Development of a Workflow for Designing Patient-Specific Mandibular Reconstruction Implants and Predicting their Performance through Experimentally Validated Finite Element Models

Arthur van Kootwijk

Technische Universiteit Delft

TU Delft

Development of a Workflow for Designing Patient-Specific Mandibular Reconstruction Implants and Predicting their Performance through Experimentally Validated Finite Element Models

by

Arthur van Kootwijk

to obtain the degree of Master of Science
at the Delft University of Technology,
to be defended publicly on Wednesday September 29, 2021 at 09:00 AM.

Student number:	4948564	
Project duration:	August 1, 2020 – September 29, 2021	
Thesis committee:	Dr. M. Mirzaali,	TU Delft, supervisor
	Dr. N. Sarkalkan,	TU Delft, supervisor
	Dr. S. Kumar,	TU Delft
	V. Moosabeiki,	TU Delft
	Dr. M. Ahmadi,	Amber implants, supervisor
	Prof. dr. E. Wolvius,	Erasmus MC, supervisor
	Drs. B. Jonker,	Erasmus MC

This thesis is confidential and cannot be made public until September 29, 2025.

Abstract

Restoration of the normal mandibular form and function is attempted with reconstructive surgery. The current standard procedure to restore continuity defects of the mandible involves free tissue transfer with an autologous bone flap. Even though the success rates are high, several critical drawbacks have been associated with this procedure, including severe donor site morbidity, long hospital stay and recovery process, need for high surgical expertise, insufficient bone graft height, and mechanical failure of the plating system. A systematic approach for the designing and testing of patient-specific implants used as an alternative to the free flap procedure appears to be still lacking.

The goal of this thesis project was to develop a semi-automatic workflow for designing patient-specific mandibular reconstruction implants and assess the effect of topology optimization on the biomechanical performance of the implant using the finite element analysis (FEA) and experimental validation. Using the proposed workflow, a fully porous implant (lattice implant) and a topology optimized implant (TO implant) were designed according to the anatomy of a synthetic mandible analog subjected to lateral resection, and were additively manufactured using selective laser melting. Both implants were designed in the shape of a cage to allow for the insertion of a bone graft and the integration of dental implants. The mechanical performance of the reconstructed mandibles was predicted with computational FEA and evaluated through quasi-static and cyclic experimental testing. Digital image correlation was used to validate the finite element model through principal strain field comparison.

An excellent fit between the implants and mandibles was established, indicating the capability of the workflow to develop customized implants with accurate dimensions. The results obtained with FEA were in agreement with the DIC measurements and quasi-static testing results. No significant differences ($P < 0.01$) in mean stiffness, mean ultimate load, and mean ultimate displacement were found between the non-implanted control mandibles, lattice-implanted mandibles, and TO-implanted mandibles during quasi-static testing. No implant failure was observed during static nor cyclic testing at loads substantially higher than the average maximum biting force of healthy individuals, indicating the high resistance of the implant designs to mechanical failure. Yet, the lattice implant would likely be preferred over the TO implant for clinical application due to its lower weight (16.5%), higher porosity (17.4%), and shorter workflow time (633.3%).

The workflow proposed in this study may offer surgeons and medical engineers the tools to systematically design and evaluate patient-specific reconstruction implants. This would result in more cost-effective and time-effective pre-surgical planning and result in implant designs that can minimize morbidity and maximize aesthetic and functional outcomes.

Acknowledgements

First of all, I would like to thank my daily supervisors Dr. Mohammad Mirzaali and Dr. Nazli Tumer from TU Delft for all the support, encouragement, and constructive advice throughout the course of the project.

I would like to thank Prof. Dr. Eppo Wolvius and Drs. Brend Jonker from Erasmus MC for sharing their clinical expertise in the field studied.

I would like to thank Dr. Mohammad Ahmadi from Amber Implants for his cooperation and insightful suggestions.

Finally, I thank Dr. Jie Zhou, Vahid Moosabeiki, Sander Leeflang, as well as all of the Section members of Biomaterials and Tissue Biomechanics for their contributions and input in the group discussions.

Contents

Nomenclature

Symbols

μ	linear attenuation coefficient
ν	Poisson's ratio
$\overline{x}$	mean shape
Φ	weighted sum of the modes of variation
ρ	density
A	elongation at break
b	vector containing the shape parameters
E	Young's modulus
F	force
k	global stiffness matrix
LE	logarithmic strain
N	number of cycles-to-failure
P	p-value
R_m	tensile strength
$R_{\rho 0,2}$	offset tensile yield strength
Ra	roughness average
Rz	mean roughness depth
S	maximum stress amplitude
s	stress
S_e	endurance limit stress amplitude
SE	strain energy
ss_1	no. sampling points across the target bone
ss_2	no. sampling points across the fitted bone
U	displacement
u	displacement vector
UR	rotational displacement
V	volume
x	estimated shape
x_e	design variable vector

Z	reduction of area

Abbreviations

ABS	acrylonitrile butadiene styrene
AM	additive manufacturing
BMP	bone morphogenetic protein
C3D10	10-node quadratic elements
C3D4	4-node tetrahedral elements
CAD	computer aided design
CAM	computer aided modelling
CAS	computer aided surgery
CT	computed tomography
DIC	digital image correlation
DICOM	Digital Imaging and Communications in Medicine
EBM	electron beam melting
ELI	extra low interstitials
EXP	experiment
FDM	fused deposition modeling
FE	finite element
FEA	finite element analysis
GUI	general user interface
HC	healthy control
HCL	hemimandibular (H), central (C), lateral (L)
HIP	hot isostatic pressure
HU	Hounsfield unit
INC	incisal clenching
LA	lattice
LED	light-emitting diode
LUT	lookup table
MPC	multi-point constraints
MTEL	maximum triangle edge length
OSCC	oral squamous cell carcinoma
PBCM	particulate bone and cancellous marrow
PC	polycarbonate

PCA	principal component analysis
PCL	polycaprolactone
PDL	periodontal ligament
PDLLA	poly (D, L-lactide)
PLA	polylactic acid
PLLA	poly (L-lactide)
PSI	patient-specific implant
PU	polyurethane
PVE	partial volume effect
RMB	right molar biting
ROI	region of interest
SIMP	solid isotropic material with penalization
SLM	selective laser melting
SSM	statistical shape model
SUD	surface deviation
TMJ	temporomandibular joint
TO	topology optimization
TPMS	triply periodic minimal surface
VSP	virtual surgical planning

List of Figures

List of Tables

Study outline

This thesis report is structured as follows (Figure 1). Chapter 1 addresses the relevance of the study by familiarizing the reader with the etiology of mandibular reconstructions, and by clarifying the need for further research and development in the field. The required background information is given in Chapter 2, covering the basic anatomy of the human mandible, current mandibular reconstruction procedures and some promising developments, additive manufacturing, digital image correlation, and the use of finite element analysis for mandibular reconstruction purposes. Next, the goals of this study are elaborated on by identifying the drawbacks and pitfalls of the current reconstruction procedures, and by setting out the associated research objectives in Chapter 3. Chapter 4 covers the methods used for data acquisition, image processing, implant designing, computational modeling, experimental validation, and integration of the digital steps into a semi-automatic workflow. Accordingly, the computational and experimental results will be presented and compared with each other in Chapter 5. The discussion in Chapter 6 outlines the interpretation of the results, points out some general remarks, and addresses the study limitations. Finally, a conclusion will be drawn, and future recommendations will be given in the last Chapter.

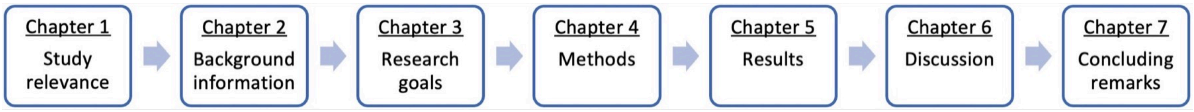

Figure 1. Summary of the study outline.

1

Relevance

The lower jaw or mandible is important for a variety of functions, of which speech and mastication (chewing) are the most important. In some situations, a specific segment of the mandible needs to be resected (removed), leaving a gap in some portion of the mandible. This gap is generally referred to as a ‘continuity defect’ of the mandible. Continuity defects of the mandible may result from tumor resection (benign or malignant), trauma, osteomyelitis, or osteoradionecrosis (Kumar et al., 2016; Goh et al., 2008; R. C. Wong et al., 2011). These main causes will be shortly discussed in the next few paragraphs. Mandibular reconstruction is a routine surgical procedure for the restoration of mandibular continuity defects. Patients with unrepaired defects might eventually suffer from facial deformity, loss of speech and reduced masticatory function, which severely affects the patient’s quality of life (R. C. Wong et al., 2011). The ideal reconstruction procedure aims to optimize functional and cosmetic outcomes by restoring facial dimensions (i.e. height, width and, projection), replacing compromised soft tissues, and by providing a foundation for dental rehabilitation (Kumar et al., 2016). Even though many different reconstruction methods have been developed, in particular over the last 40 years, an ideal solution that reproduces accurate shape and function still does not exist.

Most segmental defects of the mandible are the result of tumor therapy and - to a lesser extend - avulsion injury. Oral squamous cell carcinomas (OSCC) are oral malignancies that represent about 95% of all oral cancers and worldwide affect more than 270,000 people annually (Elaiwy et al., 2020; Sproll et al., 2020). Development of OSCC is strongly associated with long-term exposure to tobacco and alcohol consumption, especially a combination of both. Ameloblastoma is the most common benign tumor of the lower jaw, comprising about 1% of all jaw cysts and tumors (Petrovic et al., 2018). Close proximity or infiltration of the tumor from associated soft tissue to the mandible requires resection of the bone with adequate safety margins. The two types of resections that can be performed depending on the tumor location, degree of infiltration into underlying bone, and residual bone height are marginal mandibulectomy and segmental mandibulectomy (Figure 1.1). With marginal mandibulectomy, the inferior border of the mandible can be left intact, thereby preserving mandibular bone continuity. Clearly, patients would profit more from marginal mandibulectomy, but once the bone has been grossly evaded by the tumor cells, segmental mandibulectomy and subsequent reconstruction will often be inevitable.

Mandibulectomy may also be an appropriate treatment in cases of severe oral and maxillofacial trauma. Avulsive mandibular wounds predominantly result from firearm injuries and industrial accidents, as well as motor vehicle collisions. Other causes of segmental resection include radiation-induced osteoradionecrosis and, less commonly, infectious diseases such as osteomyelitis (Kumar et al., 2016).

Even though the surgical procedures have improved remarkably in the last decade, reconstruction of large mandibular defects remains a major challenge for maxillofacial surgeons, and a procedure that produces optimal aesthetical and functional outcomes is still lacking. Current segmental reconstructions typically involve vascularized bone grafting and osteosynthesis plating techniques, which are associated with several drawbacks that will be covered in Section 3.1. Adjustments of the shape

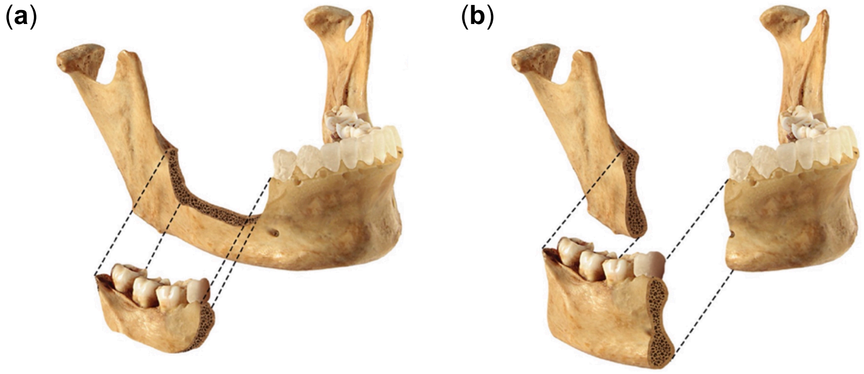

Figure 1.1. Example of (**a**) marginal and (**b**) segmental mandibulectomy. Figure adapted from Mehta and Kuriakose (2021).

and mechanical properties of the implanted material to the patient's specific situation appears to be crucial for the reconstruction system to be successful, and have been a driving force for the application of additive manufacturing (3D printing) technologies and computational tools such as finite element analysis (FEA) to produce patient-specific reconstruction implants.

Creating simulations of a living tissue environment is, however, extremely challenging. Modeling anatomically and biomechanically complex structures like the mandible involves estimations and approximations of many different material properties, geometries, and tissue interactions. Besides, the presence of model uncertainties that result from a lack of knowledge regarding the physical system of interest (e.g., how to realistically model distributed muscle forces and boundary conditions) may lead to a wide variety of model input values between different computational studies (Vollmer et al., 2000). Therefore, credibility assessment of the computational model through accurate model verification and experimental validation is essential for the theoretical predictions to be accepted and extrapolated by clinicians and medical engineers (Anderson et al., 2007). In order to obtain accurate numerical predictions of mandibular reconstruction implant designs, an experimental validation framework should be determined to minimize the uncertainties in the computational model and optimize longterm performance of the implant (Henninger et al., 2010). For now, there appears to be a major shortfall on the amount of data that represents experimental verification of FEA models on the mandible, and therefore a general consensus on how to define representative input factors for the model is still lacking (Merema et al., 2021). Considering this as well as the advances in medical implant technology, finding systematic approaches to develop and test 3D-printed patient-specific implants for maxillofacial reconstructions is currently an attractive topic of research (Du et al., 2020).

2

Background information

2.1. Anatomical structures

2.1.1. Anatomy of the healthy mandible

The mandible is a single bone that is made up of three main parts: the body, the ramus (one on either side) and the alveolar process. Figures 2.1-a and 2.1-b give an overview of the right medial and right lateral landmarks of the mandible, respectively. The mandibular body is the horizontal and largest part of the mandible that forms the chin. The midline of the body is called the mandibular symphysis. The alveolar process is an arch located on top of the mandibular body and contains the teeth. The ramus is the part of the mandible that projects upwards from the posterior side of the mandibular body. The anterior part of the ramus extends into the condylar process (condyle) and the coronoid process, which are separated by the mandibular notch. The condyle is connected to the temporal bone of the skull by the temporomandibular joint (TMJ). The point where the inferior margin of the ramus turns upwards is called the mandibular angle, which forms the juncture between the mandibular body and ramus. The inferior alveolar nerve and blood vessels, responsible for providing sensory innervation to the lower teeth and lip, enter the mandible at the mandibular foramen and exit through the mental foramen (Brand and Isselhard, 2014).

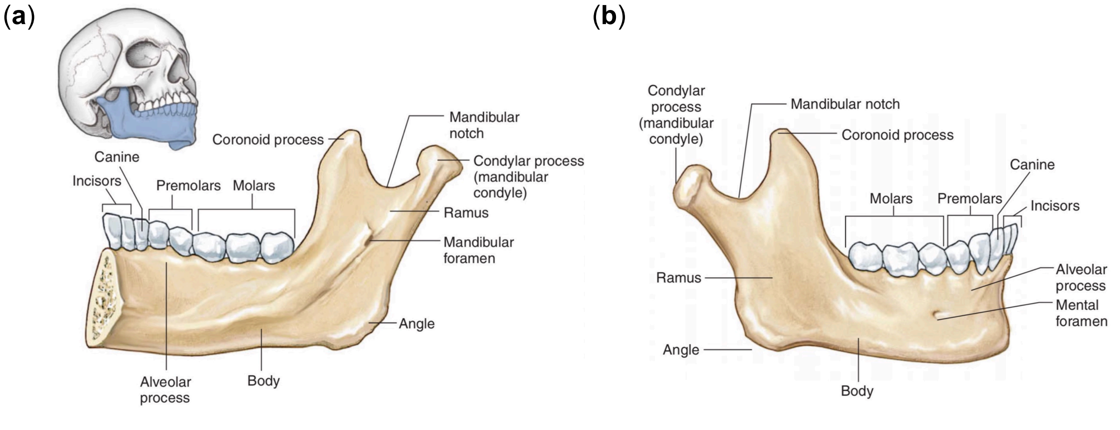

Figure 2.1. Overview of the mandible anatomy in a right medial (**a**) and right lateral (**b**) view. Figure adapted from Patton and Thibodeau (2012).

2.1.2. Muscles of mastication

The four muscles that are mainly responsible for mastication (chewing movement) are the masseter muscle, temporal muscle, and pterygoid (medial and lateral) muscles. These four muscles will be shortly discussed hereafter. The most powerful muscle is the masseter, which upon contraction elevates the mandible leading to mouth closure (Figure 4-a). The masseter consists of two heads, called superficial head and deep head. Both heads originate from two different areas on the zygomatic arch.

The larger superficial head is inserted into the mandibular angle and is oriented downward and slightly backward. The smaller deep head is inserted just above the superficial head and runs down vertically.

The temporal muscle or temporalis originates from a very broad area on the temporal fossa (Figure 2.2-a). From there, the fibers run down and insert in the coronoid process, and sometimes attach further down along the anterior border of the ramus. Contraction of the entire temporal muscle pulls the coronoid process upward, leading to elevation of the mandible and hence closure of the mouth. Contraction of only the posterior muscle fibers results in horizontal pulling on the coronoid process, causing the mandible to move backward (retruding movement).

Both the lateral and medial pterygoid muscles have two heads (Figure 2.2-b). The lateral pterygoid muscle arises from areas in the greater wing of the sphenoid bone (superior head) and pterygoid plate (inferior head) and runs in a horizontal posterior direction. The small superior head enters the TMJ capsule where it attaches to the joint disc. The large inferior head inserts into the medial and anterior condyle neck. Contraction of the lateral pterygoid muscle can result in different movements, depending on the heads that contract. The main functions are lowering of the mandible (depressing movement), moving the mandible forward (protruding movement), and to a lesser extent rotation of the mandible. The medial pterygoid muscle has its origins in the lateral and medial pterygoid plate and palatine bone (deep head), and tuberosity of the maxilla and palatine bone (superficial head). All fibers run down and in a slightly lateral and posterior direction to where they insert at the medial side of the ramus and mandibular angle. Contraction of the medial pterygoid muscle mainly leads to elevation of the mandible, thus mouth closure, and to a lesser extent rotation of the mandible.

The four muscles discussed above take care of nearly all jaw movements. However, there are other muscles (the hyoid muscles) involved in strong mandibular depression and slight mandibular retrusion. These muscles are less important for the mastication movement. For the sake of simplicity, these muscles are usually excluded from numerical models of the reconstructed mandible and will therefore not be further discussed for the purpose of this study either.

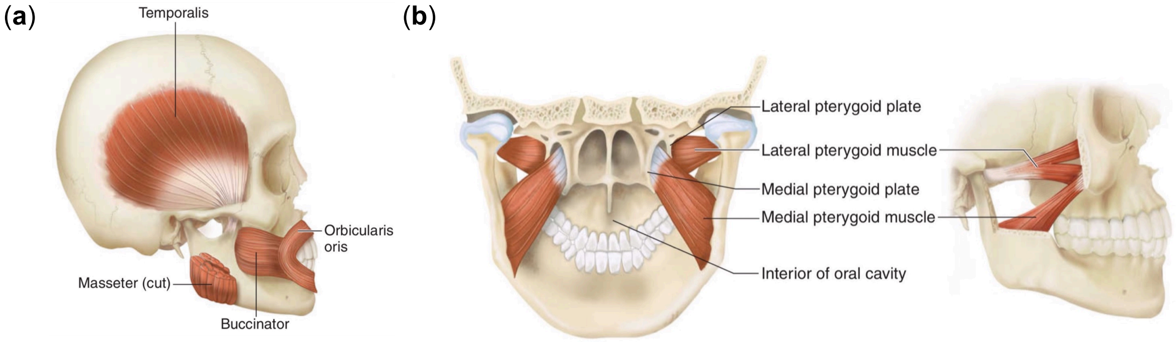

Figure 2.2. Overview of the most important muscles of mastication, showing (**a**) a right lateral dissection view of the masseter (cut) and temporalis muscles, and (**b**) a posterior (left) and right lateral (right) dissection view of the lateral and medial pterygoid muscles. Figure adapted from Patton and Thibodeau (2012).

2.2. Current mandibular reconstruction procedures

The loss of mandibular continuity can give rise to a variety of issues, including malocclusion, airway compromise, difficulty with mastication, speech and swallowing, and cosmetic distortion due to the loss of facial contour (Kakarala et al., 2018). Therefore, comprehensive reconstruction strategies are required to restore the functional and aesthetic features of the mandible. Besides, the implanted material should allow for implementation of dental prosthetics at a later stage (Pinheiro and Alves, 2015). However, due to the mandible's complexity, its many different functions and the high rate of postoperative complications, mandibular reconstruction remains very challenging, and consensus on the ideal reconstruction system that meets all functional and aesthetical criteria and prevents all of the aforementioned issues is still lacking (Kakarala et al., 2018). In what follows, a brief overview of the current procedures and perspectives for segmental mandibular defect reconstruction will be presented. Reconstruction with soft tissue only, i.e. without bony reconstruction or rigid plate fixation, will not be discussed.

2.2.1. Defect classification

Mandibular defects can be divided into different classes, depending on the location and extent of the defect. Many different classification systems have been described, but the systems proposed by Boyd et al. (1993) and Urken et al. (1991) have been cited most widely. The system proposed by Boyd utilizes an “HCL” description for central (C) defects that include both canines, lateral (L) defects that include the lateral mandible, and hemimandibular (H) defects that include both the lateral mandible and condyle (Figure 2.3), whereas Urken uses the standard anatomical designations (i.e., symphysis, body, ramus, condyle) to define the region of defect. Both systems have been extended to also include mucosal and soft tissue components. These classification systems, as well as more recently proposed systems, are important for maxillofacial surgeons and medical engineers to determine and compare reconstruction modalities for optimal aesthetic and functional outcomes. However, the standard classifications are sometimes difficult to apply in clinical routine practice. Therefore, the type of reconstruction still largely depends on the associated soft tissues to be reconstructed and the common practice and experience of the surgical team (Paré et al., 2019).

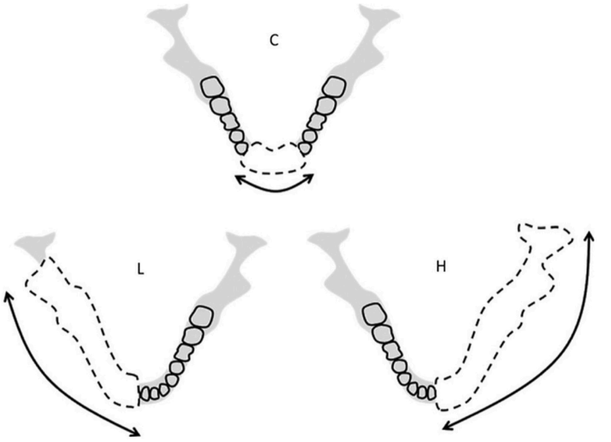

Figure 2.3. Schematic overview of the HCL mandibular defect classification system described by Boyd et al. (1993). Figure extracted from Kumar et al. (2016).

The remaining part of this report will adopt the classification system proposed by Boyd et al. (1993), as presented in Figure 2.3.

2.2.2. Fixation plates

Treatment of mandibular continuity defects with rigid reconstruction plates and concurrent or subsequent osseous (bone) grafting has become standard for almost all reconstruction procedures (Kakarala et al., 2018). The number of plates, plate sizes (i.e., length and thickness) and number of screws are considered based on the type of defect, type of reconstruction (i.e., with/or without bony reconstruction, vascularized/non-vascularized bone graft) and preference of the surgeon. The efficacy of osteosynthesis procedures has recently improved by the use of titanium fixation plates and locking screws due to their improved biocompatibility and biomechanical performance (Seol et al., 2014). Traditionally, standard commercial plates were mostly used for mandibular reconstruction. These plates are straight and need to be bend intraoperatively to the anatomy of the patient. This is not only time consuming, but it may also adversely affect the fatigue strength of the material, potentially as a result of tensile residual stresses generated in plate bending, thereby increasing the chance of delayed plate fractures (Almansoori et al., 2020; Martola et al., 2007). The average plate exposure rate calculated for 17 studies, the average plate fracture rate calculated for 19 studies, and the overall average of plate removal across 11 studies have been reported to be 19.3%, 7.5% and 25.5%, respectively (Almansoori et al., 2020). A recent study carried out by Almansoori et al. (2020) among 159 patients showed a high number of plate fractures (13.8%).

Alternatively, mini-plates with a small diameter (≤2 mm) can be used and are associated with several advantages compared to larger reconstruction plates, including ease of application and (if necessary) removal, reduced fixation times, and a decreased risk of disrupting the vascular pedicle (S.-P. Liu et al., 2016). The main drawbacks associated with reconstruction using mini-plates include the increased risk of plate fracturing, as well as inadequate union of the neomandible. The use of pre-bent plates with plate designs based on patient-specific 3D models of the mandible has helped to overcome some of these issues and have proven to shorten operative times considerably (Kakarala et al., 2018; Naros et al., 2018). Besides, the recent developments in preoperative 3D modelling and additive manufacturing have opened up the possibility to create custom or patient specific titanium plates. The use of computer aided design (CAD)/computer aided modelling (CAM) not only enables the design of patient specific plates that are functionally and aesthetically more suitable than conventional or prebent plates, but it also provides the possibility to use FE modelling to pursue optimal plate strength.

Finally, there is also the possibility for reconstruction using a rigid fixation plate only. This method is typically used as an alternative for patients that are poorly suited to free flap reconstruction. Downsides of this technique are that it needs adequate soft tissue coverage to prevent plate exposure and that the chance of plate fracture is relatively high because of its load bearing demands. Therefore, this option is limited to lateral defects in edentulous patients with limited chewing strength and is preferably avoided (Paré et al., 2019).

2.2.3. Vascularized free tissue transfer

Due to its low failure rate and ability to restore mandibular function at a multitissue level, osteocutaneous tissue-free transfer is considered as the treatment of choice for mandibular defect reconstruction. The transfer involves transmission of bone and soft tissue from the donor site to the mandibular defect while ideally preserving the blood supply for enhanced graft viability and union (Taqi and Raju, 2020). The bone graft is held in place by a fixation plate that is either pre-bent or bent intraoperatively, as discussed earlier. Depending on various factors such as the location and length of the damaged mandible segment, the type of tissue that is required, and the experience of the surgical team, a specific donor site is selected to obtain the free flap from. Due to its high bone quality, low donor site morbidity, long bicortical and vascular bone segments, and large diameter vessels, mandibular reconstruction with the fibular free flap is still considered as the gold standard, especially for larger bone defects (12-15 cm) (Paré et al., 2019; Kakarala et al., 2018) (Figure 2.4). The iliac crest, scapula and radius are also commonly used as donor sites for vascularized free flaps. These are only suitable for smaller sized defects and will be used in case the fibula is not a suitable option due to prior surgery, trauma, poor vascularity or for specific skin paddle requirements (Kakarala et al., 2018).

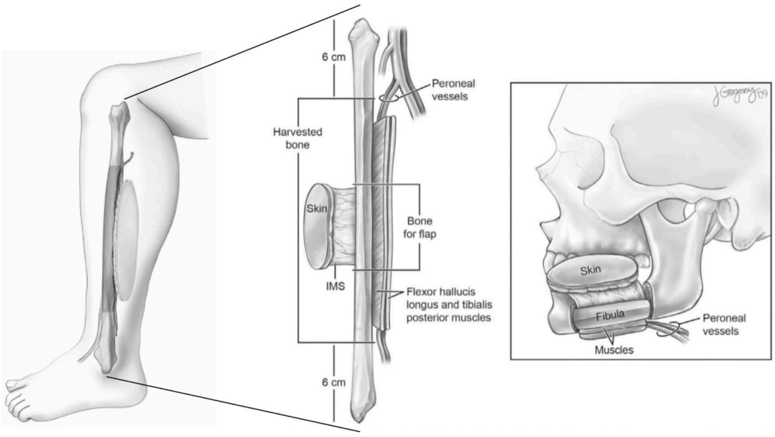

Figure 2.4. Illustration of the fibular free flap anatomy and reconstructed mandibular segment with the fibular flap inset. Figure adapted from Bak et al. (2010).

2.2.4. Non-vascularized bone transfer

In case there is only a small bone defect with little or no soft tissue loss and if the patient has not been radiated previously or will be radiated in the future, a non-vascularized bone graft is considered as an option for reconstruction. Favourable donor sites for these procedures are the iliac crest and rib (Kumar et al., 2016). Due to the efficiency and high success rates with respect to functional and aesthetic outcome of osseous free flaps, this technique has been acknowledged less by surgeons. However, with the emergence of tissue engineering, which will be further discussed below, this technique remains an important option for a selective group of patients, as well as a relevant topic for future research.

2.3. Developments and future directions

Technological advances, including virtual surgical planning (VSP) and CAD/CAM are becoming increasingly useful for preoperative planning and simulation (Paré et al., 2019). Together with the evolution of rapid prototyping and 3D printing technology, computer aided surgery (CAS) has had a revolutionary influence on mandibular surgery since its introduction in 2009 (van Baar et al., 2018). In brief, CAS comprises different phases of planning, modelling and evaluation in order to accomplish individualized mandibular reconstructions (Figure 2.5). The surgeon and engineer collaborate prior to surgery to plan osteotomies of both the native mandible and donor bone, apply mirroring techniques on the unaffected mandible, assess optimal positioning of dental implants, design drilling guides and customized plating systems and, foremost, restore accurate occlusion. The use of CAS in mandibular reconstruction has shown significantly improved aesthetic outcomes and dental rehabilitation, and has led to shorter operative times, which have been reported to be 25% lower compared to conventional surgery without VSP (van Baar et al., 2018; Y. Wang et al., 2016). CAS has been introduced to the field of oral and maxillofacial surgery relatively recently, and it might not (yet) be as cost-effective in cases where it is not required, and standard plating systems can be used instead. However, due to its wide and continuously growing scope of application and promising outcomes, it is now becoming standard practice for mandibular reconstruction.

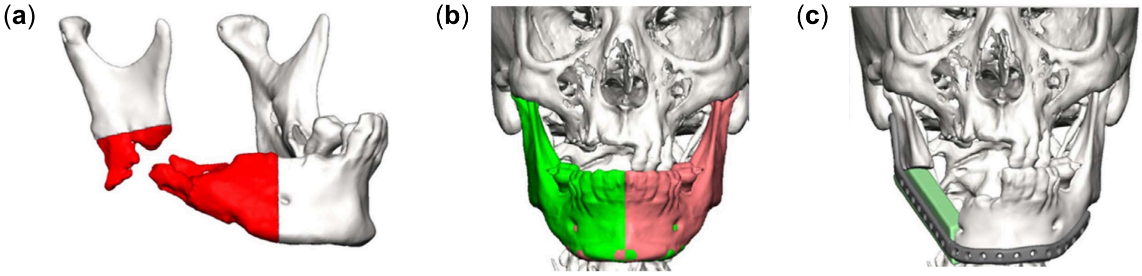

Figure 2.5. Overview of some important stages in VSP, showing (**a**) the mandibular defect (red area), (**b**) mirror image applied to the contralateral mandible, and (**c**) the reconstructed mandible with a fibular bone graft secured by a customized fixation plate. Figure adapted from Kakarala et al. (2018).

2.3.1. Tissue engineering

One of the main drawbacks of the current bone grafting procedures is that it is associated with donor site morbidity, which is reported to occur in 31.2% of patients (Nelms and Palmer, 2019). The primary morbidities include pain, paresthesias, wound-healing disturbance, motor weakness of the lower leg muscles, cold intolerance, edema, and gait disturbance, and have been reported to lead to long-term morbidities in 17% of the patients (Momoh et al., 2011). Consequently, a great deal of research is being conducted on finding bone grafting alternatives, among which bone tissue engineering might be the most promising. The main aim, and at the same time the big advantage with respect to free tissue transfer, is to generate bone that is adaptable to different bone defects and can thus be applied to every patient, thereby reducing donor site morbidity, operative complexity, and surgical time. Biomimetic scaffolds can be customized using CAD/CAM techniques, and a group of growth factors called bone morphogenetic proteins (BMPs) are typically used together with stem cells to induce functional tissue generation according to the morphology of the defect (Kumar et al., 2016; Nelms and Palmer, 2019). Particular benign defects might be suitable for treatment using tissue engineering approaches. Good reconstruction results have been achieved with cadaveric non-vascularized bone graft segments seeded with BMPs to stimulate osteogenesis (Kakarala et al., 2018). However, growing bone tissue at the site of defect using tissue engineering approaches is associated with technical difficulties since it would require a healing period during which the mandible should be inactive. Besides, malignant or large defects or patients exposed to radiation are still prone to oncogenic and other unpredictable effects exerted by morphogenetic growth factors (Kumar et al., 2016). Hence, treatment with free bone flaps remains inevitable in these cases.

2.3.2. PBCM grafts and alloplastic bone substitutes

Several studies have investigated the potential to reconstruct mandibular defects using a modular endoprosthesis (Figure 2.6-a). The concept of the endoprosthesis has been very successfully applied in the field of orthopaedics, especially for limb defects (Kumar et al., 2016). The procedure comprises removal of the damaged tissue, followed by placement of a metallic device into the medullary space of the remaining mandibular stumps after resection. The endoprosthesis is attached to the remaining bone stumps with a stem using cemented or press-fit fixation, thereby eliminating the need for screw fixations. Variable defect lengths can be bridged by using different module sizes. The modules are connected through a locking system. The endoprosthesis is relatively easy to place in long bones due to their straight and concentric cross-sectional appearance. However, to put an endoprosthesis in the mandible is more challenging due to the natural anatomic curvature and flat cross-section of the mandible. The mandibular curvature varies between individuals, making it difficult to develop a stock prosthesis. Tideman and Lee (2006) described the use of a modular endoprosthesis as a novel alloplastic reconstruction method of the mandibular body and ascending ramus. In most of studies, animal studies were performed, which were often successful, but also showed some tenacious problems with module connection loosening, infection, and loss of bone mineral density in the peri-implant region (S. Lee et al., 2008; Goh et al., 2008). *In-silico* analyses of an updated version of the modular endoprosthesis were shown to be promising for small defects (R. C. Wong et al., 2012b). A custom endoprosthesis for the restoration of major defects was proposed by Pinheiro and Alves (2015). Here too, promising results were found based on FEA. However, in-vivo experiments remain to be done and much more questions need to be answered before this prosthesis can be put into clinical practice.

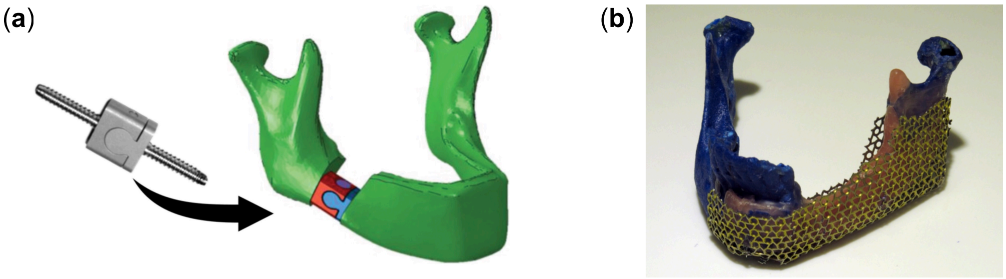

Figure 2.6. (**a**) Design and implantation of a modular endoprosthesis for mandibular reconstruction adapted from R. C. Wong et al. (2012a) and C. Wong et al. (2016), and (**b**) example of titanium mesh design adapted from Malekpour et al. (2014).

Finally, a promising alternative to reconstruction with free bone flap, and also the type of reconstruction investigated in this research, is the use of particulate bone and cancellous marrow (PBCM) packed in an alloplastic tray (Figure 2.6-b). Materials that are typically used for the tray include alloplastic trays (e.g. titanium and Dacron), and biodegradable or resorbable alloplastic trays typically made of poly (L-lactide) (PLLA) or poly (D, L-lactide) (PDLLA) (Kinoshita et al., 1997 & Louis et al., 2004). The cancellous bone grafts are typically obtained from the iliac crest (Bailey, 2001). Advantages of this method are the ability to approach correct anatomical height and arch symmetry, restore defects of any given length, and to allow for dental implant support. Tideman et al. (1998) proposed such a custom-made titanium mesh or tray system. In short, an alloplastic (titanium) tray was designed to support a non-vascularized autogenous corticocancellous iliac bone graft matching the shape of the resected mandibular segment. The procedure minimizes donor site morbidity and gives adequate functional and aesthetical outcomes. Other successful clinical results with custom-made titanium mesh filled with PBCM was reported by Y.-W. Lee et al. (2018).

2.4. Additive manufacturing

Additive manufacturing (AM) has become an important manufacturing method in both research and industry. With AM, parts are built in 3D by adding material layer-by-layer directly from CAD model data. Depending on the application, products can be fabricated from different materials, including polymers, ceramics, and metals. The main advantage of AM is the ability to create arbitrarily complex shapes, such as hollow, porous and lattice structures, directly from a material feedstock (S. Liu and Shin, 2019). Not only gives this nearly unlimited degrees of freedom in product design, but the technique also becomes highly cost-effective for small-scale production and therefore becomes particularly attractive for the development of patient-specific implants (Munir et al., 2017).

Selective laser melting (SLM) is, along with selective laser sintering (SLS) and electron beam melting (EBM), presumably the most commonly used additive manufacturing method for metallic parts in industrial applications (Zhang et al., 2018). The principle of SLM is based on the process where a high-powered laser melts and fuses metallic powder particles together (Figure 2.7-a). After melting the first layer of the build, a fresh layer of powder material is distributed over the built platform. Subsequent fusion occurs between adjacent layers until the build has completed. Parts printed with SLM usually are of high-density and show good mechanical, corrosion and tribological properties, often better than other metal AM methods (Attar et al., 2015 & Sercombe et al., 2018).

Fused deposition modeling (FDM) is the most common material extrusion AM technique and is primarily used for the manufacturing of thermoplastic polymers, such as polylactic acid (PLA), acrylonitrile butadiene styrene (ABS), polycaprolactone (PCL) and polycarbonate (PC) (Pelleg, 2020). In FDM, a thermoplastic filament is fed into a temperature-controlled extrusion head (nozzle) where it is heated to a semi-liquid state and deposited layer-by-layer onto a substrate (Figure 2.7-b). Mechanical properties of the end product depend on several 3D printing parameters, including bed and printing temperature, printing speed, layer thickness and infill density (Pradhan et al., 2021). FDM is a flexible, cost effective and relatively simple technology that has become the most accessible and widely used AM technology. It allows fabrication of multicomponent and multimaterial parts with almost any geometrical complexity (Pradhan et al., 2021).

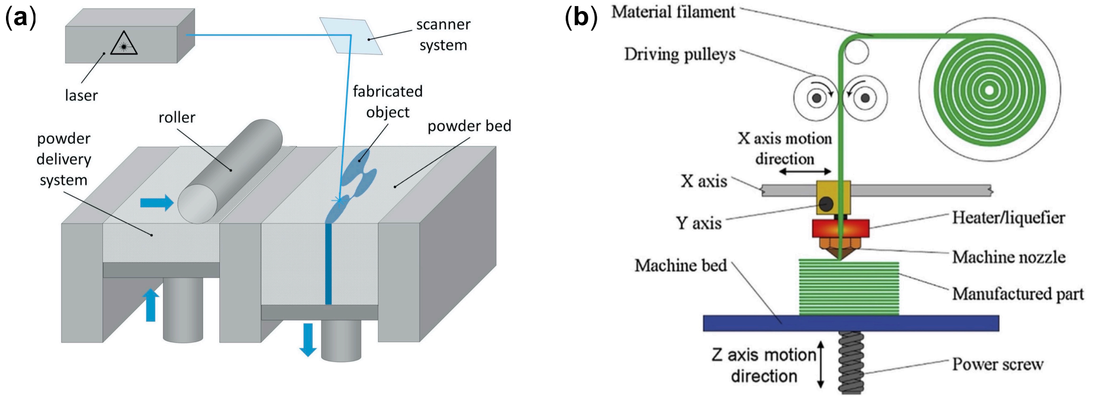

Figure 2.7. Schematic representation of the basic principles of (**a**) SLM and (**b**) FDM additive manufacturing processes. Figures extracted from Pradhan et al. (2021) and Leitz et al. (2017), respectively.

2.5. Evaluation of mandibular reconstructions with FEA

Biomechanics is essential to any musculoskeletal practice, including oral and maxillofacial surgery, and a good understanding of the mandibular biomechanics is crucial in the treatment of mandibular defects. Functional loads on the mandible create stresses and strains inside the biological structures, which induce bone remodeling, and may cause failure of the reconstruction hardware in case critical levels are exceeded. However, biomechanical analyses of the reconstructed mandible are still lacking, due to the complex biological structure and function of the mandible and its surrounding tissues, including the multidirectional muscle forces (Cheng et al., 2019). Advances in computer modelling techniques have led to the development of a computer-based numerical technique called FEA to enable accurate estimations of stress distributions within continuum structures. FEA originated in the field of civil and aerospace engineering to solve complex structural problems. However, FEA has become widely used in the prediction of biomechanical performance of medical devices and biological tissues over the past 30 years (Ko et al., 2012).

In brief, FEA is a numerical method that is used to find approximate solutions to partial differential equations by subdividing a large continuous system into a “mesh” that contains a discrete number of “elements”. The simple equations that predict the behavior of these individual finite elements are then assembled into a larger system of equations that is used to describe the loading conditions acting on the entire object, for example the mandible. (Szucs et al., 2010 & Ko et al., 2012). Computational models using FEA can predict the areas that are expected to fail, based on the areas of maximum stress concentration.

The FE model requires specification of a constitutive material model, a mesh, boundary conditions and loads. Material properties including yield properties, Young’s modulus and Poisson’s ratio, and the elastic behavior of the geometry are important input parameters that should be determined such that they represent the mechanical behavior of the implant and the surrounding tissues as close as possible. As explained before, the object needs to be discretized or meshed into a finite number of elements. This meshing step is highly important since the number and type of elements used can drastically influence the quality of the analysis. Usually, there is a tradeoff between the accuracy of the analysis on the one hand and the required computational power and time as the number of elements in the model increases on the other hand. The boundary conditions include the constraints that are applied to the mandible to prevent it from moving globally in space. For example, FE analysis of mandibular reconstruction typically involves fixation of the condyle areas, as well as a limitation on freedom of movement at the area of occlusion. Another example of a boundary condition that is often used in FE models of the reconstructed mandible is the application of contact sets between different material parts that are in contact with each other, such as between cortical and cancellous bone or between the osteosynthesis parts and the bone. External forces on the mandible are generated through loading conditions that comprise a force origin, direction and magnitude, and usually represent the musculatory system (Merema et al., 2021).

The location and magnitude of the loads and boundary conditions generally depend on the desired biting tasks. For the reconstruction to be successful, the mechanical properties of the reconstruction system should withstand the stresses and strains caused by the repetitive forces of mastication that belong to that specific biting task. Assessment of the various stresses, strains and displacements of the model gives the surgeons and engineers the information necessary to decide whether modifications on the implant design are required (Ilavarasi and Anburajan, 2011).

Due to the many different input variables such as material characteristics of bone, constraints on the mandible and reconstruction system, the application of load, and the implementation of different muscle forces, force directions and magnitudes, there are large variations between the FE models that have been developed over the last few decades. Besides, many uncertainties and simplifications regarding bone material properties, distribution of loads and application of constraints make the development of a highly accurate FE model of the mandibular biomechanics practically impossible, and adequate experimental validation of the theoretical predictions is essential.

Topology optimization (TO) can be defined as a procedure to find the optimal spatial material distribution within a specified domain, commonly known as the “design space”, under a set of constraints, in order to achieve the maximum performance function of the structure (Bendsøe, 1989). One of the attractive benefits of TO in product design is its ability to reduce material while retaining structural integrity, thereby eliminating excess weight from the design. Consequently, TO has a wide range of applications in various fields, including aerospace, automotive, biomedical, and civil engineering (Figure 2.8). Over the past few years, TO has been increasingly used in the development of mandibular reconstruction implants (Y.-f. Liu et al., 2011; Y.-f. Liu et al., 2017; C.-H. Li et al., 2020). Optimization of the biomechanical structures and implant designs for orthopedic and craniofacial applications have resulted in improved repair success rates (Cheng et al., 2019).

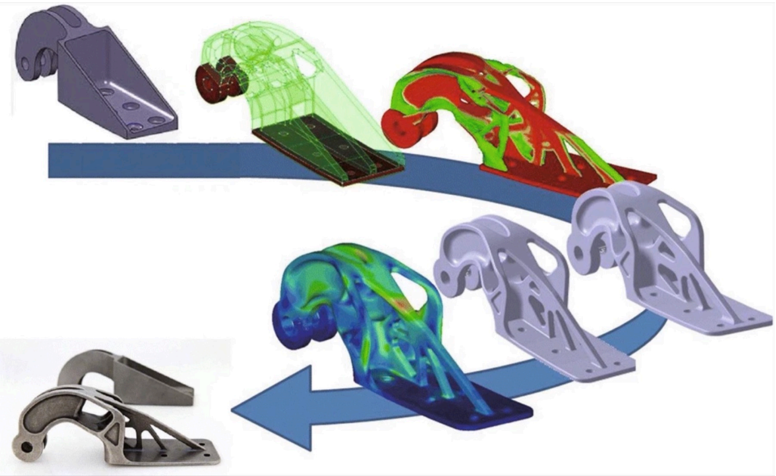

Figure 2.8. Example of AM part designed for the aerospace industry using TO techniques. Figure extracted from Meng et al. (2020).

2.6. Digital image correlation

Strains within bone indicate fracture risk, the stimulus for bone remodeling, and the influence of implants on the adaptation of bone in response to its mechanical loading. Because of that, strain measurements may give insights into pre- and postimplanted states and different implant options. Digital image correlation (DIC) is an optical non-contact and full-field strain and displacement measurement technique. In DIC, digital cameras and image registration algorithms are used to track and correlate pixel intensities on a loaded sample from two corresponding images. Strain and displacement data from DIC can provide rich information for the validation of FE simulations (Palanca et al., 2016; Rankin et al., 2017).

DIC works by tracking points on the test specimen surface that are unique from one another. For this reason, a homogeneously distributed speckle pattern must be applied to the surface. A single camera is required only if the specimen is flat, planar to the image sensor and when out-of-plane motions do not occur. If the region of interest has a curved surface, as is the case with reconstructed mandible, two cameras are required to track surface motions in 3D space. The two cameras must be calibrated with respect to one another in space in order to get an initial spatial correlation. Now, contours of the object can be calculated by the software in a 3D image by correlating the grey value patterns from both camera views. The images are then divided into smaller subsets or “facets”, which are groups of neighboring pixels with unique grey value patterns (Figure 2.9). Strains and displacements are calculated from each facet center throughout the deformed images, where the “grid spacing” defines the distance in pixels between two neighboring facet centers. Facet size is user-defined and should be large enough to provide unique speckle information for all the facets throughout the surface, while remaining small enough to maintain a high spatial resolution. Upon deformation of the surface during loading, strains and displacements are calculated from the center of each facet with respect to the reference image (i.e., undeformed state).

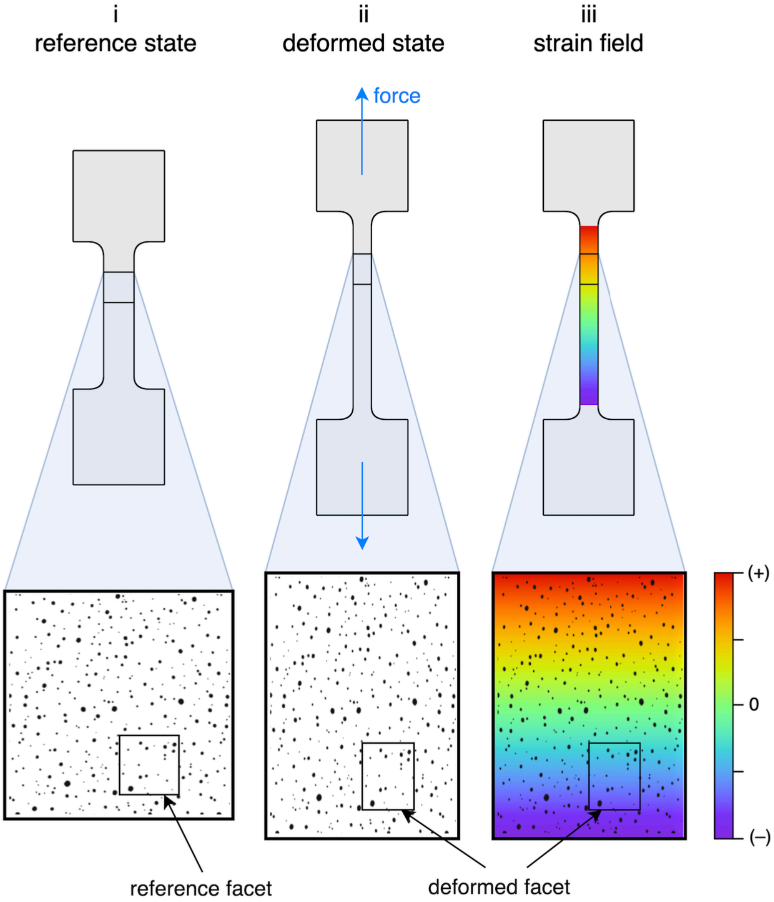

Figure 2.9. Schematic representation of the basic principles underlying DIC.

3

Research goals

3.1. Problem definition

The overall survival rate of free flap reconstructions is very high, usually even higher than 95% (Paré et al., 2019; Kakarala et al., 2018). However, there are some pivotal drawbacks associated with free tissue transfer, of which the limited amount of available bone, donor site morbidity, and the need for high surgical expertise remain the major limitations of the technique (Y.-W. Lee et al., 2018). Besides, usage of mini-plates requires manual bending of the plates on sterilized 3D models in order to match the bone anatomy of the patient. Apart from the fact that this plate bending process may be error-prone and time-consuming, it weakens the fatigue strength of the plate due to internal stress concentrations (Marchetti et al., 2006). A large variety of prostheses and osteosynthesis plates that are used for mandibular reconstruction have been reported to be associated with mechanical failure, usually resulting from fracturing, loosening or exposure of either the implant itself or the screw-fixation to the mandibular bone, as well as postoperative infections following wound dehiscence (Radwan and Mobarak, 2018; Seol et al., 2014). All of these issues often result in extended surgical procedures, prolonged hospital stays, long recovery processes, and increased risk for surgical revisions (Vignesh et al., 2019). Lastly, poor patient satisfaction was reported for fibular graft reconstructions with regard to functional performance and aesthetic outcomes (Hölzle et al., 2007).

Many of the issues mentioned above could possibly be resolved by using porous 3D printed patient-specific implants (PSIs). The PSIs are usually made of porous structures due to the many benefits associated with implant porosity, as will be discussed in Section 4.4.4. Clinical studies that have investigated customized metallic implant reconstructions with or without bony insertions have shown promising results (Dolgolev et al., 2020; W.-b. Lee et al., 2018; Y.-W. Lee et al., 2018; Malekpour et al., 2014; Mounir et al., 2020; Park et al., 2020; Rachmiel et al., 2017; Zhou et al., 2010). First, no, or minor harvesting of autologous tissue is required and therefore the risk for associated donor site morbidity will be significantly lower. Second, no intra-operative bending of hardware is required which will make the implant less susceptible to fatigue fracture. Third, less surgical expertise is required which will result in shorter operative times compared to free flap reconstructions. Fourth, the patient-specific implant is designed to the anatomy of the patient, thereby improving aesthetic and functional outcomes.

Development of PSIs for mandibular reconstruction is therefore becoming more popular, yet their suitability for clinical application is still under research. Only a few studies have reported details on the design process of customized reconstruction implants, and hardly any studies have evaluated implant performance through computational modeling with FEA (Nasr et al., 2017). Consequently, a large variety of implant designs have been created, and a lack of standardized procedures with regard to the designing and testing of such implants is evident (Merema et al., 2021). This will lead to unpredictable results and thus the whole treatment workflow becomes expensive, inefficient and time consuming (León et al., 2020). Before patient-specific 3D printed mandibular reconstruction implants can be integrated in standard treatment, convenient and systematic approaches with regard to designing, fabrication and (computational) testing must be established.

3.2. Objectives

In light of the issues raised in the previous Section, the main goal of this thesis project was to develop a semi-automatic workflow for designing patient-specific mandibular reconstruction implants and assess the effect of TO on the biomechanical performance of the implant through FEA and experimental validation.

The following sub-objectives to reach this goal were determined:

- Define the steps needed to comprise a semi-automatic workflow for the designing of patient-specific mandibular reconstructions implants.
- Develop a FE model to predict the mechanical behavior of a fully porous implant design and a TO implant design.
- Define the steps needed to validate the FE model using biomechanical experiments.
- Compare the design outcomes and biomechanical performance between the TO and non-TO implant and determine which implant design would be most suitable in the case of clinical application.

The workflow proposed in this study may help the clinical engineers to design reconstruction systems as a suitable alternative to or in combination with the current standard free flap approach in the treatment of mandibular continuity defects. The establishment of a systematic approach for the designing of patient-specific mandibular reconstruction implants may reduce the costs and duration of pre-surgical planning, while ensuring optimal aesthetics and minimizing morbidity. Combining the design workflow with validated computational predictions on the performance of the implant design could improve functional outcomes and increase surgical success rates.

4

Methods

4.1. Schematic overview of study methodology

The major steps involved in the implant development and testing are summarized in the flowchart shown in Figure 4.1. The different colors represent the software platforms that were used at each step. First, a computed tomography (CT) scan was made of the synthetic mandible analog. The Digital Imaging and Communications in Medicine (DICOM) files were processed (**a**) and a 3D model of the mandible was created (**b**) using Mimics Research® 21.0 (Materialise, Belgium) software. Then, the model was exported to the 3-Matic® 15.0 (Materialise, Belgium) software, in which the mandibular resection procedure (**c**), missing shape estimation (**d**) and implant designing (**e**) was performed. The initial design result was a fully solid implant. After implementation of lattice structures using the Materialise Magics® 24.01 (Materialise, Belgium) software (**f**) and combining this with the results of the topology optimization, the solid implant was converted into a fully porous design, from now on denoted as lattice implant (**g**), and a topology optimized design, from now on denoted as TO implant (**h**). A surgical cutting and drilling guide was designed on the same mandible model (**i**). All 3D objects, including the mandible model and the implant designs, were imported back into Mimics for material assignment (**j**). A conceptual model was defined, which represents the physical description of the loads and boundary conditions that was used in the computational and experimental analyses (**k**). First, FE simulations were performed closely simulating the experimental conditions on the control group (non-implanted intact mandible) (**l**). Then, this model was extended to simulate physiological conditions (**m**). That is, the uniaxial loading condition used in the experimental FE model was replaced by an extensive musculatory loading system, and heterogenous material assignment was implemented based on the CT grey density values and according to the values for cancellous and cortical bone found in the literature. Note that the optimized implant design (**h**) was created based on the topology optimization results of the solid implant. After SLM manufacturing of the two implant designs (**p**) and preparation of the samples (**q**), mechanical experiments were conducted (**r**). The results of the simulations (**n**) and experiments (**s**) were quantitatively compared (**t**). If there is no acceptable agreement (**u**) between the numerical predictions and experimental data, revision of the computational model or experimental setup is required (**v**).

The methods behind each step will be discussed in more detail in the following Sections of this Chapter.

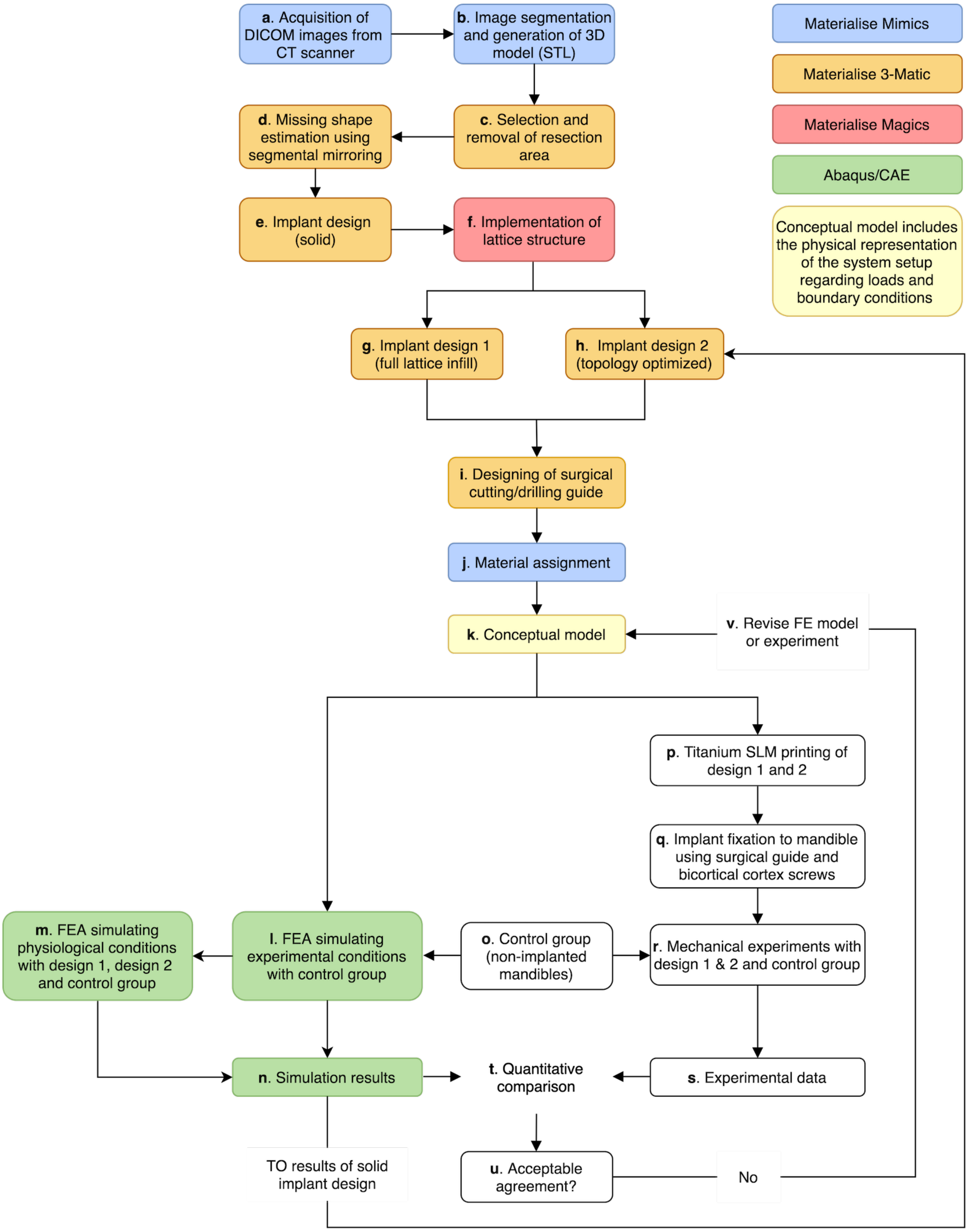

Figure 4.1. Flowchart of the steps taken to create the implant designs and validate their performance.

4.2. Mandible model and CT image acquisition

4.2.1. Synthetic mandible analog

Cadaveric bones are typically preferred when it comes to performing biomechanical experiments, as they present the unique viscoelastic behavior and the internal structures of real bone. However, the use of cadaveric bone is associated with several challenges such as availability, requirements for storage, the possibility of infection and high cost (Shim et al., 2012). Besides, consistency and reproducibility of the experiments are usually required, which are difficult to fulfil. Therefore, synthetic polyurethane (PU) mandible analogs are attractive alternatives to the cadaveric mandibles. The use of PU foam as bone analog has been proven to be a reliable substitute for cadaveric bone, showing similar compressive stress-strain curves and elastic behavior (Shim et al., 2012). For this study, PU mandible analogs (Model 8950, Synbone AG, Malans, Switzerland) were used to create the 3D model from and to perform experiments with. These models imitate real bone by having a dense outer layer and a porous inner layer, respectively representing the cortical and trabecular bone components. Besides the established history of testing with synthetic PU mandibles (Dichard and Klotch, 1994; Haug et al., 1996; Haug et al., 1998; Haug et al., 2001) it has been shown that Synbone mandibles exhibit a (2.4-mm diameter) screw insertion torque and pull-out strength similar to those of cadaveric mandibles (Bredbenner and Haug, 2000). Several studies evaluated mandibular reconstruction systems through experiments with Synbone mandibles, which led to meaningful and consistent comparison of specific design variables (Doty et al., 2004; Koper et al., 2021; Rendenbach et al., 2017; Schupp et al., 2007).

4.2.2. CT image acquisition

A CT scan of the mandible replica was made using a Siemens Somatom Volume Zoom CT scanner (Figure 4.2) with a slice thickness of 0.6 mm, 140 kVp peak potential, and field of view of 512 x 512 pixels. The 2D images were saved as DICOM files and stored in a database, which was exported to Materialise Mimics for image processing.

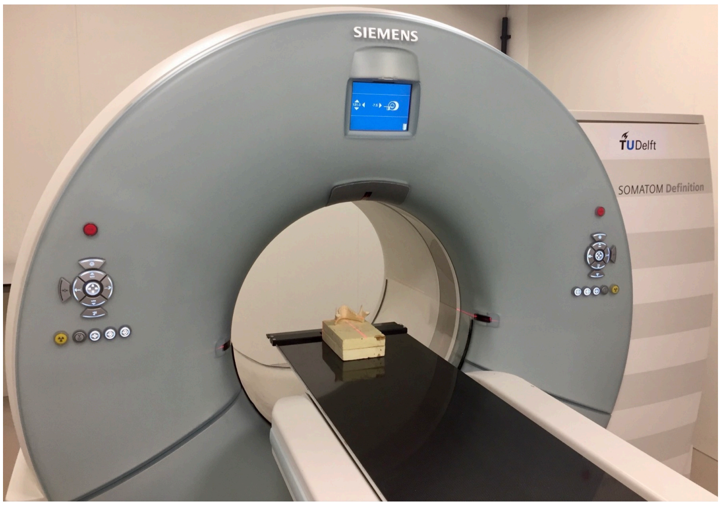

Figure 4.2. Synbone mandible model positioned inside the Siemens Somatom Volume Zoom CT scanner.

4.3. Image processing

The 2D and 3D viewports in Mimics are shown in Figure 4.3. Segmentation of the mandible model was relatively easy since no other tissues surrounding the mandible had to be dealt with. Background noise was removed from the images by thresholding the pixel intensity (-870 to 1570 Hounsfield unit (HU)), and holes in the model were automatically filled. A 3D part was calculated from the final mask. No surface smoothing or other model editing operations were performed in Mimics. The 3D part was exported to 3-Matic where the segmentation and implant designing procedures were carried out.

4.4. Implant designing

4.4.1. Area of resection

The location and size of the mandibular segment that needs to be resected from a patient depend to a large extent on the pathology being treated. The resection area investigated in the current study is a 4 cm long lateral defect type that ranges from the canine tooth up to the mandibular angle (Figure 4.4). The reason for choosing this area is that a lateral defect type (i.e., between the mandibular condyle

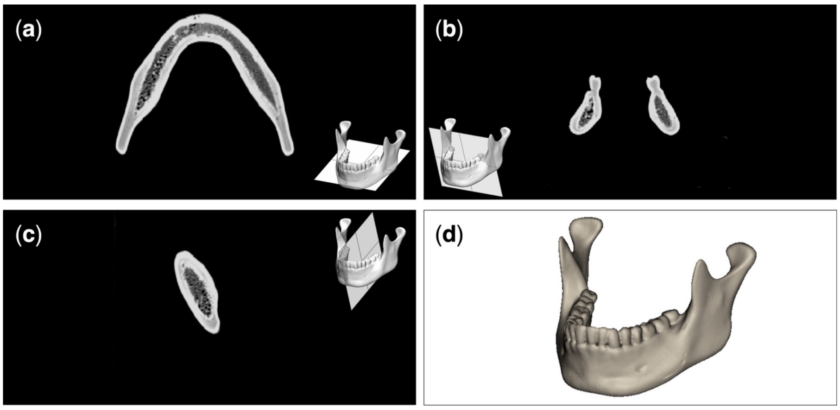

Figure 4.3. Mimics viewports of the Synbone mandible model reconstructed from the CT images, showing the (**a**) horizontal plane, (**b**) frontal plane, (**c**) sagittal plane, and (**d**) 3D part preview.

and symphysis) corresponds with the region that is most frequently subjected to resection (Shibahara et al., 2002; Coletti et al., 2009; Ettl et al., 2010; Gutwald et al., 2017). This defect represents the typical osteotomies performed during surgical treatment of advanced squamous cell carcinomas (Doty et al., 2004). The CAD volumes of the fully intact mandible and the cut-out segment defined as the defect were 77.8 cm^3 and 19.8 cm^3 , respectively.

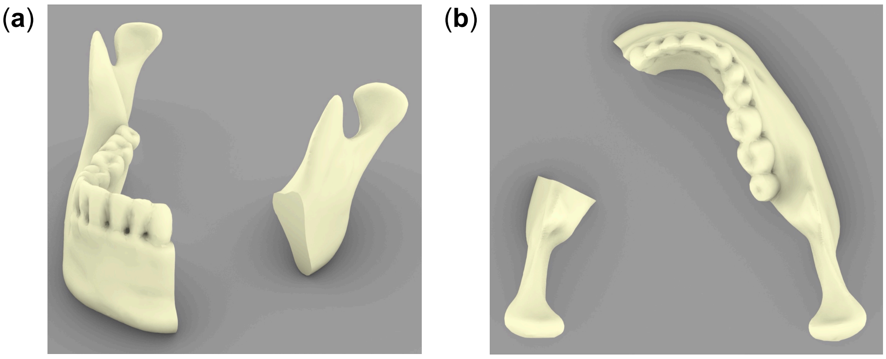

Figure 4.4. Isometric (**a**) and top (**b**) view of the mandibular lateral defect used in this research.

A surgical cutting and drilling guide was designed to aid the resection process in the experimental part of the study. Details on the designing of the surgical guide and its usage in the experimental implant fixation procedure are provided in Sections 4.6 and 4.8.3, respectively.

4.4.2. Shape estimation of resected segment

Several techniques to estimate the missing mandibular segment have been described in the literature, of which statistical shape modeling and (segmental) mirroring are the most commonly used ones (Al-Ahmari et al., 2015; Khalifa et al., 2016; Moiduddin et al., 2016; Moiduddin et al., 2017). A statistical shape model (SSM) can be used to describe a three-dimensional anatomical shape using a mean shape and its primary modes of variation. This mean shape and variation modes are extracted from a collection of training samples, which are typically obtained through segmentation of CT data. For this research, a training set was used, consisting of 35 mandibles segmented from full body CT-scans. Unbiased registration algorithms were used to find the mean mandible shape of the training data (Tümer et al., 2019). Similar to Procrustes analysis, iterative processes of translation, rotation and uniform scaling were applied to the different mandible shapes with respect to a set of corresponding landmark points sampled across the surface of the mandibles, in order to find the minimal distance between the shapes in the training set.

A covariance matrix can be computed from the data vectors that contain the coordinates of the points in the point cloud representing the mandibular surface. Principal component analysis (PCA) is then used to extract the main modes of variation by computing the eigenvectors of the covariance matrix. The modes of variation (eigenvectors) and the variance (eigenvalues) respectively represent the direction of shape change and the amount of variation in the corresponding direction. By choosing principal components within the population distribution, new shapes can be generated within the boundaries of the training set. This new shape x can be represented by a combination of the mean shape $\overline{x}$ and a weighted sum of the modes of variation Φ:

$$x = \overline{x} + \sum_{s=1}^{c} b_s \Phi_s \tag{4.1}$$

The weighting vector, also known as the 'shape parameter', b defines the influence on the mean shape for a given mode of variation. By fitting these shapes onto the patient mandible, the missing anatomy of the mandible can be estimated. Both SSM and mirroring techniques were investigated. First, the results of SSM will be briefly discussed, followed by the results of the segmental mirroring approach.

MATLAB (version 2018a) scripts for the SSM process were developed in-house in the past. The number of sampling points across the target bone ss_1 and fitted bone ss_2 can be adjusted to find an optimum fitting of the estimated mandible on the target mandible. After investigation of the application of SSM to the mandible model using various ss_1 and ss_2 parameter values it turned out that the newly generated 3D shapes did not accurately match the original shape of the mandible (Figure 4.5). This mismatch was most likely caused by the presence of teeth in the model, as the SSM script was developed, based on edentulous cases. Hence, optimization of the script was required to acquire more accurate results for all patient cases.

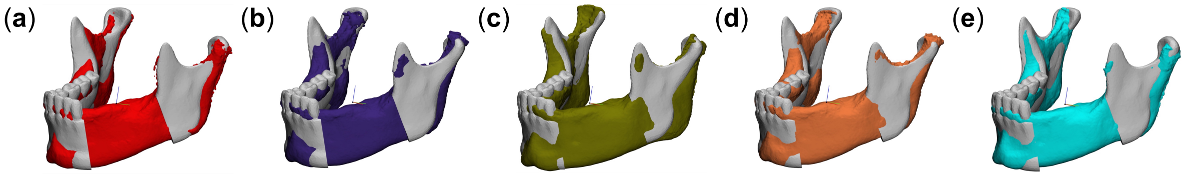

Figure 4.5. SSM results. The target mandible is shown in grey and the fitted mandible shapes are colored, where (**a**) $ss_1 = 400; ss_2 = 2400$, (**b**) $ss_1 = 100; ss_2 = 2300$, (**c**) $ss_1 = 100; ss_2 = 2600$, (**d**) $ss_1 = 100; ss_2 = 2100$, (**e**) $ss_1 = 600; ss_2 = 100$.

In the case of the mirroring method, the intact side of the mandible is mirrored across the midsagittal plane onto the region of defect. This midsagittal plane cuts between the two central incisors and the mandibular condyles. Advantages of the mirroring technique compared to SSM are that no additional database with training samples is required, and the procedure is faster as it can be implemented in the 3-Matic design workflow. However, mirroring is only possible if only one side of the mandible is affected, while the other side is still intact. For example, mirroring techniques are not applicable to central defects or lesions that cross the midline. Besides, the presence of asymmetry in the mandibular body, rami, and condyles hampers accurate regeneration of resected areas. In contrast, shape estimation through SSM is size and location independent.

A combination of the mirroring technique and anatomical extrusion technique was implemented in the current 3-Matic design workflow for shape estimation (Figure 4.6). First, the healthy side was mirrored to and then aligned with the affected side (Figure 4.6-b). Next, the missing segment was cut out of the mirrored side between the previously defined resection boundaries, and teeth were trimmed off (Figure 4.6-c). A centerline was created between the two boundary surfaces of the remaining mandibular segments to provide a path for the sweeping operation (Figure 4.6-d). Three curves are created around the surface of the mirrored segment, which served as intermediate contour profiles for the sweeping operation (Figure 4.6-e). The estimated shape was generated by using a sweep-loft operation from one remaining segment to the other following the sweep path and intermediate profiles (Figure 4.6-f).

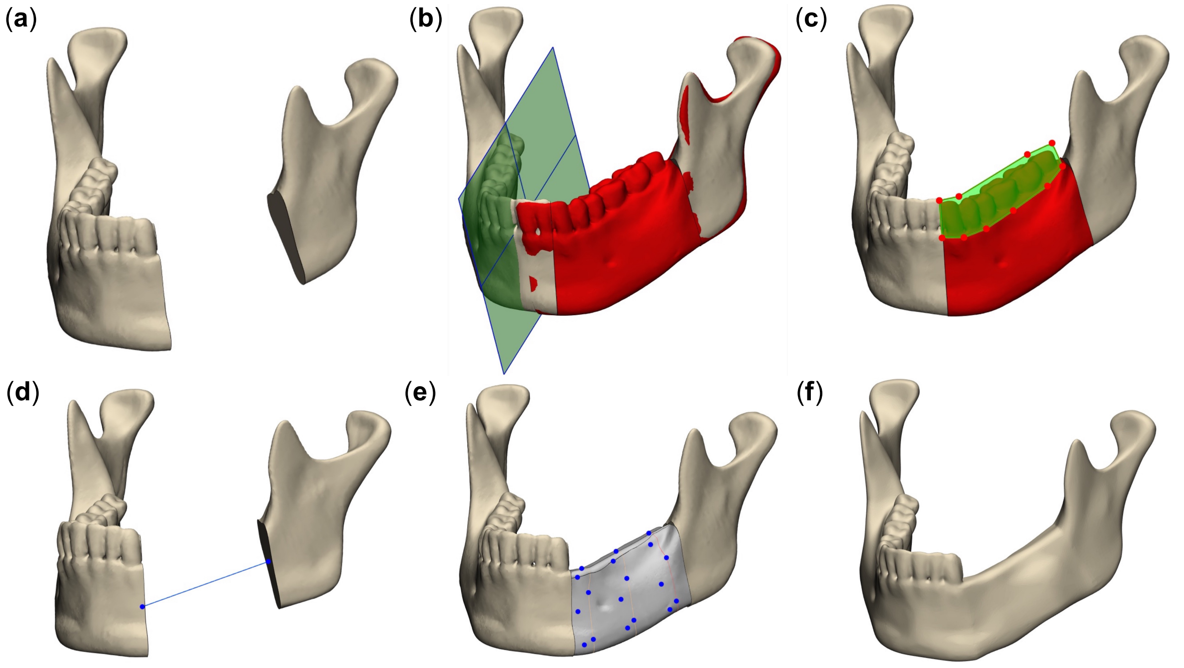

Figure 4.6. Shape estimation procedure, showing (**a**) segmental resection, (**b**) healthy-side mirroring (**c**) segmental cut-out and trimming of teeth, (**d**) creation of centerline, (**e**) creation of intermediate contour profiles, and (**f**) final result after performing sweep-loft operation.

The *Part comparison analysis* function in 3-Matic was used to visualize and quantify the difference between the estimated and original resected segment, thereby indicating the accuracy of the shape estimation technique. The function shows the surface deviation (SUD) in mm between two shapes, in this case the estimated and original segment. Figures 4.7-a and 4.7-b respectively show a lateral and medial view of the mandible subjected to part comparison analysis. The color spectrum indicates the surface of the estimated segment moving either inside (blue) or away from (red) the reference surface. It is evident that apart from the locations of the teeth, which were not present in the estimated segment, the amount of surface deviation was very small (-1 < SUD < 1) for the largest surface area. Clearly, the degree of surface deviation will be different each time the procedure is being performed, as it is influenced by the input of the user during the mirroring and sweeping procedures. However, repetition of the procedure with different user input gave SUD results at similar orders of magnitude at corresponding locations, thereby confirming the reliability of the shape estimation method.

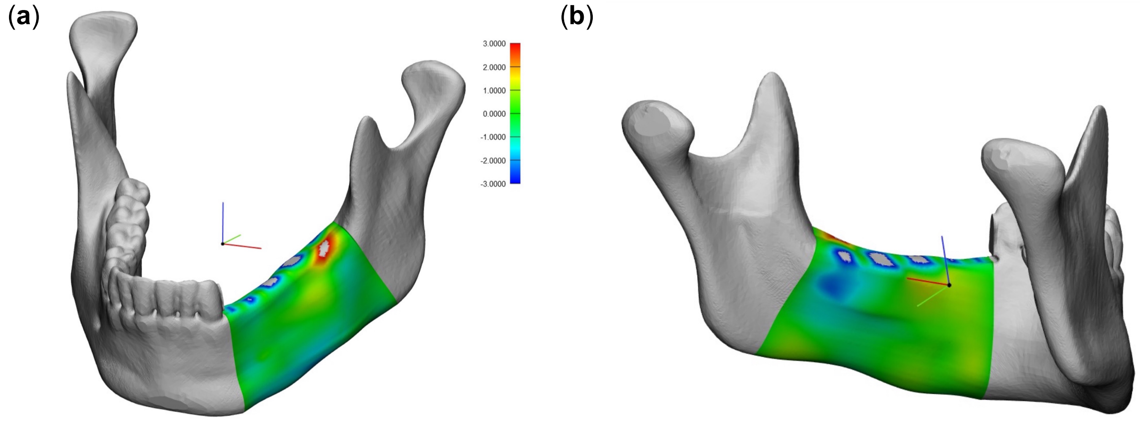

Figure 4.7. Lateral (**a**) and medial (**b**) views of the mandible with estimated segment subjected to part comparison analysis. Color bar shows surface deviation in mm.

4.4.3. Implant design requirements

Usually, the reconstruction procedure includes a planning phase in which the surgeon and engineer consider the resection options and define the overall shape and characteristics of the customized reconstruction implant. Many physiological and technical parameters are involved in these considerations, and sufficient feedback from the surgeon is essential in the design process.

Aitchison et al. (2009) defined a set of design requirements (or product design specifications) that generally apply to implantable orthopedic medical devices. These include (1) intended performance, (2) design attributes, (3) materials, (4) design evaluation, (5) manufacture, (6) testing, (7) instruments required, (8) sterilization, (9) packaging, and (10) information to be supplied by the manufacturer. The first requirement, intended performance, will be shortly discussed after this paragraph, followed by a comprehensive description of all the implant design features. Computational verification of the designs, and manufacturing and testing will be covered in Sections 5.1 and 5.2, respectively. Implants developed through the workflow discussed in this study do not require custom designed surgical instruments (drill bit, screwdriver, oscillating saw, etc.), because the instruments used for the standard plating systems in fibular free flap reconstructions can be used similarly here. Sterilization, packaging, and transfer of manufacturing information will only be relevant at a later stage and is not part of the current study, which focusses primarily on the development of the implant itself.

The ideal mandibular reconstruction would establish continuity, alveolar height, arch form, and width, allow dental implant installation and improve facial contours, thereby restoring swallowing, speech, mastication and aesthetics (Kumar et al., 2016). Although the possible reconstruction methods depend highly on the type of defect and the patient's state of health, these key functional and aesthetics criteria should always be leading. Satisfaction of these performance requirements depends to a large extent on the implant body geometry, which will be covered in the next Section.

4.4.4. Implant design features

The development of a mandibular reconstruction implant involves taking into account several design features. These are primarily about the general appearance and technical characteristics of the implant itself and should not be confused with the design requirements discussed earlier. The main design features that were encountered in the design process are represented in Figure 4.8. In what follows, each of these design features will be discussed in detail. As mentioned earlier, decisions on the overall implant geometry and positioning of the screws were made in close consultation with maxillofacial surgeons from the Erasmus Medical Center Rotterdam.

1. Implant material

The reconstruction implants will be made of Ti-6Al-4V (ELI grade 23). This titanium alloy is the current gold standard material for loadbearing orthopedic implants due to its high strength, low weight, good corrosion resistance and excellent biocompatibility properties (Elias et al., 2008). Besides, the titanium alloy is very suitable for metal 3D printing through SLM or EBM (S. Liu and Shin, 2019). Detailed information on the material and SLM manufacturing properties of the implants will be provided in Section 4.8.1.

2. Implant body geometry

The implants were designed in the shape of a cage or tray. This particular body shape is associated with several advantages, of which accurate reproduction of the natural shape of the mandible and insertion of PBCM grafts are the most notable. Implant height in the resected area should be somewhat lower than the native mandible, so that the implant can be covered with sufficient soft tissue without the need for an additional local flap (Qassemyar et al., 2017). However, the cage loaded with PCBM should be high enough for dental implants to be placed on top at a later stage, usually several months after surgery, in order to restore masticatory performance.

3. Implant thickness

Conventional reconstruction plates typically have a thickness ranging between 2.0 mm and 3.0 mm, and mini-plates typically below 2.0 mm. Cage thickness is usually not specified in the literature. Qassemyar

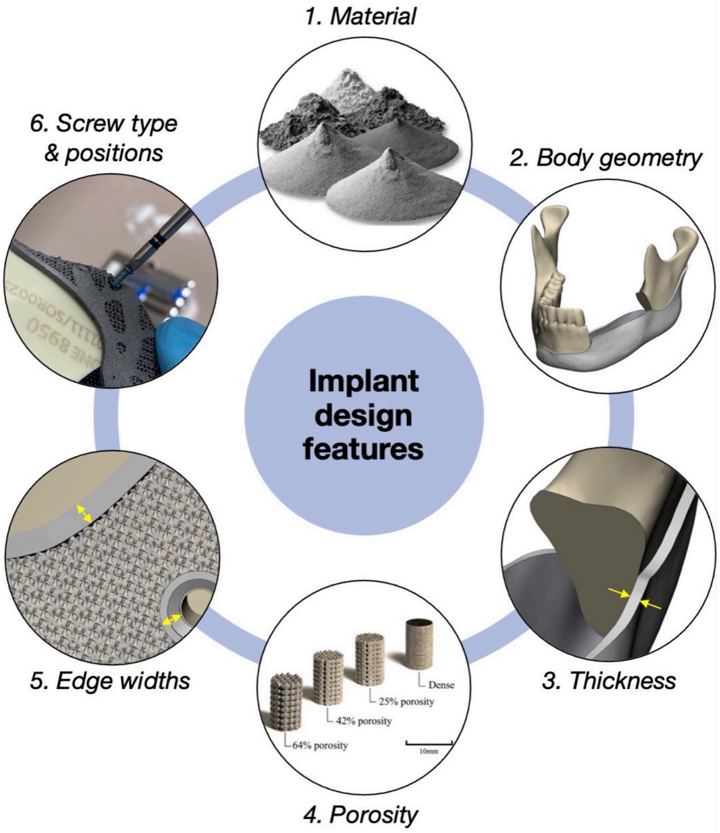

Figure 4.8. Implant design features.

et al. (2017) mentioned a thickness of 1.0 mm at the fixation wings of their custom implant. Johnson & Johnson developed a design procedure for 3D printed patient-specific titanium implants, including mandibular reconstruction cages (J&J, n.d.). The standard plate profile of these implants is 1.0 mm. P. Li et al. (2014) have developed an endoprosthesis with an appearance similar to that of a cage. Their implant had a general thickness 1.7 mm, which increased up to 2.5 mm in the areas of stress concentration. Given these examples from the literature, implant weight restrictions, and wearing comfort, the thickness of the current implant design was set at 1.5 mm.

4. Implant porosity

Porosity was implemented in the implant designs to reduce implant weight, decrease implant stiffness, and facilitate bone and tissue ingrowth. Instead of using simple one-dimensional holes, porosity is often designed in the implant in the form of a lattice structure to open up more space inside the material for tissue to grow into. To create a lattice structure, a unit cell of some type is spatially repeated along the principal directions (*x*, *y*, and *z*) of three-dimensional space. The type and dimensions of the unit cell need to be carefully determined since both aspects have a large influence on the mechanical, biological (e.g., osseointegration and bone tissue regeneration) and mass transport (e.g., diffusivity and permeability) properties of the implant. Lattice structures have not only been widely used in the biomedical field, but also the aerospace, automobile, civil and other engineering fields take advantages of their low density, high specific strength and stiffness, thermal insulation properties and excellent energy absorption abilities (Ashby, 2006; Ashby and Gibson, 1997).

The most important lattice parameters considered were the unit cell type, pore size, strut thickness, and porosity. The ‘dode’ unit cell type was chosen for the lattice structures in both implants based on promising previous studies on mandibular reconstruction implants implemented with lattice structures composed of dode unit cells (Moiduddin et al., 2019; Moiduddin et al., 2020). The first implant design included a lattice structure that extends throughout the entire implant volume, except for the solid edges around the screw holes and implant extremities, as discussed earlier. The second implant design was identical to the first, except for the solid volume that was added based on the results of the topology optimization.

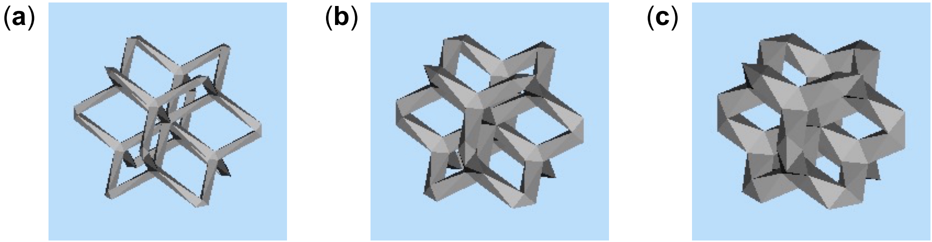

Figure 4.9. (**a**) Dode thin, (**b**) dode medium and (**c**) dode thick unit cell structures available in the Materialise Magics® software.

In Magics, three different versions of the dode unit cell type are available by default, namely the dode thin, dode medium and dode thick unit cell (Figure 4.9). The three different dode unit cell structures were investigated for the implant in this research. The unit cell size was kept constant at 1.5 mm. The pore and strut parameters for each of the dode structures are listed in Table 4.1. Based on the parameters from Table 4.1 and visualization of the structures in Materialise 3-Matic®, it became clear that the dode thin structure had a too high porosity and too small strut thickness, which would result in a too low mechanical strength. Therefore, only the dode medium and dode thick structures were considered. In theory, both types of structures could meet the requirements for adequate bone ingrowth and seemed sufficient after visual inspection with the Materialise 3-Matic® software. Therefore, two test samples, one implant with dode medium unit cells and the other implant with dode thick unit cells, were 3D printed and visually compared (Figure 4.10). Note that Figure 4.10 does not include the final lattice implant design, which includes countersinks and has smaller screw holes. It turned out that due to the smaller pores and thicker struts of the dode thick structure, some pore regions were not completely opened up due to trapped powder particles fused between the struts. These pore blockages are undesirable as they adversely affect the implant permeability. This was observed to a lesser extent in the dode medium structured implant. Besides pore connectivity, the medium structure is arguably preferred over the thick structure, because of its higher porosity and lower weight. Therefore, the 1.5 mm dode medium unit cell was selected for the final implant designs.

Table 4.1. Theoretical values for pore and strut parameters of three different dode unit cell structures.

	Dode thin	**Dode medium**	**Dode thick**
Pore size in-plane (μm)	590	460	320
Pore size smallest (μm)	420	325	230
Strut thickness (μm)	110	210	300
Porosity (%)	96.2	87.5	75.4

5. Implant edge widths

Most of the solid implant volume was replaced by a lattice structure in the two final implant designs. To ensure patient safety and sufficient mechanical performance, only a certain inner volume of the implant was made available for lattice structuring, leaving some edges to remain solid. These edges were located at the upper boundaries of the implant and around the screw holes. These solid edges provided the implant with extra mechanical strength and protected the patient from the sharp ends of the struts that would otherwise be sticking out. Based on estimations from implant designs provided in the literature as well as visual inspection of various widths, the solid edge width of the current design was set at 1.5 mm. This included a countersink width next to the screw holes.

6. Screw hole locations

For conventional reconstruction plates a minimum of three and preferably four bicortical screws are required on either side of the mandibulectomy for optimal resistance to deformation. (Smith, 2021). Most of the load will be carried by the screw located closest to the resection border. Failure of this screw will

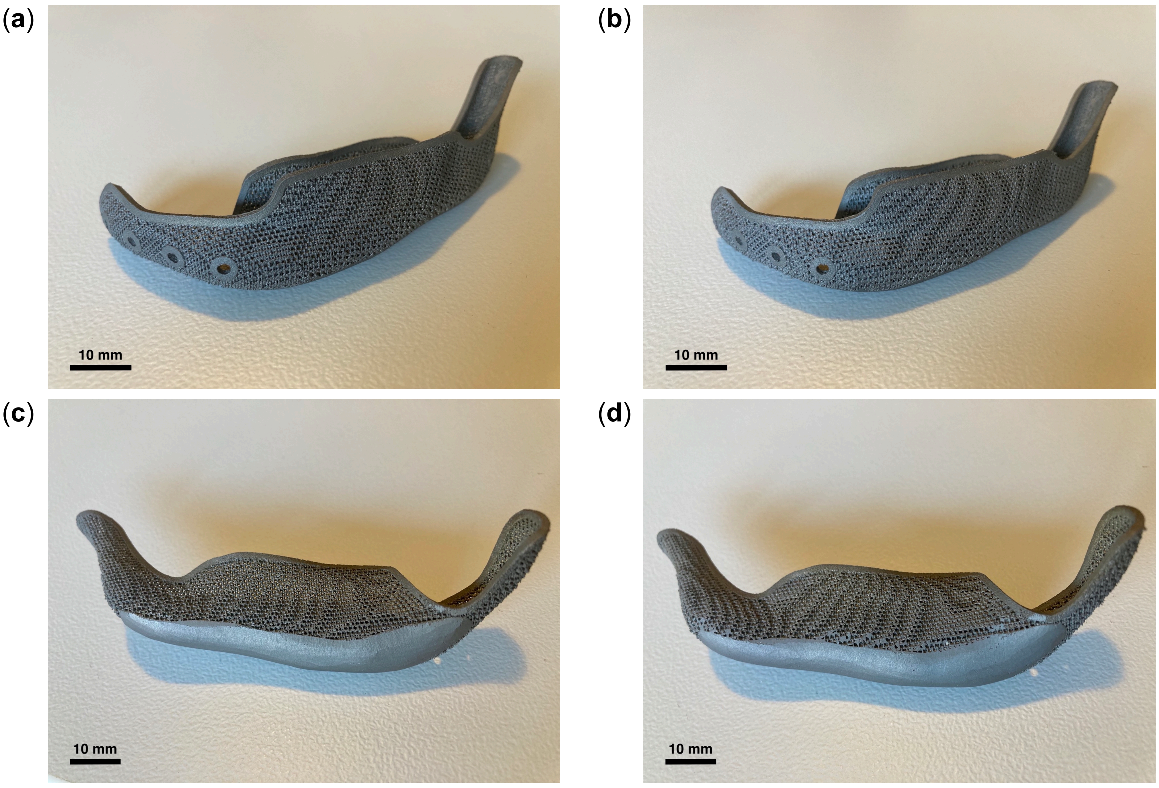

Figure 4.10. 3D printed implant test samples, with (**a**) dode-medium; lateral view, (**b**) dode-thick; lateral view, (**c**) dode-medium; medial view, and (**d**) dode-thick; medial view. Note that the final lattice implant design, which is not shown in this figure, includes countersinks and has smaller screw holes.

lead to an unstable system much faster if only three screws are used instead of four. This will be even more vital in the osteoporotic, infected, or atrophic cases (Klotch, 1995). Furthermore, it is important to note that for mechanical reasons the screw closest to the resection border should be positioned at least 5-7 mm away from the osteotomy line, as the bone density and vascularity surrounding the defect can be reduced (Klotch, 1995).

The minimum distance between two screws holes measured from the center has been reported for steel constructions (American Institute of Steel Construction, 2016). Since no such data is available in the literature for screw-to-screw distance in bone, it was assumed that the same methods could be applied to bone fixations. This source indicates that the distance between the centers of screw holes should not be less than $2\frac{2}{3}$ times the nominal screw diameter, and that a distance of 3 times the screw diameter is preferred. Therefore, a minimum screw spacing of 7.2 mm between the screw holes should be applied to the mandible model. For simplicity, the screw hole distance was set at 8 mm.

Taking the requisites for screw placement mentioned above into account, four screws were placed on the anterior body and four on the posterior border of the ramus (Figure 4.13). The options for different screw positions in the chin region were limited given the specified requisites and available amount of space. Therefore, these four screws were placed next to each other in the horizontal plane crossing the symphysis, similar to the conventional fixation plates that are used for mandibular resection or fracture repairs. The positions of the screws in the posterior mandible closely followed the lateral posterior border of the mandibular ramus, so that possible damage to the mandibular nerve and interference with tooth roots and possible future implants could be avoided.

7. Screw type

For this study 2.4 mm bicortical titanium cortex screws (MatrixMANDIBLE, DePuy Synthes®) were used to fixate the implants to the mandibles. Each implant will be fixed to the mandible by a total of eight screws with varied lengths. Screw lengths were determined by visual inspection in the mandible using 3-Matic. Four screws placed at the remaining anterior mandibular segment had a length of 14 mm. The two screws on the remaining posterior mandibular segment closest to the resection had a length of 8 mm. The two most distal screws on the posterior mandibular segment had a length of 5 mm.

4.5. Design workflow

The image processing and design steps were compiled into a Python-based workflow using the Mimics and 3-Matic Scripting Modules. The workflow is completely semi-automized in the sense that all the operations are automatically executed except when user input is required. All scripts were written to be compatible with Python version 3.8. The workflow starts with importing the DICOM image files and extends towards a solid implant design, ready to be exported to Abaqus/CAE for TO. Abaqus also offers a Python-based general user interface (GUI) toolkit, allowing the design workflow to be coupled to the FEA workflow in the future.

The Mimics and 3-Matic main windows are shown throughout the entire design process to allow for the manipulation of modules and to enable display regulation of objects in the viewport at all times. In order to collect user input, Abaqus supports GUI applications that group widgets and dialog boxes in a single layout. Mimics and 3-Matic do not have this option. Instead, the scripting module only provides message boxes that can instruct the user to do something outside the message window. A possibility to establish convenient user interaction would be to use Tkinter, a GUI toolkit built into the Python standard library. Tkinter applications can be relatively easily implemented in the scripts and contain all the required GUI widgets, including text boxes, buttons, entries, and labels. A combination of message boxes and Tkinter application windows will be used to guide the user through all the different steps in this workflow. In case the user is instructed to carry out a task in the viewport, an instructive example image will be provided for additional clarification. An example of this is shown in Figure 4.11.

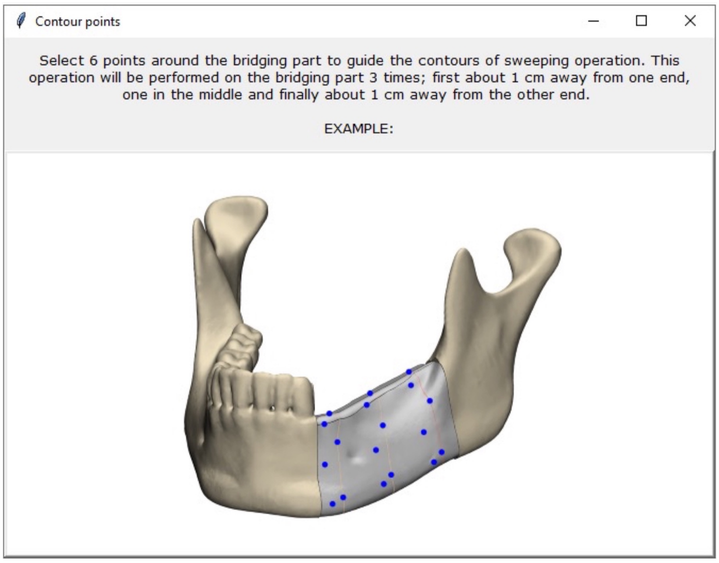

Select 6 points around the bridging part to guide the contours of sweeping operation. This operation will be performed on the bridging part 3 times; first about 1 cm away from one end, one in the middle and finally about 1 cm away from the other end.

EXAMPLE:

Figure 4.11. Tkinter pop-up window with instruction message and example image.

The main steps of the implant design workflow are shown in the flowchart of 4.12. More detailed descriptions of all the steps and user inputs are provided in Appendix A and B.

After the path has been set correctly, the DICOM images will be loaded into Mimics (Figure 4.12-a). Then, segmentation of the mandible will be performed using either HU thresholding alone (Figure 4.12-b) or, if necessary, with subsequent region growing (Figure 4.12-c). Region growing is a pixel-based segmentation tool used to get rid of extraneous (noise) structures around the part of interest. The user can inspect the mask and 3D part preview (Figure 4.12-d) and choose to refine the thresholding and/or region growing procedures if the results are not yet as good as desired. After obtaining satisfactory

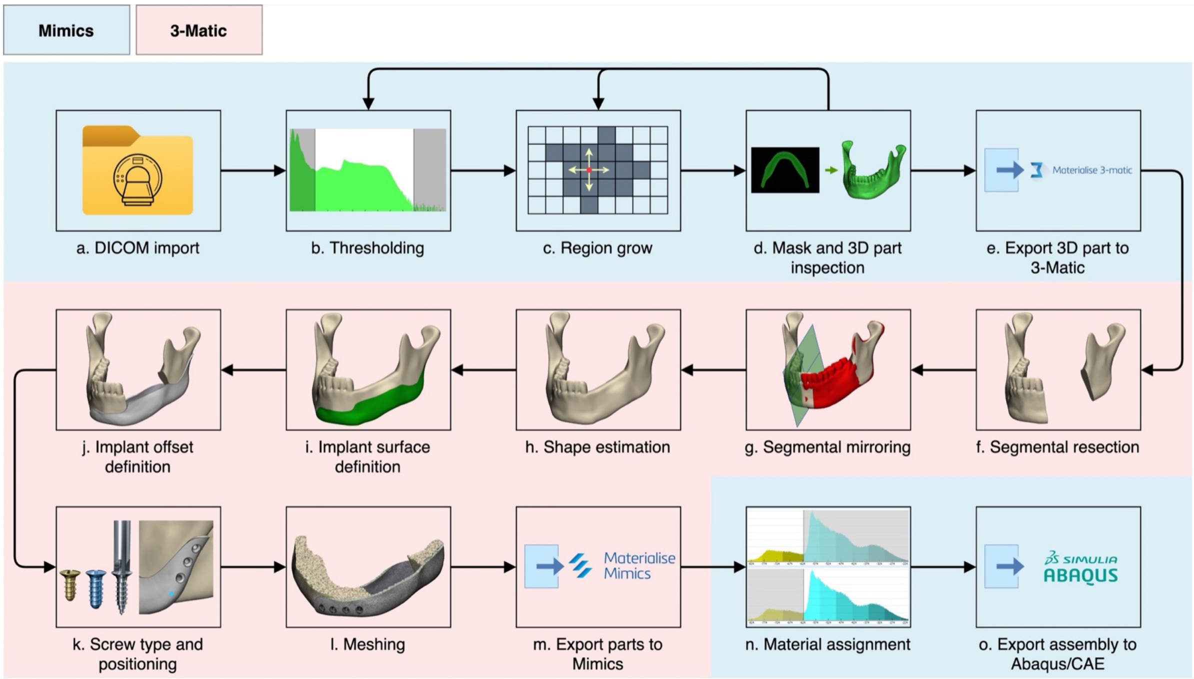

Figure 4.12. Flowchart showing the steps of the implant design workflow in Mimics and 3-Matic.

results, the 3D mandible part will be calculated and exported to 3-Matic where the script continues to run (Figure 4.12-e). The design part in 3-Matic comprises seven steps: segmental resection (Figure 4.12-f), segmental mirroring (Figure 4.12-g), estimation of the missing shape (Figure 4.12-h), marking of the implant outer surface (Figure 4.12-i), defining the implant thickness/offset (Figure 4.12-j), defining screw types and positions (Figure 4.12-k), and meshing (Figure 4.12-l). Volume meshes of the implant and mandibular segments are exported back to Mimics (Figure 4.12-m) where materials will be assigned to all the parts based on predefined lookup tables (LUT) (Figure 4.12-n). Finally, an assembly of the volume meshes will be exported as an input file (.inp) that contains the complete description of the numerical model (Figure 4.12-o). This file can be read by the Abaqus software for topology optimization.

The design module of 3-Matic contains a functionality that allows the user to perform lattice operations in a certain design space. However, the 3-Matic license owned by Delft University of Technology does not provide access to this functionality, so instead lattice structuring of the mandibular implant was performed in the Materialise Magics software, as mentioned earlier. Materialise Magics does not support Python scripting, so this part of the design process could not (yet) be implemented in the current Python script. After determining the dimensions of the solid extremities and unit cell type, as discussed in the previous Section, the lattice structure was allocated to the designated implant design space. Anterior and posterior oblique views of the lattice implant are shown in Figure 4.13-a and 4.13-b, respectively.

The TO implant is obtained by merging the results of the topology optimization of the solid implant with the design of the lattice implant. The geometry of the optimized result could not be used just by itself since the implant would then lose its cage structure and thereby the possibility to insert bone grafts. Detailed descriptions on the methodology behind the TO, and how the optimized structure is implemented in the final TO implant design, is provided in Section 4.7.5. Anterior and posterior views of TO implant are shown in Figure 4.13-c and 4.13-d, respectively.

4.6. Surgical cutting and drilling guide

Based on the final implant designs a surgical guide was developed in 3-Matic (Figure 4.14). Note that this surgical guide was not designed to be suitable for clinical application as a patient-specific anatomy

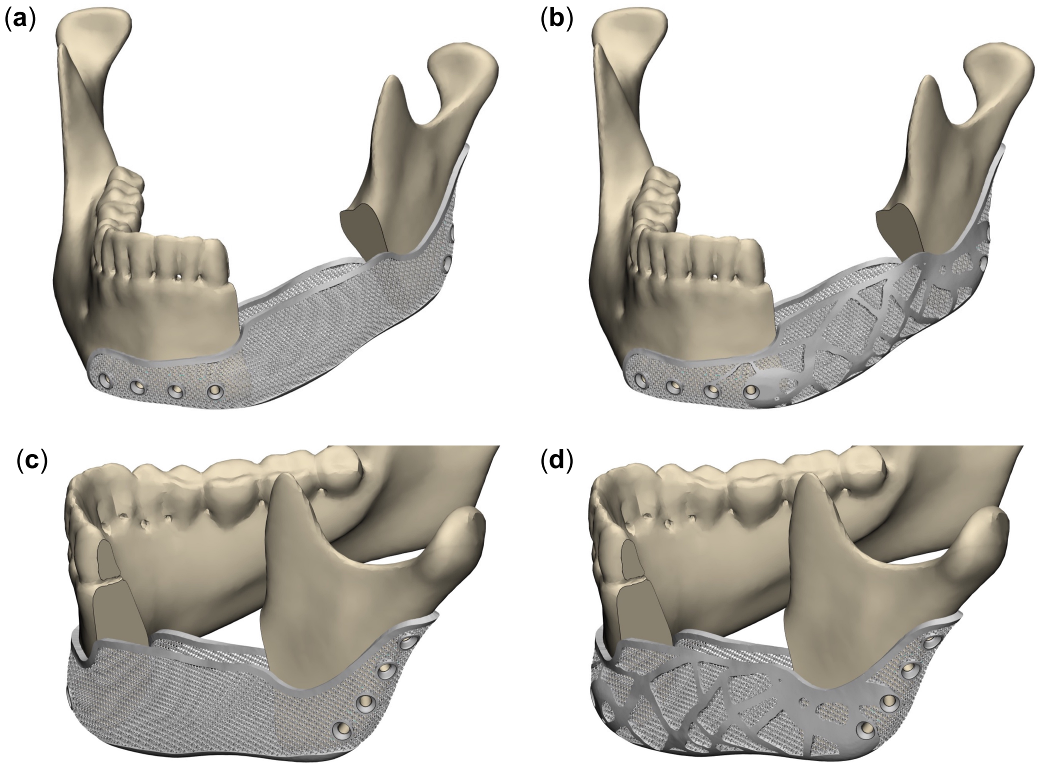

Figure 4.13. (**a**) Anterior view of the lattice implant, (**b**) anterior view of the TO implant, (**c**) posterior view of the lattice implant, and (**d**) posterior view of the TO implant.

was lacking. Two slits were created with an opening narrow enough for a surgical oscillating saw to accurately cut the mandible at the predefined cutting planes. Eight holes were present at the locations that corresponded to the locations of the screw holes inside the implants. Insertion of self-tapping 2.4-mm screws in dense cortical bone required predrilling with a 1.8-mm drill bit. Therefore, the cylindrical apertures present in the surgical guide had a diameter of 2 mm to enable smooth insertion of the drill bit.

The guide could be clicked onto the mandible and, if necessary, secured tightly with two screws on the lateral side of the mandible. The guide could be reused for each of the sample preparation procedures so that only one copy had to be printed. The design process for the surgical guide is not yet included in the semi-automatic workflow and remains to be done in future work.

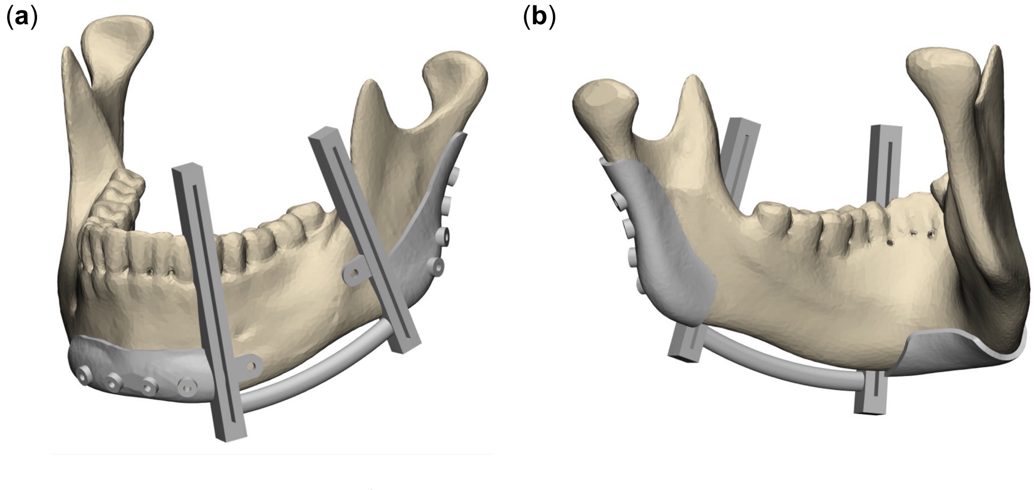

Figure 4.14. (**a**) Lateral and (**b**) medial views of the surgical cutting and drilling guide.

4.7. FEA methods

As discussed in the introduction, it is very difficult to create an experimental setup that closely mimics the physiological biomechanics of the mandible. For that reason, multiple simplifications had to be made in the experimental setup. There are two main differences between the experiment and the actual physiological situation. First, uniaxial loading with a loading bar was used in the experiments as compared to multidirectional forces produced by the muscles in the human body. Secondly, for convenience, consistency, and reproducibility of the experiments a synthetic mandible analog was used. Even though this bone analogue has been proven to be a reliable substitute for cadaveric bone, its mechanical properties differ from real bone which is stronger due to its complex composition. Because of these differences, the experimental data cannot be directly compared to a FE model that attempts to simulate physiological conditions (i.e., with an extensive musculatory system, and heterogenous bone properties). Therefore, a FE model that matched the experimental conditions was developed first. By doing so, two validation steps would be integrated into the FEA process. First, the FE model that reproduced experimental conditions was validated one-to-one with experimental data. Afterwards, this FE model was extended to include the more sophisticated physiological conditions. This FE model that reproduced the physiological conditions would in turn be compared with the FEA data published in the literature.

The healthy intact mandible was used for the initial validation step of the FEA under experimental conditions. Four different models were investigated with FEA under physiological conditions, where the first model included the healthy intact mandible, the second model included the resected mandible model with the solid implant, the third model included the resected mandible model with the lattice implant, and the fourth model included the resected mandible model with the topology optimized (TO) implant. These four models will from now on be denoted as ‘healthy-model’, ‘solid-implant-model’, ‘LA-implant-model’ and ‘TO-implant-model’, respectively.

In what follows, FEA methodologies will be described in two parts, first for the FE models with physiological conditions and secondly for the FE models with experimental conditions. All FE analyses were performed using Abaqus/CAE 2019 (Dassault systèmes, Johnston, RI, USA). The topology optimization was performed using Abaqus/CAE 2017.

4.7.1. Material assignment

Physiological conditions

The Synbone mandible analog comprises two predefined regions of cortical and cancellous bone-like material. These variations in bone density can be captured in the grey values from the CT data and approximated with real bone material properties. Mimics was used to assign linear-elastic material properties to the volumetric meshes of the mandible and implant produced in 3-Matic. The material assignment method used for the mandible is ‘Grey value based’, which means that Mimics calculates a grey value for each volume element after determining the voxel intersections and after producing a weighted average grey value for each element. Two material types were created, one for the cancellous bone region and the other for the cortical bone region. The total number of materials to describe all volume elements in the mandible was 15, of which the first 5 materials made up the smaller cancellous region and the last 10 materials made up the larger cortical region of the mandible. The distribution of elements between the 15 materials is shown in Figure 4.15.

Grey values are expressed in HU, a scale that describes the radiodensity according to the following expression:

$$HU = 1000(\frac{\mu - \mu_{water}}{\mu_{water}}) \tag{4.2}$$

where μ and μ_{water} denote the linear attenuation coefficient of the material of interest and water, respectively. The synthetic (PU) mandible model that was used in this research produced different HU values compared to a mandible made of real bone. The HU values ranged from around -870 to -170.

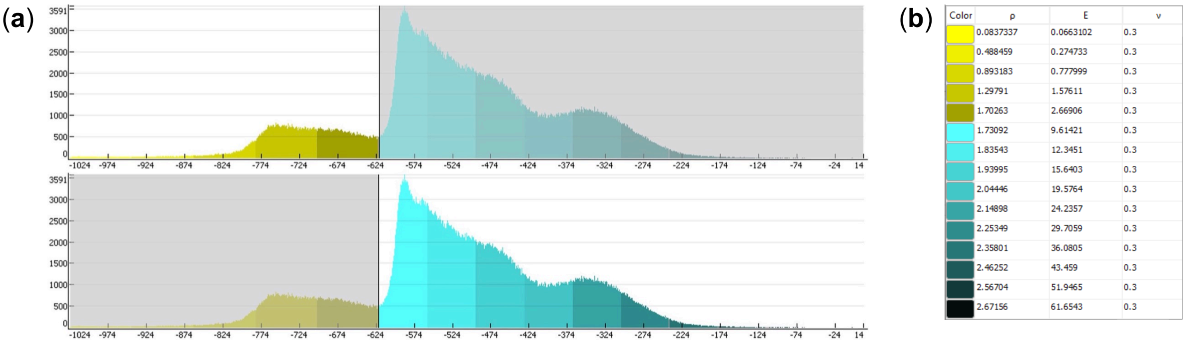

Color	ρ	E	ν
🟨	0.0837337	0.0663102	0.3
🟨	0.488459	0.274733	0.3
🟨	0.893183	0.777999	0.3
🟨	1.29791	1.57611	0.3
🟨	1.70263	2.66906	0.3
🟦	1.73092	9.61421	0.3
🟦	1.83543	12.3451	0.3
🟦	1.93995	15.6403	0.3
🟦	2.04446	19.5764	0.3
🟦	2.14898	24.2357	0.3
🟦	2.25349	29.7059	0.3
🟦	2.35801	36.0805	0.3
🟦	2.46252	43.459	0.3
🟦	2.56704	51.9465	0.3
⬛	2.67156	61.6543	0.3

Figure 4.15. Element distribution across the 15 materials assigned to the mandible. The first 5 materials (**a-top**) correspond to the cancellous bone region and the last 10 materials (**a-bottom**) correspond to the cortical bone region. (**b**) The color scale with corresponding material properties is shown on the right.

HU < -620 and HU > -620 were used to define cancellous bone and cortical bone, respectively. Calculations of the density and elastic moduli from the HU values for mandibular bone are reported in the literature (Ay et al., 2013). Since the HU values are different for the synthetic mandible, these equations are inapplicable in this case and had to be adjusted in order to obtain values that match the average values for density and elastic modulus of real mandibular bone. For cancellous bone, the material properties were calculated using the following equations:

$$\rho = 5 + 0.005HU \tag{4.3}$$

$$E = 0.06 + 0.9\rho^2 \tag{4.4}$$

This resulted in ρ-values ranging from 0.08 to 1.70 g/cm^3 and E-values ranging from 0.07 to 2.67 GPa for cancellous bone. For cortical bone, the material properties were calculated using the following equations:

$$\rho = 2.7 + 0.00165HU \tag{4.5}$$

$$E = 0.09 + 0.9\rho^{4.3} \tag{4.6}$$

This resulted in ρ-values ranging from 1.73 to 2.67 g/cm^3 and E-values ranging from 9.61 to 61.65 GPa for cortical bone. In the case of the implanted mandibles, the mandible material assignment was performed similarly for both remaining bone segments.

A problem often encountered when assigning material properties to bone models or other types of tissues is caused by a phenomenon called partial volume effect (PVE). PVEs result from the fact that a single voxel may contain different types of tissues or materials due to the finite spatial resolution of the CT scanning device (Tohka, 2014). Not only does this complicate the segmentation process, but it also adversely affects the FEA (Poelert et al., 2013).

The effects of PVEs were also observed during the assignment of materials to the mandible model in this study (Figure 4.16). Underestimation of material properties occurs to the elements on the outer mandible surface where two materials of highly different densities, namely air and bone, occupy the same voxel. For the elements that correspond to those voxels, the average density of both materials is being computed (Abel et al., 2013). Consequently, nearly all elements on the outer surface of the mandible (Figure 4.16-a) are assigned with a density that is much lower than their actual density. A method to avoid such partial volume artefacts is by limiting the assignment to a mask that is reduced such that the outer boundary layer of voxels is excluded. A separate material, in this case cortical bone, can then be assigned to the excluded boundary elements (Figure 4.16-b). The elastic modulus of this outer layer is set at E = 30.1 GPa, which corresponds to the average elastic modulus of the dentulous mandibular cortex as determined by Ay et al. (2013).

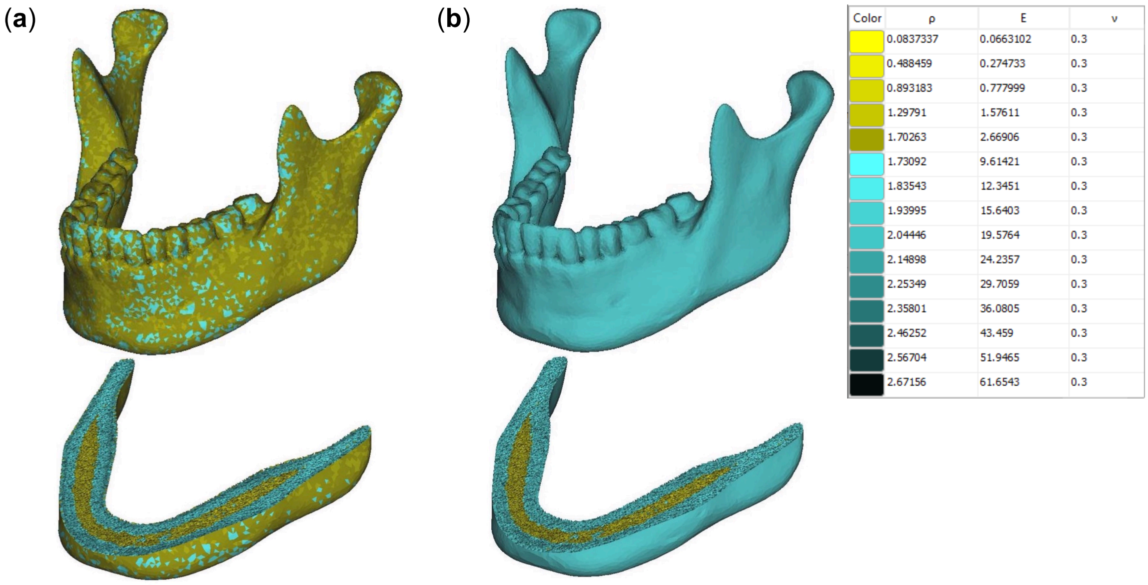

Color	ρ	E	ν
🟨	0.0837337	0.0663102	0.3
🟨	0.488459	0.274733	0.3
🟨	0.893183	0.777999	0.3
🟨	1.29791	1.57611	0.3
🟨	1.70263	2.66906	0.3
🟦	1.73092	9.61421	0.3
🟦	1.83543	12.3451	0.3
🟦	1.93995	15.6403	0.3
🟦	2.04446	19.5764	0.3
🟦	2.14898	24.2357	0.3
🟦	2.25349	29.7059	0.3
🟦	2.35801	36.0805	0.3
⬛	2.46252	43.459	0.3
⬛	2.56704	51.9465	0.3
⬛	2.67156	61.6543	0.3

Figure 4.16. Full and cross-sectional views of the material assignment to the healthy mandible model (**a**) subjected to partial volume artefacts, and (**b**) with the outer boundary layer of voxels assigned separately.

The elastic modulus of Ti-6Al-4V alloy ranges between 100 to 130 GPa (Y. Lee and Welsch, 1990). Therefore, the entire implant volume is assigned with an elastic modulus of E = 120 GPa. A Poisson's ratio of ν=0.3 was assigned to all volume elements of both the mandible and implant.

Elastic moduli, Poisson's ratios and mass densities were imported into Abaqus. All materials were modelled as linear elastic and isotropic.

Experimental conditions

Koper et al. (2021) performed FE analysis on the same Synbone mandible analogue that was used in this study, and they assigned standard values for the Young's modulus (0.50 GPa) and Poisson's ratio (0.3) of PU to the full cortical part of the model. The cancellous region was left empty, as its low stiffness would not contribute significantly to the stress distribution in the implant. Similarly, for this study the cancellous region was assigned with a neglectably low Young's modulus of 1E-6 GPa as to imitate cavity. The Young's modulus of the cortical bone region was chosen such that the stiffness of the model would match the stiffness as derived from the experimental data. Using this approach, a Young's modulus of 0.41 GPa was found for the cortical PU region. Poisson's ratio was set at 0.3.

4.7.2. Loads and boundary conditions

Physiological conditions

For this study, two types of clenching movements were simulated in all physiological models: incisal clenching (INC) and right molar biting (RMB) at the unaffected side. For the INC condition, 127 nodes on the incisal surfaces of the central and lateral incisors were restrained from moving vertically (i.e., perpendicularly to the occlusal plane). For the RMB condition, 68 nodes on the occlusal surfaces of the first and second molar were restrained from moving vertically. For both biting movements, 112 nodes on the articular surface of the temporomandibular joints were restrained in all directions. Boundary constraints for the two loading conditions are shown in Figure 4.17.

Pinheiro and Alves (2015) have described the expected reaction forces on the teeth involved with both biting conditions, i.e. INC and RBM. The magnitudes of these reaction forces are 570.90 N and 600.40 N for INC and RMB, respectively. These forces are based on average maximum single tooth bite forces of young male adults. Similar to Pinheiro and Alves (2015), four different muscles (masseter, temporalis, medial pterygoid, and lateral pterygoid) were modelled bilaterally through three-dimensional

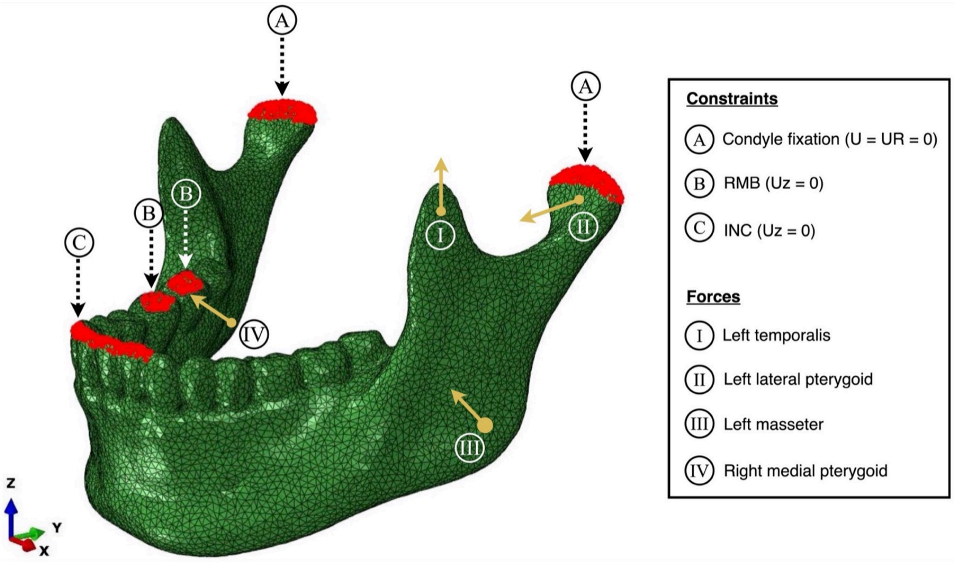

Figure 4.17. Representation of the boundary constraints and resultant muscle force directions for the INC and RMB clenching tasks in the physiological FE model. For simplicity, muscle force vectors are partly shown on the left and right side of the mandible.

force vectors. In the case of the healthy mandible all four muscles were used bilaterally to create the required loading condition. Each muscle force was applied to one control node on the surface of the model. This control node was constrained to several surrounding slave nodes using rigid beam multipoint constraints (MPC). This was done to distribute the force over a larger area, thereby resembling the muscle insertion area more accurately and preventing high stress gradients imposed by concentrated (point) loads.

For some segmental resections, muscles can be (partially) reattached to the mandible, which can then (to a limited extent) continue their function after implantation. The remaining muscle force after mandibular reconstruction has been reported to be 60% of the average biting force of healthy adults (Moghaddam et al., 2016). However, this value clearly varies for each individual, depending on the area of resection and the shape of the implant. Generally, segmental resections in the anterior part of the mandible are more likely to be restored with (partial) reattachment of all four masticatory muscles described earlier, as they will not be removed in the first place. The implant used in this study covers an area on the posterior mandibular segment that, according to surgical feedback, makes reattachment of both the left masseter and the left medial pterygoid very unlikely. Therefore, the forces exerted by those muscles will also be excluded from the loading conditions in the FE simulation. The masticatory function of the mandible is in this case dependent on the forces exerted by the remaining muscles, which remain unaffected by the surgical procedure.

Since two muscles will not be reattached to the affected side of the mandible, the remaining muscle force might be lower than 60% of the original maximum muscle force. Since the exact reduction in muscle force cannot be predicted, a general 'worst-case' scenario is simulated to ensure good mechanical implant performance in the long term. Therefore, the maximum biting forces described above are still reduced by 40% as described in the literature, leading to a reaction force of 342.54 N and 360.24 N for incisal clenching and right molar clenching, respectively. All individual muscle forces are scaled based on the desired clenching movement. The weighting factors of each muscle, as well as the scaling factors that provide the muscle activation force, are specified in the work of Korioth and Hannam (1994). Pinheiro and Alves (2015) positioned their mandible model in their coordinate system according to cephalometric standards. The mandible model in this research was positioned such that it could match the reference frame used in the paper of Pinheiro and Alves (2015) as accurately as possible so that no new direction cosines of the unit vectors would have to be computed. Instead, the muscle forces could simply be scaled uniformly until the desired reaction forces on the teeth were produced. For INC and RMB, those scaling factors were 0.72 and 0.87, respectively.

The orthogonal directions, the muscle forces and the scaling factors for different clenching tasks used in this research led back to those reported in Korioth and Hannam (1994). Hence, the displacement patterns of the healthy-model were compared with the displacements obtained by Korioth and Hannam (1994).

The three-dimensional force vectors of each muscle group for the two loading cases, as well as the number of nodes to represent each muscle group are listed in Table 4.2 for the healthy-model and in Table 4.3 for the implanted model.

Table 4.2. Muscle forces in three directions for incisal and right molar clenching in the healthy-model. Resultant force vectors at their respective area of insertion are shown in Figure 4.17.

	# Nodes	**Incisal clenching (N)**			**Right molar clenching (N)**		
		x	*y*	*z*	*x*	*y*	*z*
Left lateral pterygoid	21	-131,87	-146,00	-23,24	-30,89	-37,14	-8,50
Left masseter	24	88,25	-78,49	269,34	56,83	-34,19	155,75
Left medial pterygoid	24	-213,95	-164,23	348,19	-57,53	-44,17	93,54
Left temporalis	22	12,19	15,78	60,48	38,44	60,04	178,40
Right lateral pterygoid	24	131,87	-146,00	-23,24	14,23	-17,18	-3,90
Right masseter	23	-88,25	-78,49	269,34	-68,20	-41,13	186,90
Right medial pterygoid	22	213,95	-164,23	348,19	80,52	-61,78	131,02
Right temporalis	19	-12,19	15,78	60,48	-45,64	72,89	211,98

Table 4.3. Muscle forces in three directions for incisal and right molar clenching in the three implanted-models. Resultant forces are set at 60% of the healthy average maximum muscle force. Resultant force vectors at their respective area of insertion are shown in Figure 4.17.

	# Nodes	**Incisal clenching (N)**			**Right molar clenching (N)**		
		x	*y*	*z*	*x*	*y*	*z*
Left lateral pterygoid	21	-148,52	-164,43	-26,18	-24,64	-29,63	-6,78
Left masseter	-	-	-	-	-	-	-
Left medial pterygoid	-	-	-	-	-	-	-
Left temporalis	22	13,74	17,78	68,12	30,67	47,90	142,32
Right lateral pterygoid	24	148,52	-164,43	-26,18	11,35	-13,71	-3,12
Right masseter	23	-99,39	-88,40	303,33	-54,41	-32,81	149,11
Right medial pterygoid	22	240,95	-184,96	392,14	64,24	-49,29	104,53
Right temporalis	19	-13,74	17,78	68,12	-36,41	58,15	169,11

Experimental conditions

The loading bar was modeled as an undeformable rigid object, given its high stiffness compared to that of the PU bone sample. It exerted an equal force on both sides of the mandible by giving its reference point a displacement in the z-direction of 5 mm (Figure 4.18). This distance was enough to cover at least the full linear trajectory of the load-displacement curve obtained with biomechanical experiment. Movements and rotations of the bar were fully constrained in all other directions.INC biting was modeled using the boundary conditions identical to those used in the physiological model. That is, 127 nodes on the incisal surfaces of the central and lateral incisors were restrained from moving vertically (i.e., perpendicularly to the occlusal plane) and 112 nodes on the articular surface of the temporomandibular joints were restrained in all directions. A friction coefficient of 0.2 was used for the interface between the bar and bone.

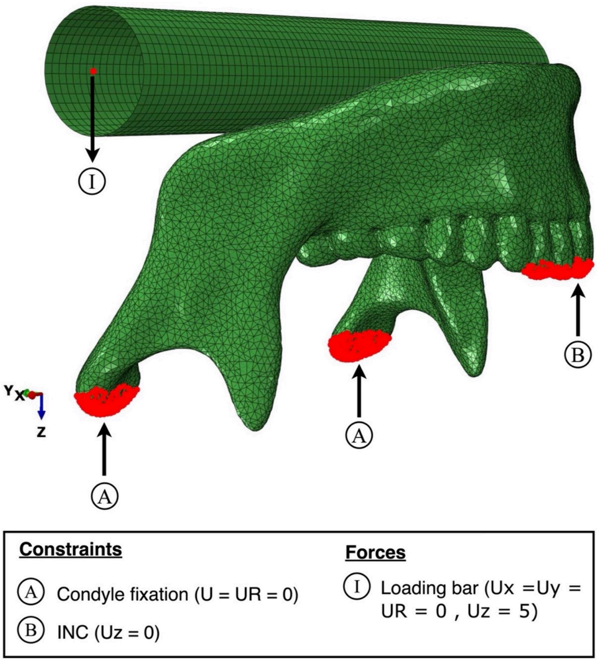

Figure 4.18. Setup of the FE model with experimental loads and boundary conditions.

4.7.3. Modeling of screws with rigid beam elements

Implementation of physical screws in the physiological FE model using “tie” contact definitions would most likely be the most accurate way to model the bone-screw and implant-screw interactions (Safi et al., 2010). However, given the large amount of computational power this method would require, it would make more sense to leave out the physical screws and model rigid beam constraints between the screw holes in the mandible and implant instead, assuming that the results would not differ significantly. No significant difference was found between the accuracy of both methods, as demonstrated in a technical document reported internally.

The procedure to model the screws by defining rigid beam elements goes as follows:

1. Define two reference points, each representing the head and tail part of the screw that lies inside the implant and mandible, respectively.
2. Define a rigid beam multi-point constraint between both reference points.
3. Define a coupling constraint (kinematic, U1=U2=U3=RU1=RU2=RU3=0) between each reference point (master) and the elements of the corresponding screw surface (slave).
4. Repeat steps 1-3 for all eight screws.

4.7.4. Meshing

Generation of surface and volume meshes on the intact mandible, resected mandible and implants was performed in the 3-Matic software. The mandible was meshed using 4-node tetrahedral elements (C3D4) in all four models under physiological conditions as well as in the model with experimental conditions. C3D4 elements were also generated for the implants but were converted to 10-node quadratic (C3D10) elements in Abaqus to increase accuracy. However, the solid implant was meshed using

C3D4 elements for the topology optimization procedure. Compared to using C3D10 elements for the solid implant, the resulting structure after optimization was nearly identical when using C3D4 elements, and the computational time was reduced by more than a factor 2 from 38 to 18 hours.

The elements generated for the mandible and the solid implant had a maximum triangle edge length (MTEL) of 2.0 mm and 1.0 mm, respectively (Figure 4.19). A gradient mesh was applied around all the screw holes on both the outer and inner surface of the implant. This means that the element density was higher near the border of the screw hole, and gradually decreased towards the standard 1.0 mm element size when moving further away from the hole. This gradient meshing was applied under the assumption that the loads would be transferred from the mandible to the implant mainly via the screws, and therefore high stresses would be present in close proximity to (some of) the screw holes. The element size of the lattices in the lattice and TO implant were based on a mesh convergence study that will be discussed next.

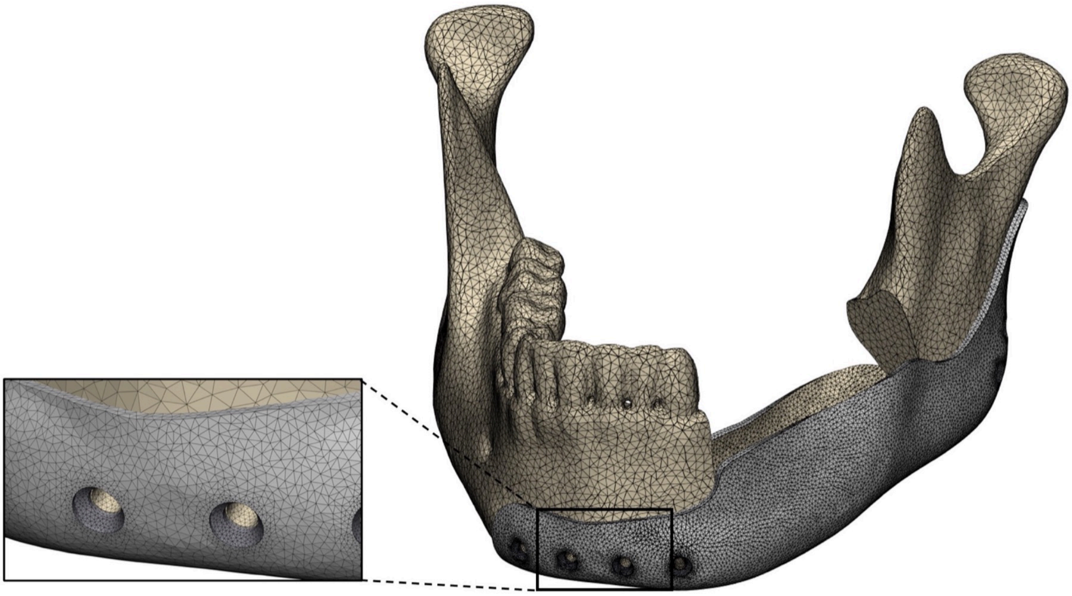

Figure 4.19. Overview of the surface mesh applied to the mandible (C3D4, MTEL = 2.0 mm) and solid implant (C3D10, MTEL = 1.0 mm) in the case of the solid-implant-model.

As mentioned earlier in the report, the accuracy of the results of a FEA depends largely on the element density used, especially in the case of complex geometries such as a lattice structure where rapid variations of stress may occur between or within the struts. A mesh convergence study was performed to make sure that the FE simulation results would be practically mesh independent. Mesh independency means that if two meshes with a different element density give the same result, you have more certainty that the model produces a mathematically accurate solution. It is computationally very expensive to perform a sensitivity study on the full model geometry. Besides, the locations of the high-stress regions, and thus the regions that require a finer mesh, can be predicted from a relatively course mesh density. Therefore, a mesh sensitivity analysis was performed on a section of the implant next to the first posterior screw, which corresponds to the area in which the predicted stress values were the highest (Figure 4.20).

Stress singularities are the locations in the FE mesh at which the stress does not converge towards a specific value. Instead, the stress will continue to increase, even when the mesh keeps being refined and the element size gets smaller. Consequently, the stress at a singularity is infinite in theory. Such stress singularities are frequently generated by sharp structural changes like cracks or corners. The strut junctions in the lattice structure of the mandibular implant contain sharp corners that give rise to stress singularities at these locations, as the stress continues to rise without convergence at finer mesh sizes (Figure 4.21). The actual geometry of the printed implants will not contain such sharp corners, but

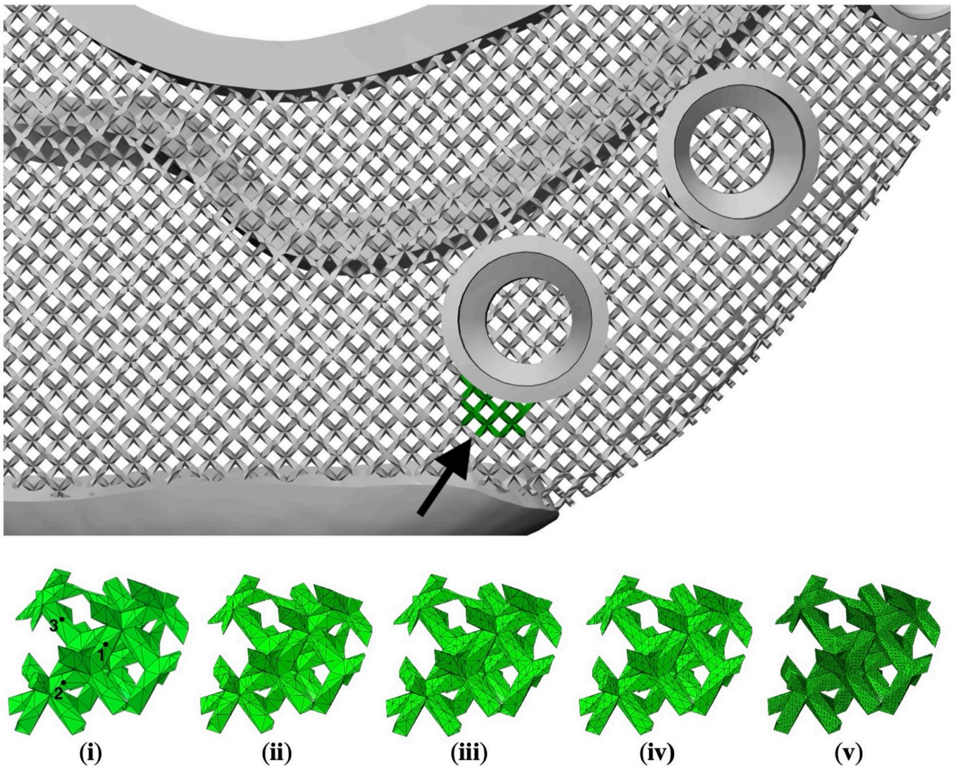

Figure 4.20. Area of the lattice implant that was analyzed with different mesh densities (shown in green), with (**i**) MTEL = 0.30 mm, (**ii**) MTEL = 0.25 mm, (**iii**) MTEL = 0.20 mm, (**iv**) MTEL = 0.15 mm and (**v**) MTEL = 0.05 mm. Numbered black dots in (**i**) correspond to the three nodes at which stress values were extracted for each mesh density.

small fillet radii will be present. However, introducing fillets in the numerical model is not reasonable as it will massively increase the model size due to the extremely large number of elements required. And even though the predicted stresses close to these singularities will be inaccurate, it will not significantly affect the overall response of the model if adequate mesh convergence is established (Zienkiewicz et al., 2005). The high nodal stress values obtained at the corners are the result of inaccuracies in the FEA solution and are non-realistic. For that reason, the stress values at those junction areas should not be considered for the prediction of implant failure, nor should they be guiding the mesh convergence analysis. For the sensitivity study, stress values were compared between the various mesh densities at corresponding nodes in the middle of the struts.

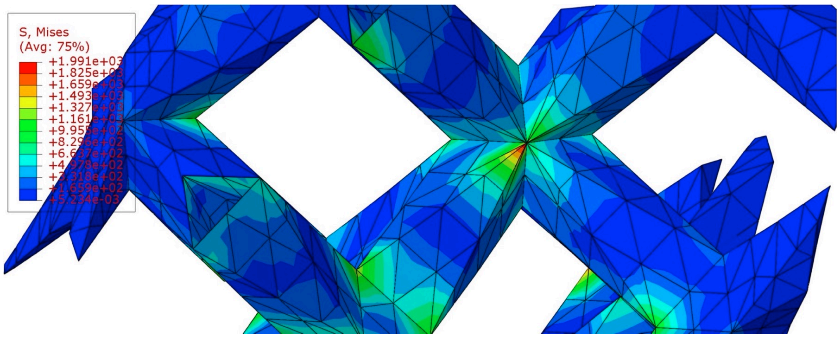

Figure 4.21. Example of stress singularity located at a strut junction.

Middle nodes on three different struts were investigated, where each strut was oriented in a different spatial direction. These three nodes are highlighted in Figure 4.20-i. In this way, loads propagating through the struts in different spatial directions can be accounted for. Figure 4.22 shows the nodal von Mises stress values at the various element sizes for nodes 1, 2 and 3. The element size is expressed in terms of maximum triangle edge length. The von Mises stresses and element size reduction factors are normalized with respect to the values obtained for the coarsest mesh.

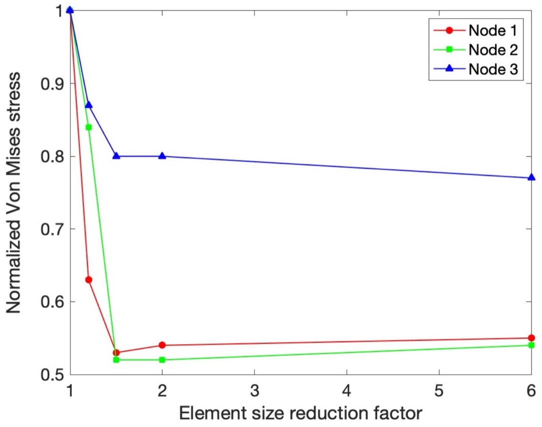

Figure 4.22. Mesh convergence results. All results are normalized with respect to the values obtained by the coarsest mesh (MTEL = 0.3 mm).

Based on Figure 4.22, the lattice structure was meshed with MTEL = 0.15 mm. The solid parts (i.e., the non-lattice structured volume) in the lattice implant and TO implant require a less refined mesh and are therefore meshed with MTEL = 0.4 mm in order to save computational time. A zoomed-in image of the mesh at an anterior region of the TO-implant-model is shown in Figure 4.23. An overview of the meshing parameters for each part in the different models is provided in Table 4.4.

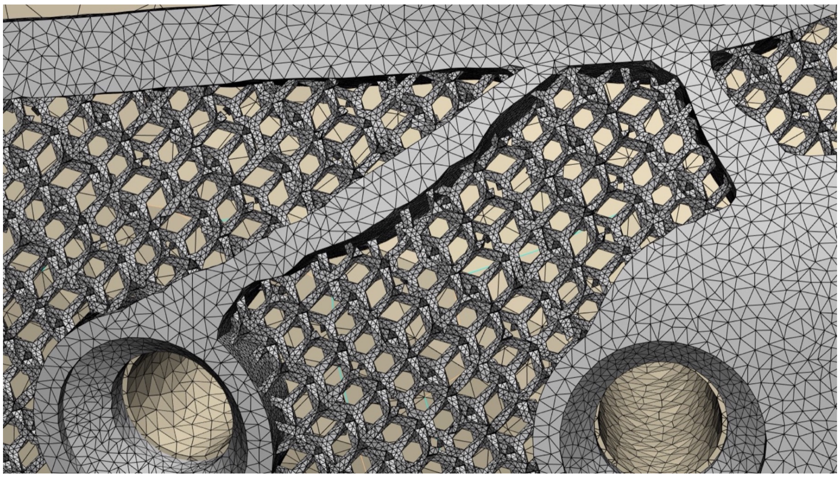

Figure 4.23. Anterior zoom-in of the mesh applied to the TO-implant-model.

4.7.5. Topology optimization

In this study, the Abaqus Topology Optimization Module was used to find an optimum implant shape. The most popular method to solve TO problems, referred to as “General topology optimization” in Abaqus adopts a density-based approach in which each element e inside the design space is assigned with design variable $\rho(x_e)$, which corresponds to the artificial material density of the element, where

$$0 \leq x \leq 1 \tag{4.7}$$

and x_e is the design variable vector. The solid isotropic material with penalization (SIMP) interpolation scheme defines the relationship between the density and the stiffness of an element, resulting in all elements being either hard or void elements. The TO starts with an initial model that contains the original design area, in this case the fully solid implant, and the prescribed loads and boundary conditions.

Table 4.4. Mesh properties of the components in the FE models.

Model	Component	Element type	# Nodes	# Elements
Healthy	Bone	C3D4	115.868	695.448
Solid-implant	Bone	C3D4	90.169	520.299
	Implant	C3D10[1]	44.554	204.034
Lattice-implant	Bone	C3D4	90.169	520.299
	Implant	C3D10	8.564.382	3.972.996
TO-implant	Bone	C3D4	90.169	520.299
	Implant	C3D10	6.926.718	3.280.634

1. C3D4 elements were used for topology optimization of the solid implant.

The optimization algorithm will then iteratively attempt to find a new material distribution by changing the element density and element stiffness. The purpose of the optimization procedure is to minimize or maximize a predefined objective function, while continuing to satisfy the predefined optimization constraints. In this study, the objective function was set to minimize the compliance of the entire model (i.e., to maximize structural stiffness). The structural compliance is defined as the sum of the strain energy (SE) of all elements in the model. For linear models, this can be expressed as

$$SE = \sum u^t k u, \tag{4.8}$$

where *u* and *k* represent the displacement vector and global stiffness matrix, respectively. The optimization constraint is set to constrain the final implant volume to 10% of the initial implant volume. This means that the final implant volume will be reduced by 90% from the initial solid volume. According to surgical advice, it would be beneficial for the healing process to have sufficient open space in the implant. Taking this and implant weight reduction into account, the solid implant volume fraction was estimated to be optimal around 10%. Lower volume fractions (e.g., around 5%) led to converging issues as it became computationally more expensive to calculate solutions for TO problems that involved low material volume fractions (Gupta et al., 2020). Since the global shape of the implant was defined earlier, no geometrical restrictions were applied to the optimization procedure.

Multiple load cases, in this case INC and RMB, can be defined in Abaqus within a single step. Not only does this give more realistic results than when the shapes of the implants obtained from separate analyses are combined afterwards, but it also significantly reduces the computational cost.

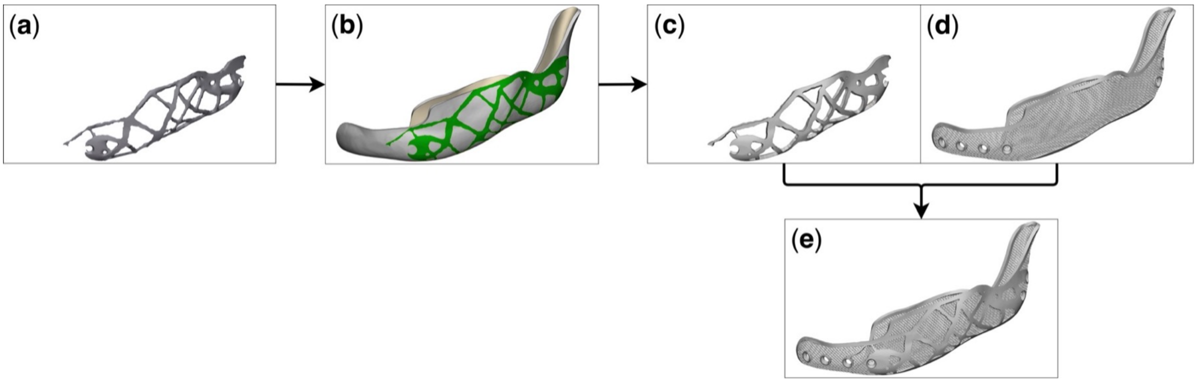

Figure 4.24. 3-Matic steps for creating the TO implant design, showing (**a**) the 'raw' TO structure, (**b**) the surface marked on the solid implant, (**c**) the extracted surface after offsetting, (**d**) the lattice implant, and (**e**) the final TO implant design after merging (**c**) and (**d**).

The sequence of steps used in 3-Matic to finalize the TO design is shown in Figure 4.24. After completion of the combined analysis, the optimized result from the last design cycle was saved as an

STL file and imported into 3-Matic (Figure 4.24-a). Here, the surface of the original geometry was first smoothed, and triangles were subsequently reduced in number and subdivided. Contours of the resulting shape were then marked on the surface of the solid implant by overlaying the two structures in a transparent mode (Figure 4.24-b). After applying a uniform offset to this surface with a distance corresponding to the implant thickness (Figure 4.24c), the structure was unified with the lattice implant (Figure 4.24-d). This way, the cage-shaped geometry and screw locations are preserved in the final TO design (Figure 4.24-e).

4.8. Experimental methods

4.8.1. Additive manufacturing

All lattice and TO implants investigated in this study were 3D printed from Ti-6Al-4V ELI grade 23 (as-built) using SLM (SLM Solutions®). The chemical composition, printing properties and tensile mechanical properties of the titanium specimen are listed in Table 4.5, Table 4.6, and Table 4.7, respectively. The surgical guide was 3D printed from “tough” PLA material using FDM.

Table 4.5. Chemical composition [mass fraction in %] of 3D printed Ti-6Al-4V obtained from SLM Solutions® (n.d.).

Condition	*Layer thickness / laser power (µm / W)*	*Particle size (µm)*	*Mass density (g/cm^3)*	*Roughness average Ra (µm)*	*Mean roughness depth Rz (µm)*
As-built	60 / 400	20 – 63	4.43	12 ± 1	71 ± 6

Table 4.6. Ti-6Al-4V printing properties obtained from SLM Solutions® (n.d.).

Condition	*Layer thickness / laser power (µm / W)*	*Particle size (µm)*	*Mass density (g/cm^3)*	*Roughness average Ra (µm)*	*Mean roughness depth Rz (µm)*
As-built	60 / 400	20 – 63	4.43	12 ± 1	71 ± 6

Table 4.7. Tensile mechanical properties of 3D printed Ti-6Al-4V obtained from SLM Solutions® (n.d.).

Offset tensile yield strength $R_{\rho 0,2}$ [MPa]	*Tensile strength R_m [MPa]*	*Elongation at break A [%]*	*Reduction of area Z [%]*	*Young’s modulus E [GPa]*
1189 ± 49 (H) 1196 ± 26 (V)	1351 ± 17 (H) 1330 ± 12 (V)	7 ± 1 (H) 9 ± 1 (V)	13 ± 2 (H) 26 ± 3 (V)	113 ± 7 (H) 120 ± 4 (V)

4.8.2. Design of the experiment setup

A testing setup denoted as ‘the three-point fixation’ setup was developed for this research to evaluate the performance of the reconstruction systems and validate the FE models. In order to create a specific clenching task, a distributed load is applied to both mandibular angles while fixing translations of both condyles and constraining a certain region on the dental arch perpendicular to the plane of occlusion. Only rotational movement of the condyles about the transverse horizontal axis is allowed. In this particular setup, the mandible can be placed in an upstraight anatomically correct position or in a reversed upside-down position, as shown in Figure 4.25-a. The latter is used more often because this position yields a more convenient way of applying the force. Loads on the dental arch are applied by a rigid bar or see-saw device that presses down onto the mandibular angles using a materials testing machine. Due to the frequent absence of dental support on the affected side, and preference of the patient to chew with the healthy side, a load distribution of 70% and 30% is commonly applied to the mandibular angles of the healthy and affected side, respectively (Gateno et al., 2013; Rendenbach et al., 2017; Schupp et al., 2007). This setup was designed such that it could be used on two instruments:

one for quasi-static testing (Lloyd Instruments LR5K) and the other for cyclic fatigue testing (INSTRON ElectroPulsTM E1000). An overview of the complete setup is shown in Figure 4.25-a. Several translational and rotational degrees of freedom for mandible positioning and fixation were implemented in the setup design. This way, tests can be performed on mandibles (or mandible models) with arbitrary dimensions, which will be particularly useful when cadaver studies will be performed in the future. The different parts that comprise this setup were machined from stainless steel (SS316), given its material strength and corrosion resistance. Fabrication of the parts from raw materials was performed in-house using conventional machining processes.

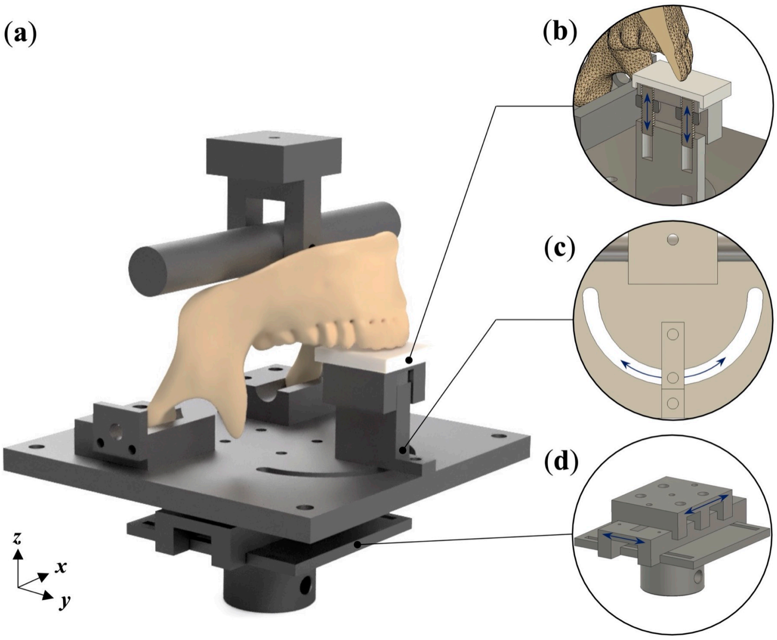

Figure 4.25. (**a**) Overview of the complete experimental setup, (**b**) axial movement of the tooth support structure along the *z*-axis, (**c**) rotation of the tooth support structure about the *z*-axis, (**d**) and axial movement of the linear bases along the *x*- and *y*-axes.

The setup assembly consists of 13 different parts excluding screws and nuts, as can be seen in the exploded view in Figure 4.26. Starting from the bottom, the setup is built upon a structure of sliding bases that carry out the function of an *xy*-table. Part 1 is fixed on the bottom table of the test instrument, i.e. the Lloyd machine in Figure 4.25, through a pinned connection. Part 2 and part 3 are placed consecutively on top of part 1 and can slide along the *y*-axis and *x*-axis, respectively (Figure 4.25-d). The main table (part 4) is mounted to part 3. Depending on the desired loading situation, the table can be positioned differently under the loading bar through smooth sliding movements of parts 2 and 3 in the *x*-*y*-plane. Two blocks (parts 5 and 6) are fixed to the table and contain cylindrical grooves that serve as support for the mandibular condyles. This type of support restrains translation of the condyles in the vertical *z* direction and allows for rotations about the transverse horizontal (*x*) axis only. Two large screws are inserted through parts 7 and 8 so that the screw ends prevent outward translation of the right and left condyle in the respective positive and negative *x*-axis. Part 9 is the base component for the teeth support and can be rotated about its own axis, as well as along the oval-shaped slit that is designed in the main table such that it follows the average contour of the dental arch (Figure 4.25-c). Consequently, different loading scenarios can be tested by supporting different groups of teeth. The last degree of freedom of movement is enabled by part 10, which is a small plate that rests upon two nuts that are fixed to small segments of screw thread. Depending on the desired mandibular angle, these screw thread segments can simultaneously be turned up- or downwards to elevate or lower the support platform, respectively (Figure 4.25-b). A plastic platform (part 11) that is 3D printed through FDM with regular PLA material can be placed on top of part 10. Finally, a loading bar (part 12) is via another pinned connection attached to part 13, which is in turn fixed to the load cell of the test instrument. Part 13 enables a hinging effect that allows the loading bar to be used as a seesaw to compensate for differences in height of the mandibular rami.

The assembly that was used for the cyclic testing on the Instron device is similar to the one shown in Figures 4.25 and 4.26. However, the Instron machine already has a T-slot table build in which provides freedom of movement along the *y*-axis. Therefore, a separate plate has been designed that replaces parts 2 and 3 in Figure 4.26 and can be directly fixed onto the T-slot table

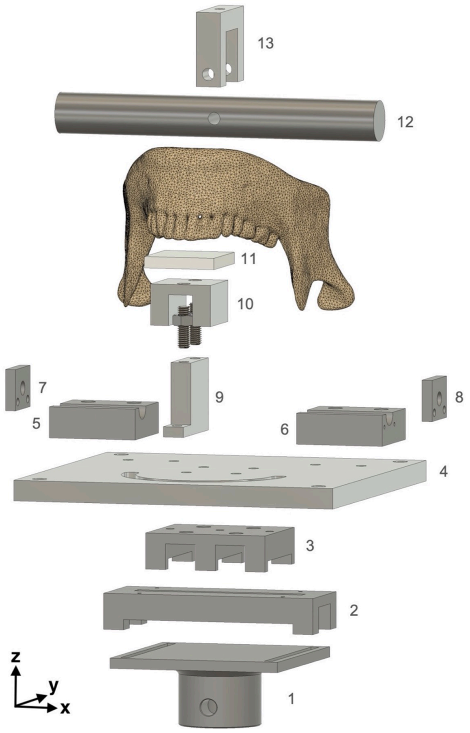

Figure 4.26. Exploded view of all components in the experimental setup.

In the FE simulations, the mandible model was positioned according to cephalometric standards (Pinheiro and Alves, 2015). To establish accurate comparison between numerical and experimental results, the mandibles were positioned in the experimental setup so that the mandibular angle was similar to that in the FE models. Therefore, the mandibles were oriented with their inferior border at around an angle of 26° to the horizontal plane (Figure 4.27), which also corresponded to the angle used in the experiments of Gateno et al. (2013).

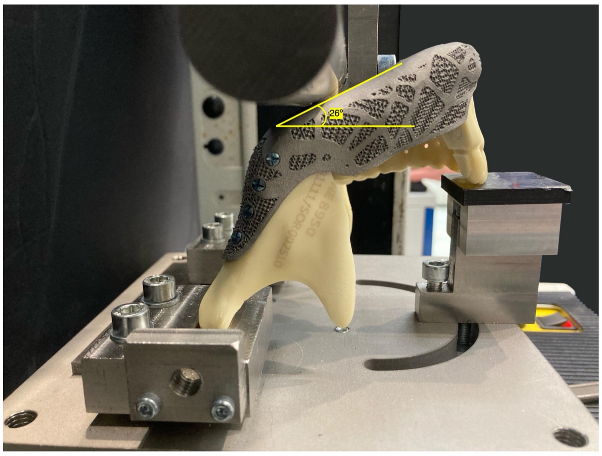

Figure 4.27. Position of the mandible inside the experimental testing setup (quasi-static), indicating the 26° angle between the inferior border of the mandible and horizontal plane.

4.8.3. Sample preparation procedure

All implanted samples were prepared, following the procedure described below. The 3D printed surgical guide was clicked on the mandible (Figure 4.28-a). The 8 screw holes were predrilled using a 1.8-mm drill bit (Figure 4.28-b). The resection area was cut out using an oscillating saw (Figure 4.28-c). The two remaining parts were taken out of the surgical guide and fixed inside the implant with the screws using a custom screwdriver (DePuy Synthes®) (Figure 4.28-e).

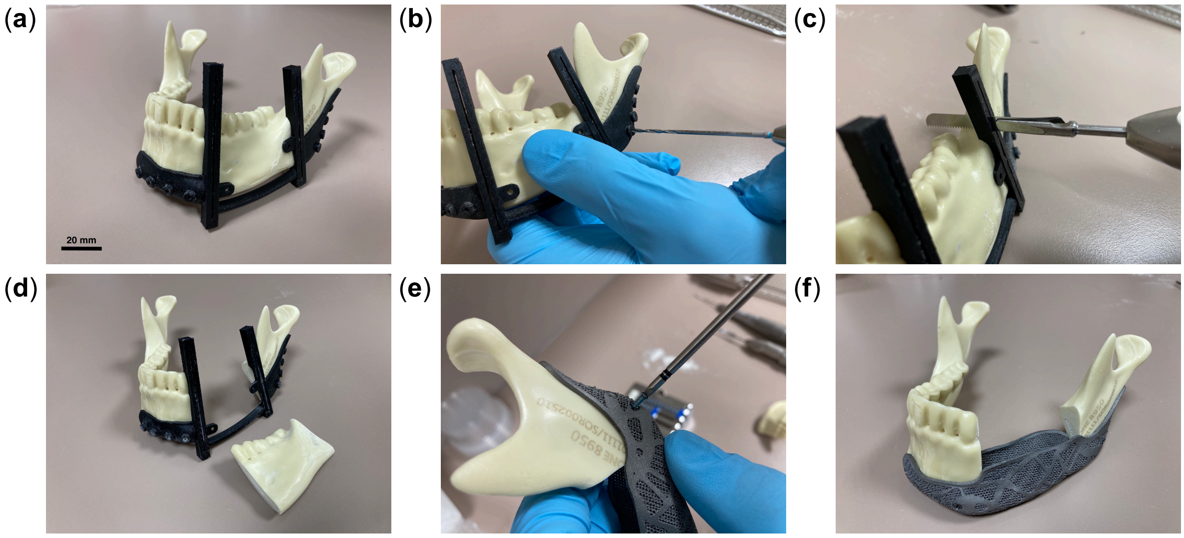

Figure 4.28. Sample preparation procedure, showing (**a**) the surgical guide secured to the mandible, (**b**) predrilling of the screw holes using a 1.8-mm drill bit, (**c**) resection of the 'defect' area using an oscillating saw, (**d**) removal of the resected segment, (**e**) screw fixation of the implant (in this example TO implant) to the mandible, and (**f**) the final implanted sample.

4.8.4. Quasi-static testing protocol

Samples were subjected to continuous compression at a loading rate of 1 mm/min until failure of the sample. Failure of the sample was defined as fracture of the plate or mandible, failure at screw-substrate interface (e.g., screw pullout or loosening), or vertical displacement above 20 mm. A pre-load was set at 10 N (Koper et al., 2021).

As indicated earlier, loads on the dental arch were applied by the rigid bar that pressed down onto the mandibular angles. Initially, 70% of the load was allocated to the intact right-hand side of the mandible, while the remaining 30% was allocated to the reconstructed left-hand side for both INC and RMB conditions (Figure 4.29-a). Since implant failure did not occur using the current loading setup, measurements were also performed in a 50/50% distributed loading configuration for both loading conditions (Figure 4.29-b). This way, both sides of the mandible were loaded equally, putting more stress on the implanted side, as compared to the 70/30% loading configuration.

Table 4.8. Number of mandibles used for each loading condition during quasi-static testing.

Loading configuration		Healthy-model	LA-implant-model	TO-implant-model
INC	50/50 %	2	3	3
	70/30 %	2	3	3
RMB	50/50 %	1	3	3
	70/30 %	2	3	3

INC = incision clenching, RMB = right molar biting.

Due to the limited number of samples, 3 samples with lattice implant and 3 samples with TO implant, and 2 non-implanted control samples could be tested in each group (Table 4.8). Only one control sam-

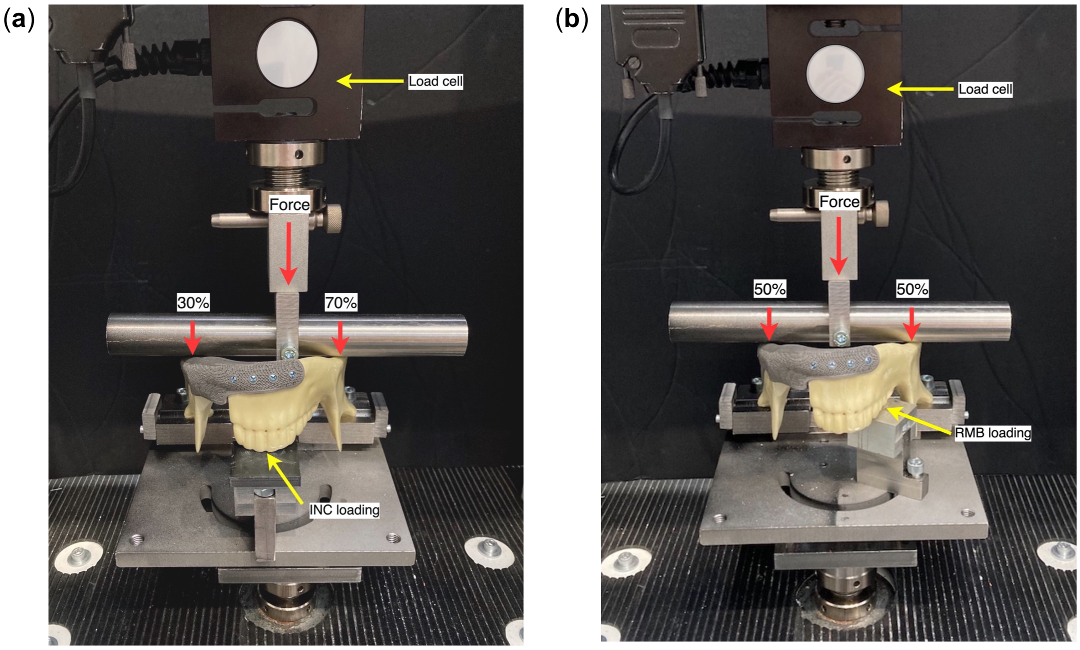

Figure 4.29. Quasi-static testing setup including implanted specimen. (**a**) RMB loading with a 50/50% force distribution between the left and right side. (**b**) INC loading with a 70/30% force distribution between the intact and implanted side. INC loading in a 50/50% force distribution and RMB loading in a 70/30% force distribution were also tested but are not shown in this figure.

ple was used for RMB 50/50% loading condition because of test failure with the other control sample.

For each sample, the failure or ultimate load (N) of the construct, ultimate displacement (mm), and the location of failure were recorded. A one sample t-test was used to evaluate differences between the three groups, where $P < 0.01$ was set as the threshold level for statistical significance. The stiffness (N/mm) was determined from the slope of a best-fit approximation of the linear portion of the load-displacement curve (Figure 4.30). The maximum slope was determined in MATLAB by using an algorithm that iteratively calculates the gradient within a predefined data window size.

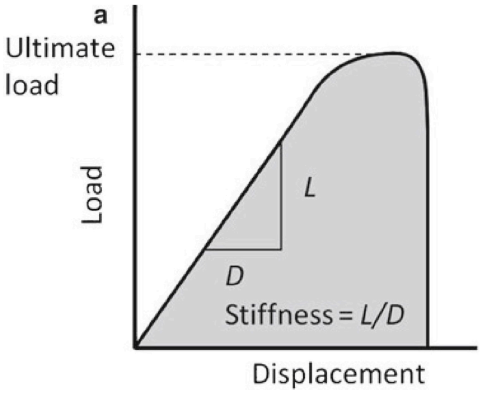

Figure 4.30. Example of a load-displacement curve. Stiffness is defined as the slope in the linear region of the curve. Image extracted from Goodyear and Aspden (2012).

4.8.5. DIC measurements

Digital 3D Image Correlation System Q-400 by Dantec Dynamics was used to measure surface strains on the samples during quasi-static tests. In total, three measurements were performed: one for the healthy-model, another one for the LA-implant-model, and the third one for the TO-implant-model. The posterior segment on the implanted side of the mandible was selected as the area of interest as it included the primary location of sample failure. Speckle patterns were applied to the region of interest by first spraying a thin layer of white paint on the surface, followed by the application black contrasting paint using an air spray gun (Figure 4.31). The entire experimental setup was rotated 90º so that the region of interest was directly facing the cameras (Figure 4.32). Two digital cameras and two light-emitting diode (LED) panels were used to create the images and illuminate the samples, respectively. Both the cameras and LEDs were placed at around 0.8 m distance from the sample. Each sample was subjected to quasi-static loading until failure of the sample. A calibration target containing a defined grid pattern was used to calibrate the system parameters. Image processing and strain calculations were performed using the Istra4D x64 4.6.5 software by Dantec Dynamics. To achieve high strain accuracy and a relatively low absolute strain error, the facet size and grid spacing were set at 33x33 pixels and 11 pixels, respectively. The imaging frequency was set at 1 frame/sec.

Figure 4.31. (**a**) Speckle pattern applied to the three samples using contrasting spray paints. (**b**) Close-up image of lattice implant with applied speckle pattern.

The main purpose of performing the DIC measurements was to compare strain fields with those predicted by FEA. Extracting values from a single point would introduce an error when points are not chosen at the exact corresponding locations. This effect will be enhanced in the presence of very local strain concentrations that would otherwise be regarded as outliers. Such errors can be minimized by averaging the strain values over a larger surface are. Hence, two enclosed polygonal regions, denoted as Polygon-1 and Polygon-2, were created on the anterior and posterior condylar neck region of the mandibular bone, corresponding to the areas of largest maximum and minimum principal strain, respectively. The mean strain value for each of these two areas was extracted and plotted against the applied force. Similarly, the two corresponding areas, denoted as Area-1 and Area-2, were identified in the FE model, and the average nodal strain values within both areas were plotted against the reaction force on the loading bar. Note that only the linear elastic portion of the applied force could be used for comparison of DIC data with the FE model as plasticity is not accounted for in the FE analysis. Validation of the FE model through DIC was done using the non-implanted mandible. Besides, differences between the three groups (healthy-model, LA-implant-model and TO-implant-model) were identified by comparison of true effective (Von Mises) strain fields at the time of failure, which indicated how much the material changes in shape and volume under the applied stress.

4.8.6. Cyclic testing protocol

Cyclic testing or fatigue testing is a form of mechanical testing in which the resistance of materials to damage is measured under a repeated application of load. While the structure is subjected to repetitive loads, the stiffness and strength of the material reduce progressively and eventually, after a certain number of cycles, the material will fail and break. The failure mechanism of structures subjected to frequently repeated stress is associated with the propagation of cracks through the material. Fatigue loads initiate crack growth which will promote premature failure in the specimen, often at loads much lower than those reached during a static load-to-failure test. Even though static tests usually perform very well in detecting weak points within implant designs, implants generally do not fail as a consequence of a single loading event but rather under fatigue loading conditions. Therefore, fatigue tests better

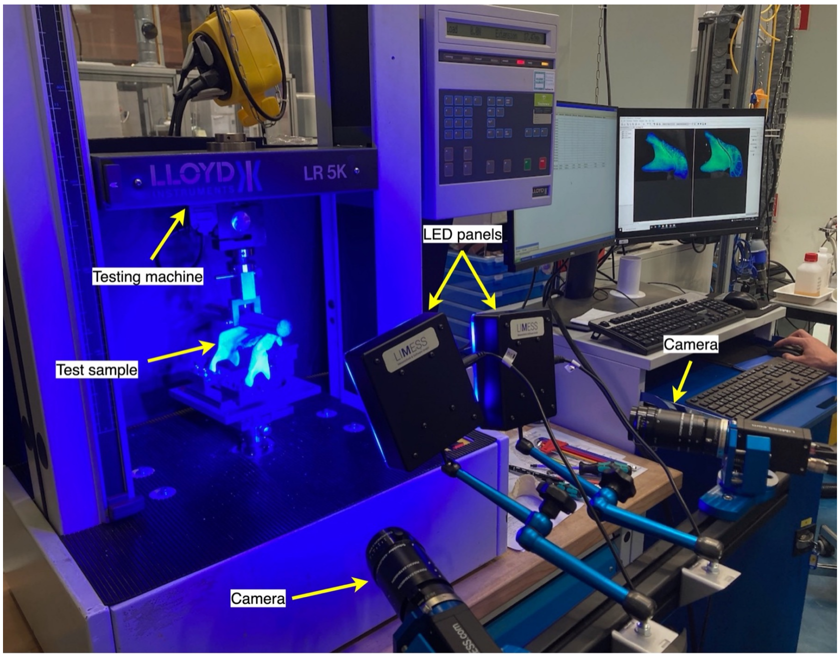

Figure 4.32. Experimental arrangement for measuring strain fields on the specimens using DIC.

reflect the loads applied to the human body during daily life activities, such as in this case the repetitive loads applied to the mandible during chewing, making them pivotal in determining the longevity of the implant designs.

Since fatigue failure in materials often occurs well below the static strength limits, it is important to determine the maximum load that the implanted reconstruction system can withstand for a specified number of cycles. A common method to determine the fatigue resistance of materials is by creating a fatigue life (S-N) curve, in which the maximum fatigue stress amplitude (S) is plotted against the number of cycles-to-failure (N). An example of such an S-N curve is shown in Figure 4.33.

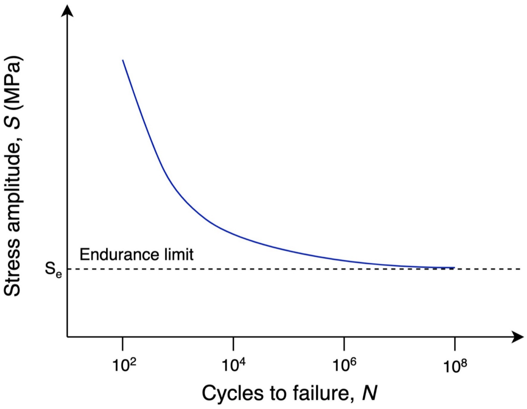

Figure 4.33. Example of a typical fatigue life (S-N) curve. The number of cycles to failure are plotted on a logarithmic scale, whereas the stress is plotted on either a linear or logarithmic scale. Failure by fatigue does not occur below the limiting stress (S_e), also known as the endurance limit or fatigue limit.

An image of the cyclic testing setup is shown in Figure 4.34. First, the fatigue performance of the implant was tested at physiological conditions by cycling the stress between a constant minimum and maximum compressive stress amplitude (Figure 4.35-a). This method will be denoted as ‘constant-cyclic-method’. The minimum load (preload) was set at 30 N. The maximum load was, like the biting force used in the computational models, set at 340 N which corresponds to the ‘worst case’ maximum biting force of patients that have been subjected to reconstruction surgery. The loading rate was set at

3 Hz, which is fast enough to imitate physiological biting speed, but not too fast to give the specimen enough time to recover during unloading and prevent irregular sine profiles. Survival of the implanted system at this post-surgical 'worst case' load throughout the maximum number of 250.000 cycles guarantees the long-term safety of the implant. In other words, implant fatigue will in that case not occur under the expected physiological circumstances. In total, 4 samples were tested using this method, of which 2 samples contained the lattice implant and 2 samples contained the TO implant. An INC 50/50% loading configuration was used to provide the most stable setup while transferring the highest load through the implant.

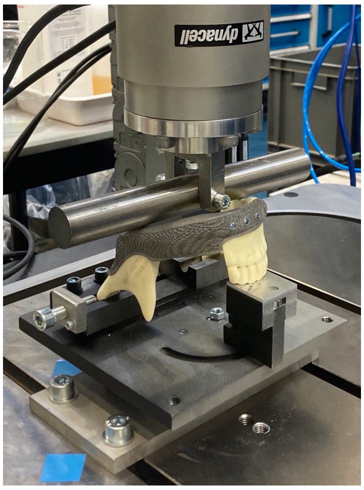

Figure 4.34. Cyclic testing setup with implanted specimen included.

As yielding and failure of the implanted mandible occurred at loads much larger than 340 N as measured by the quasi-static tests, the samples would not be expected to fail during cyclic tests under this maximum load. To detect potential implant failure or screw loosening because of fatigue, and to determine at which load this fatigue failure would occur, a second cyclic testing procedure denoted as 'increment-cyclic-method' was used. In this loading procedure, the maximum stress amplitude increased incrementally (3 N per cycle) from the initial load of 340 N until failure of the specimen or until the maximum load of 2500 N (Figure 4.35-b). As with constant-cyclic-method, the loading frequency was set at 3 Hz and a total of 4 samples were tested, of which 2 samples contained the lattice implant and 2 samples contained the TO implant, using an INC 50/50% loading configuration. For both cyclic methods, the number of cycles to failure and failure load are reported. Plots of the minimum and maximum displacement of the loading bar versus the number of cycles are attached in Appendix C.

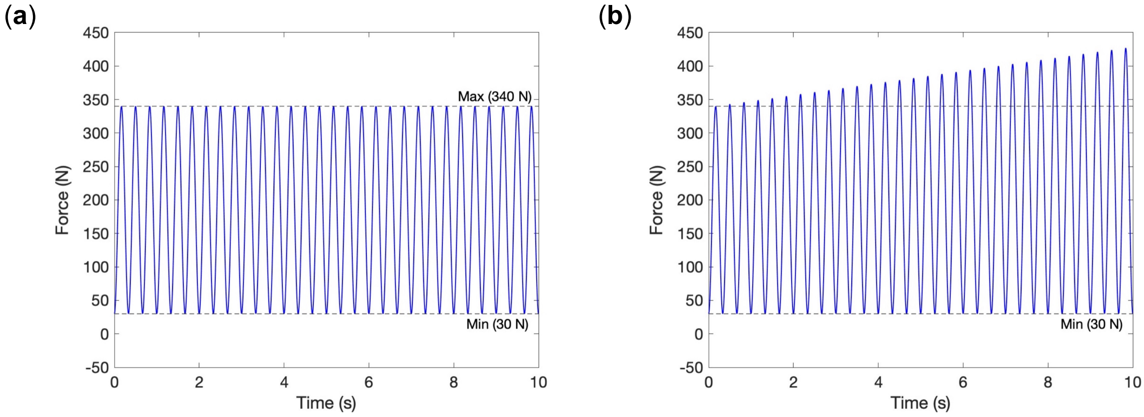

Figure 4.35. Cyclic loading sine waves plotted for the first 10 seconds for (**a**) constant-cyclic-method and (**b**) increment-cyclic-method.

5

Results

5.1. FEA results

5.1.1. Validation of FEA

The stiffness of the mandible in the FE model was compared with the stiffness obtained from the quasi-static test that was performed in combination with DIC. Good correspondence in stiffness was found for the mandible analogue with a Young's modulus of 0.41 GPa. Stiffness values of 274.9 N/mm and 278.5 N/mm were obtained from best-fit approximations of the linear portion of the force-displacement curves of experiment (EXP) and the FE model (FEA), respectively (Figure 5.1).

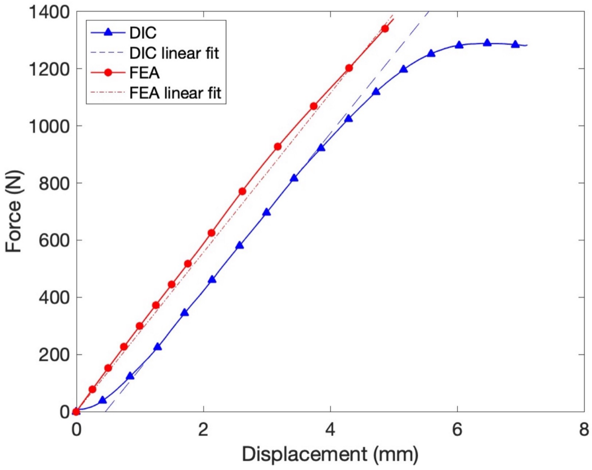

Figure 5.1. Force-displacement curves of the non-implanted control mandible obtained by FEA and experiment (EXP). Dotted and dashed lines represent best-fit approximations of the linear portion of the curves.

Figure 5.2-a shows the von Mises stress distribution on the intact mandible at a load of 804 N. The highest stress values can be found at the posterior (12 MPa left and 16 MPa right) and anterior (14 MPa left and 16 MPa right) sides of the condylar neck, and along the external oblique line (8 MPa left and 9 MPa right). The vector displacement plot of Figure 5.2-b shows predominant movement of the mandibular angles in the superior-anterior direction, with a maximum displacement of 3.1 mm. This agrees well with the directions of deformation observed in the samples during experimental testing (Figure 5.3).

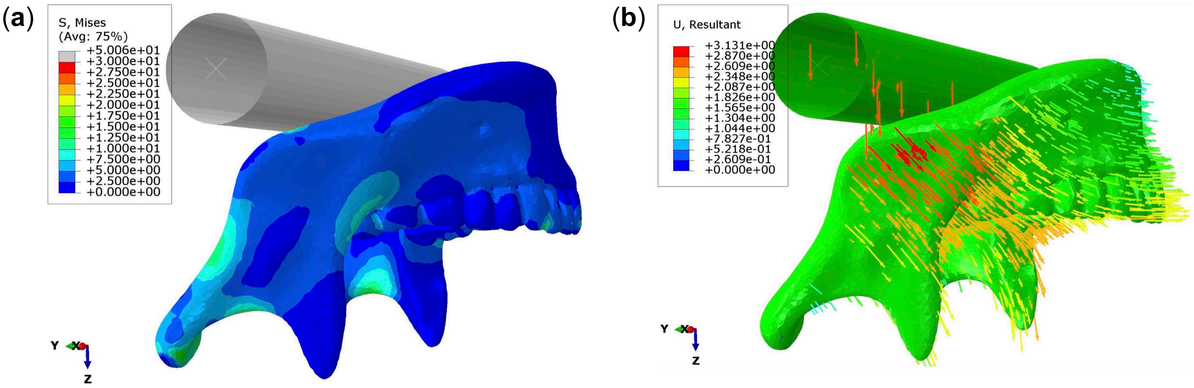

Figure 5.2. (**a**) Von Mises stress (MPa) contour on the non-implanted mandible under experimental conditions, and (**b**) symbol plot of the resultant displacement vector (mm) on the deformed mandible. Deformations in both figures correspond with a bar loading of 804 N.

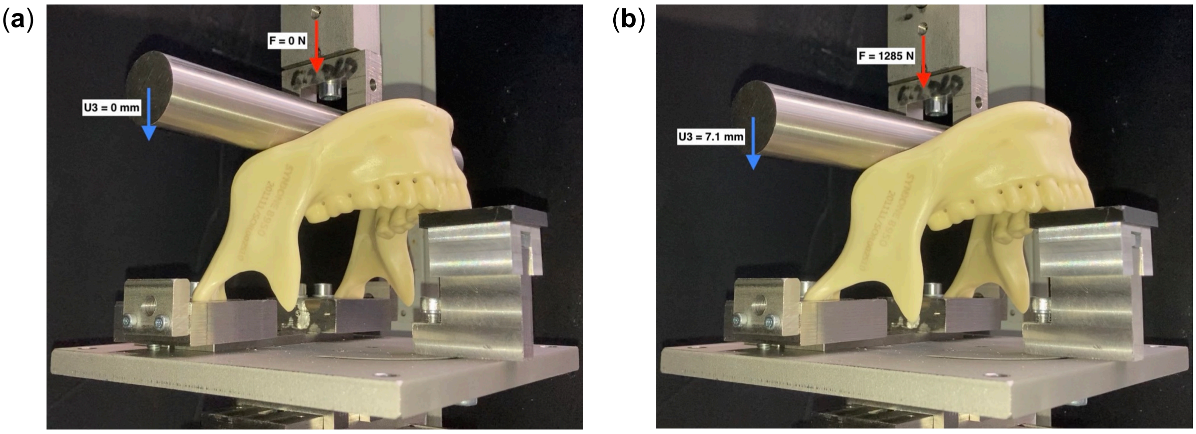

Figure 5.3. Intact mandible in the quasi-static testing setup. (**a**) Prior to loading (0 N), and (**b**) just before fracture (1285 N). The applied force (F) and vertical displacement (U3) of the loading bar are indicated by the red and blue arrows, respectively.

5.1.2. FEA of stress distribution under physiological conditions

In the case of the healthy-model, the combined muscle forces create resultant biting forces of 570.90 N and 600.40 N for INC and RMB, respectively. Deformation patterns are compared with the deformations obtained by Korioth and Hannam (1994) in Figure 5.4. Looking at the INC condition, the most deformation of the mandible occurs around the dental arch. The overall deformation pattern is very similar to that obtained by Korioth, with the molars moving up- and slightly inward and the front teeth moving forward. Looking at the RMB condition, the results match well with those from Korioth, showing a counterclockwise torsional movement with a maximum deformation located at the left gonial angle.

Distributions of Von Mises stress on the healthy mandible subjected to INC and RMB loading are shown in Figure 5.5-a and 5.5-b, respectively. Reaction forces correspond to those obtained by Pinheiro and Alves (2015), as mentioned earlier in Section 4.7.2. A stress contour plot of the healthy mandible was only provided for the INC condition in Pinheiro and Alves (2015). Like their results for this condition, high stresses can be observed below the condylar process in the mandibular notch (37 MPa), along the external oblique line (29 MPa), and at the posterior aspect of the ramus (33 MPa). In accordance with the findings of Pinheiro and Alves (2015) in the case of RMB, high stresses were found on the posterior aspect of the contralateral ramus, when compared with the working (right) side, as well as along the external oblique lines on both sides.

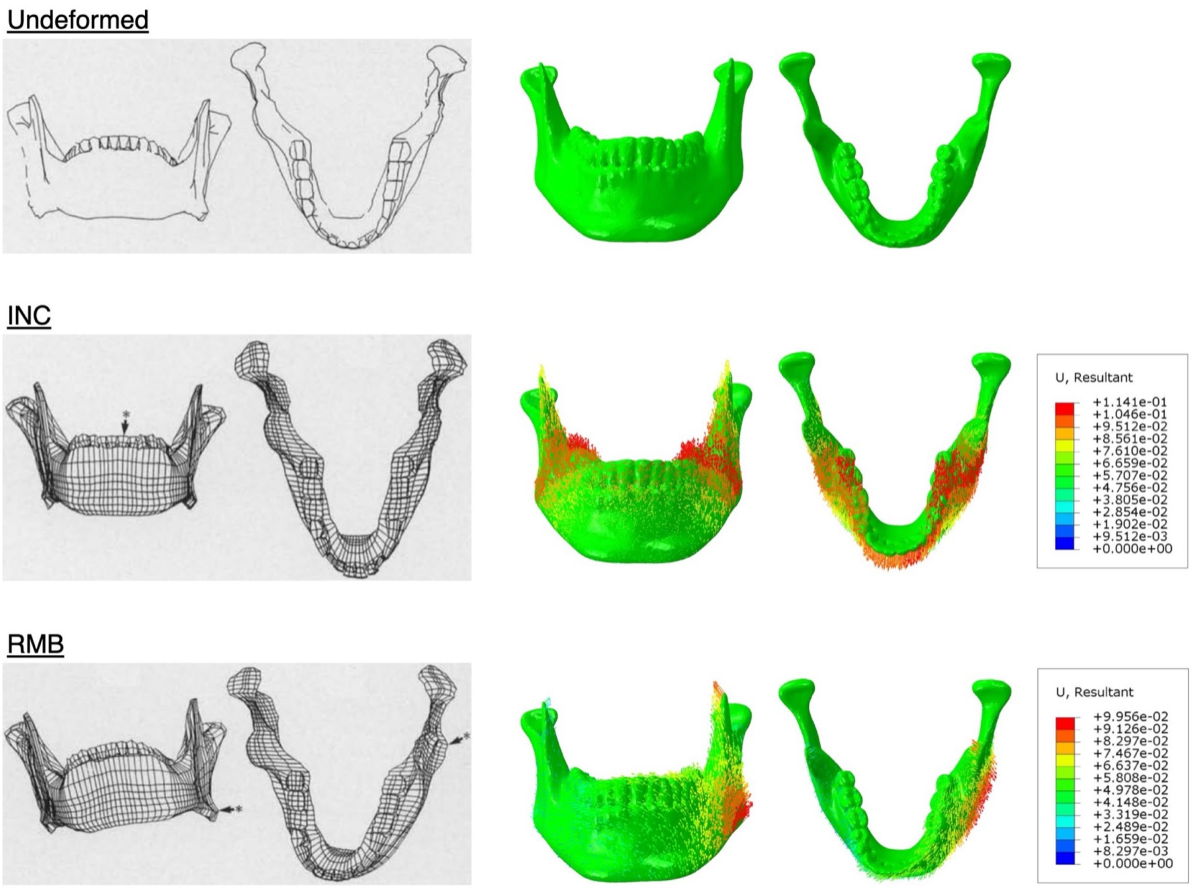

Figure 5.4. Comparison of resultant deformation U (mm) with Korioth and Hannam (1994) for the healthy mandible. Figures on the left side show front and top views of the mandible from Korioth at undeformed state (top), under INC conditions (middle), and under RMB conditions (bottom). Corresponding figures from this study are shown on the right side. Maximum deformations are magnified 26 times and 15 times for INC and RMB, respectively, in the Korioth models. Maximum deformations are magnified 50 times for both INC and RMB conditions in this study. Arrows in the vector plots represent the total displacement of each node. The color and length of the arrow indicate the magnitude and direction of the displacement, respectively.

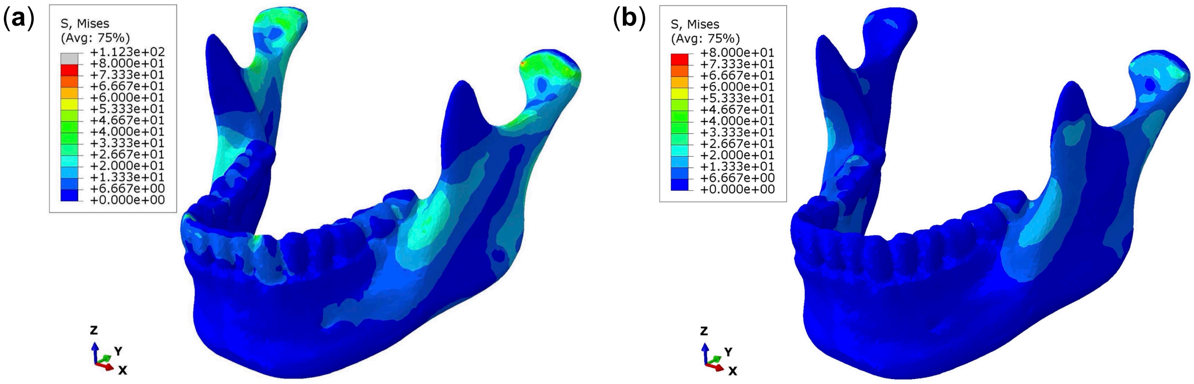

Figure 5.5. Distribution of Von Mises stress (MPa) on the healthy-model under (**a**) INC and (**b**) RMB conditions.

The Von Mises stress distribution plot obtained after topology optimization of the solid implant is shown in Figure 5.6. The elements of the implant that were assigned with zero density are excluded from the contour plot. The convergence plot of the analysis is shown in Figure 5.7. Maximum stress values for the implant (78 MPa) and bone (42 MPa) are well below the respective yield strengths of both materials.

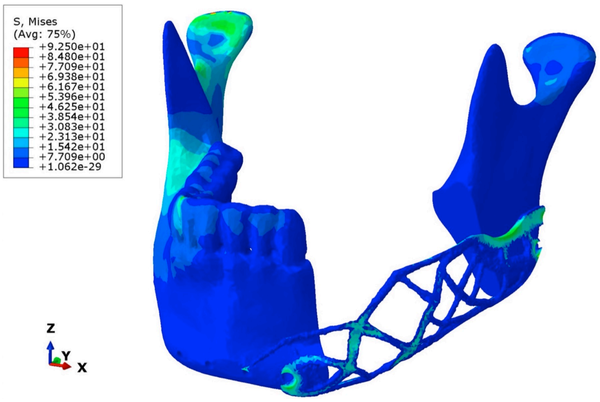

Figure 5.6. Von Mises stress (MPa) distribution after topology optimization of the solid implant.

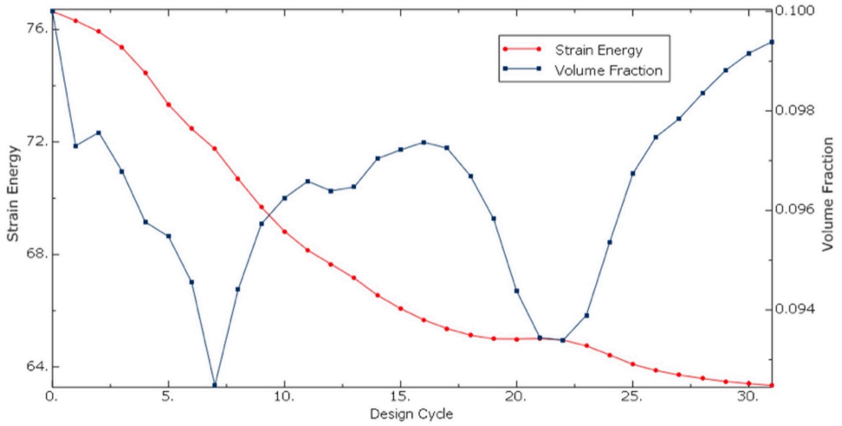

Figure 5.7. Convergence plot of the TO analysis. The TO analysis converged towards an optimum solution after 31 design cycles. The analysis using C3D4 elements for the implant resulted in a simulation time less than 18 hours, compared to 38 hours using C3D10 elements. Convergence plots and final geometries were nearly identical for both element types.

Figure 5.8 shows the distributions of von Mises stresses in the solid-implant-model, LA-implant-model, and TO-implant-model under INC and RMB conditions. For all three models, stresses on the mandibular bone are mainly located on the anterior and posterior condylar neck, and external oblique line of the contralateral (non-implanted) side during INC, and on the condylar neck of the lateral (implanted) side during RMB. Note that for both INC and RMB the stresses around the contralateral condyle are very similar (around 40 MPa), whereas the stresses on lateral condyle are lower in the solid-implant-model (15 MPa) compared to the TO-implanted-model (23 MPa), which in turn is lower compared to the lattice-implanted-model (55 MPa).

Elevated stress concentrations in the bone are also notable in and around the first and second posterior screw holes closest to the resection margin, with a maximum value of 36 MPa observed in the TO-implant-model. The stress values in the posterior aspect of the mandible are in all models well below the mean compressive yield strengths of cortical mandibular bone, which have been reported to be 200 MPa, 110 MPa and 100 MPa in the longitudinal, tangential, and radial directions, respectively (Van Eijden, 2000).

Von Mises stresses inside the implant are higher for the RMB condition than for the INC condition in all three implanted models. Some elevated stresses can be seen around the anterior screw holes, but the highest stress values are concentrated around the first posterior screw hole near the resection, and, to a lesser extent, along the curved implant edge above that screw. The area of the mandibular angle, and especially around the screws nearest to the proximal resection margin, is known to represent a weak point. For many reconstruction plates investigated in the literature fracture occurs between the two screw holes closest to the proximal resection margin (Gutwald et al., 2017; Yi et al., 1999; Trainotti

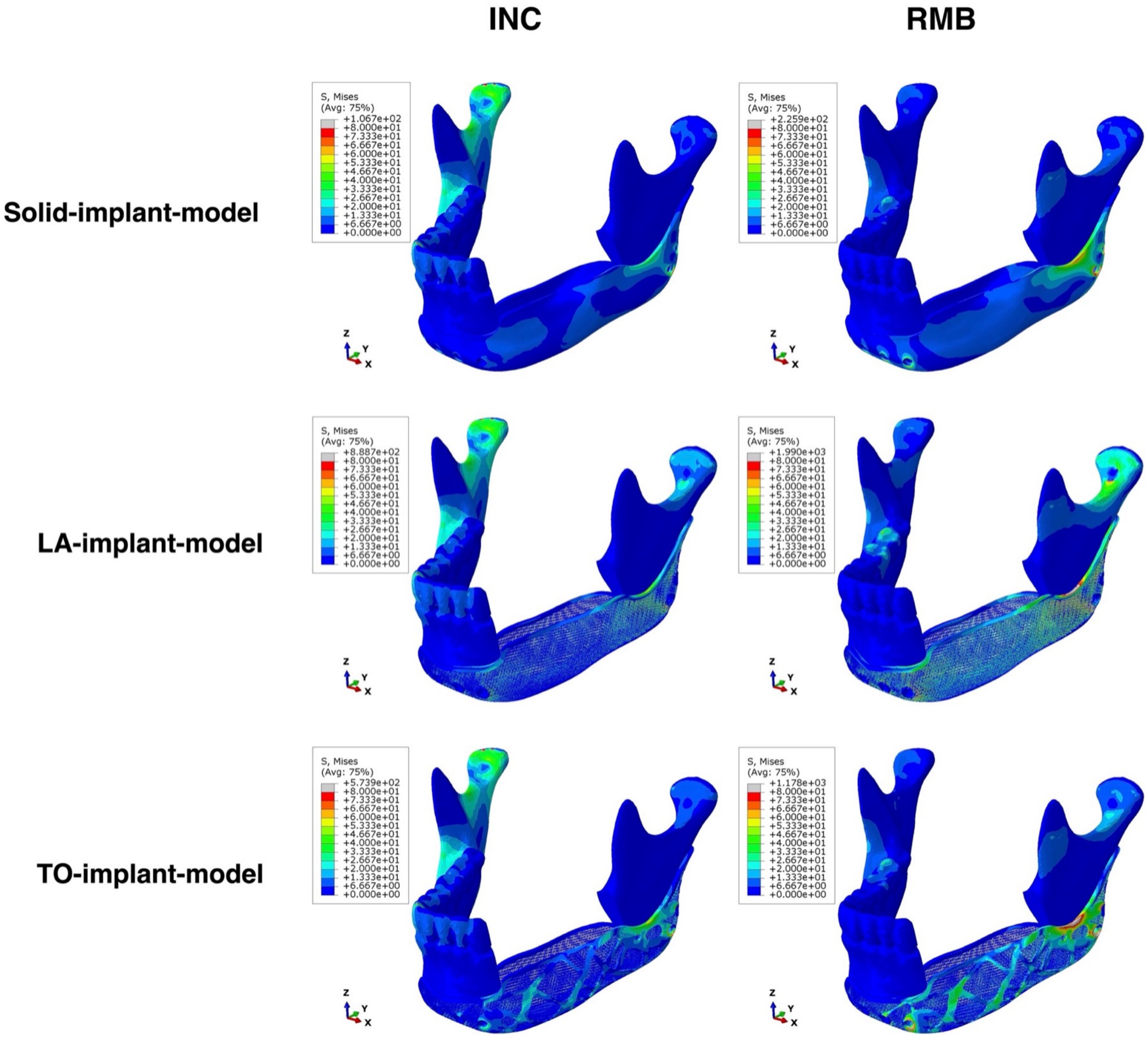

Figure 5.8. Distribution of Von Mises stress (MPa) on the three implanted models under INC and RMB conditions.

et al., 2014; Schupp et al., 2007). Figure 5.9 shows von Mises stress distributions on the most critical region of the three implant designs under RMB conditions. The figures indicate that except for some high stress values locally concentrated in the strut junctions, stress values stay well below the yielding safety limit of 400 MPa, which is the yield strength of Ti-6Al-4V (800 MPa) multiplied by a safety factor of 0.5 (C.-H. Li et al., 2020). The high stress values located in the strut corners are most likely the result of singularity calculation errors, as discussed in Section 4.7.4.

5.2. Experimental results

The weights of the lattice and TO implants after 3D printing were 15.8 g and 18.4 g, respectively. The weight of the removed mandible segment excluding the teeth was estimated to be around 20 g, based on CT density values of a real mandible with similar resection margins. The weight of the implants corresponds well with that of the original bone segment, and allows for additional weight from the dental prosthesis, which in the case of clinical application might have been placed at a later stage. The weights of the implants developed in this study are considerably lower compared to the implants used in case series reported in literature, which weighted from 55 to 95 g for a total of 7 implants, with an average weight of 60 g (Mounir et al., 2020). No other clinical studies that have reported the weight of their implant were found.

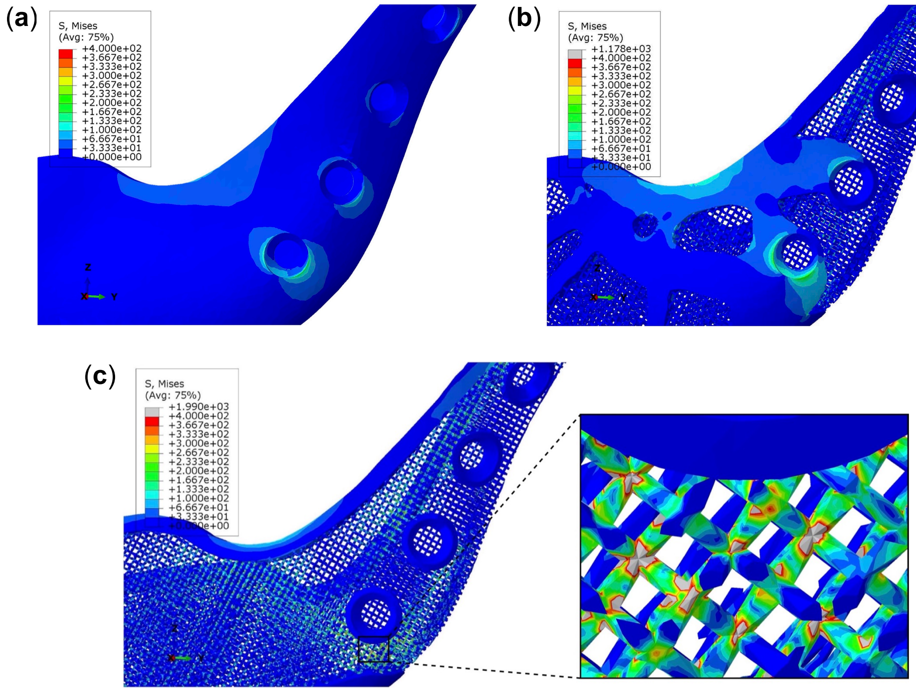

Figure 5.9. Distribution of Von Mises stress (MPa) across the lateral mandibular angle region of the (**a**) solid implant, (**b**) TO implant, and (**c**) lattice implant under RMB conditions.

No problems were encountered during preparation of the samples. In all samples, an excellent fit was obtained between the implant and the remaining mandibular segments, and a tight screw fixation was established after predrilling of the samples using the surgical guide.

5.2.1. Quasi-static mechanical behavior

Static biomechanical testing led to successful results with no implant failure or failures at the screw-substrate interface for all samples. Force-displacement graphs of the tested implanted and non-implanted mandibles under the four different loading scenarios are shown in Figure 5.10. The healthy (control) mandible, mandible with lattice implant, and mandible with TO implant are denoted as HC, LA, and TO, respectively. The location of fracture for all the samples in each group is indicated by the image at the bottom right. Fracturing occurred in the condylar neck region in all cases, either on the implanted or non-implanted side, depending on the loading condition. In all cases, fracturing occurred at loads far above the maximum physiological biting force of healthy individuals. This ensures a substantial safety factor with respect to the maximal loads that the reconstructed system can bear in the case of clinical application.

Table 5.1. Quasi-static testing results.

Loading condition	Group	Mean stiffness (N/mm)	Mean ultimate load (N)	Mean ultimate displacement (mm)
INC 50/50 %	HC	273.6 ± 1.9	1324.5 ± 52.0	6.7 ± 0.3
	LA	358.6 ± 18.6	1492.0 ± 57.2	6.0 ± 1.1
	TO	338.2 ± 28.8	1365.1 ± 41.0	6.1 ± 0.7
INC 70/30 %	HC	295.3 ± 5.3	1253.6 ± 76.4	5.8 ± 0.5
	LA	311.5 ± 8.3	1200.9 ± 54.0	5.3 ± 0.3
	TO	323.3 ± 21.9	1271.5 ± 112.0	4.9 ± 0.4
RMB 70/30 %	HC	480.4 ± 14.2	2364.0 ± 78.9	6.6 ± 0.0
	LA	578.5 ± 63.1	2440.2 ± 181.7	5.8 ± 0.3
	TO	570.0 ± 53.5	2372.6 ± 73.5	5.9 ± 0.2

* Data are presented as mean ± SD.

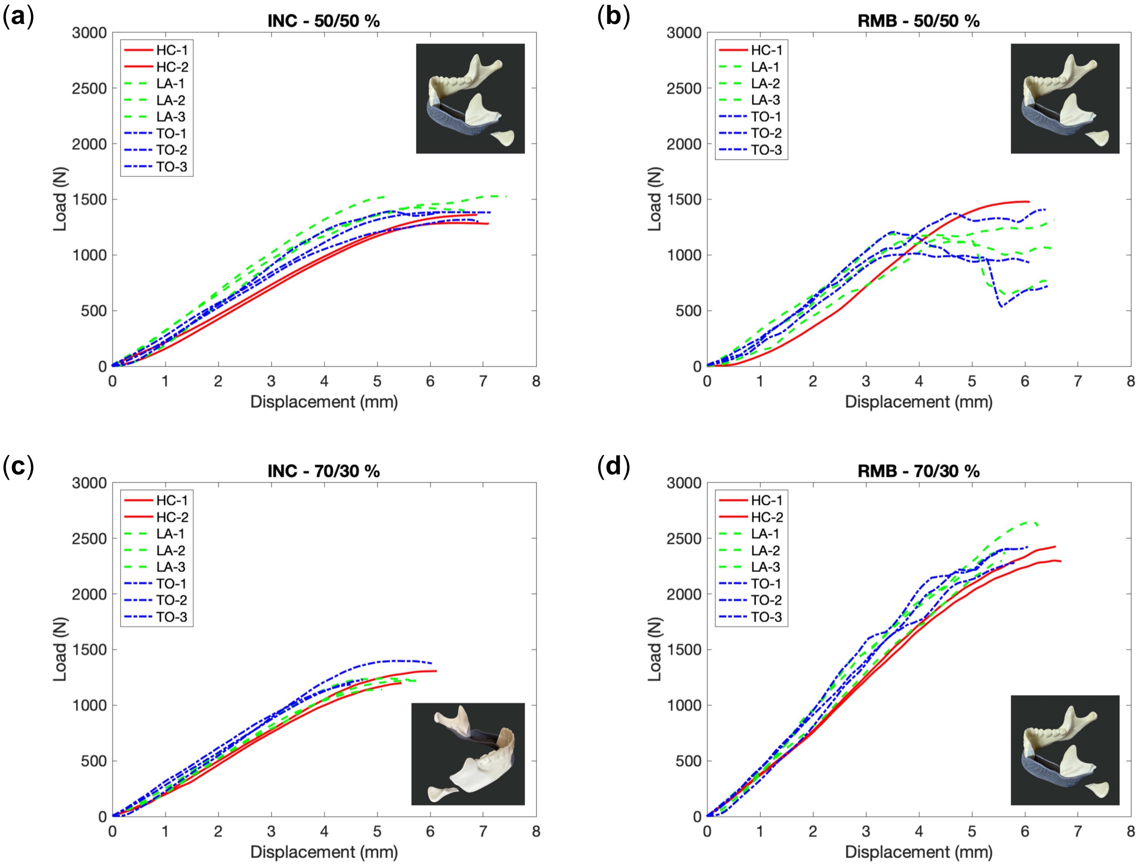

Figure 5.10. Load-displacement curves obtained with quasi-static testing for (**a**) INC biting in a 50/50% loading configuration, (**b**) RMB biting in a 50/50% loading configuration, (**c**) INC biting in a 70/30% loading configuration, (**d**) RMB biting in a 70/30% loading configuration. The small images at the top and bottom right indicate the location of fracture in each group.

Mechanical properties could not be accurately determined for the samples in the RMB 50/50% loading condition, since torsional movements at the balancing (non-biting) side created an unstable loading configuration, until eventually (>1000 N) the mandible rotated out of the setup fixtures. As a result of this, the test had to be terminated before fracture could occur for most of the implanted samples in this group (4 out of 6).

For the other 3 loading conditions, the stiffness, ultimate load, and ultimate displacement of the samples are presented by grouped scatter plots in Figure 5.11-a, 5.11-b and 5.11-c, respectively. Mean values are listed for each group in Table 5.1. The control group and two implant designs showed comparable mechanical stiffness, ultimate loads, and ultimate displacements. No significant differences ($P < 0.01$) were found between the groups in each loading scenario.

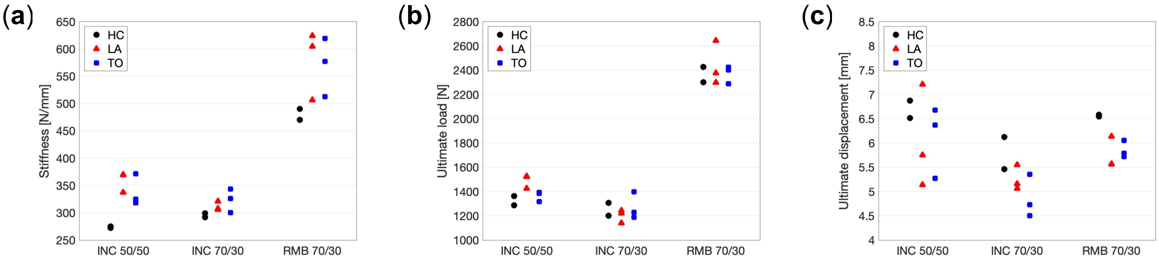

Figure 5.11. Grouped scatter plots of the (**a**) stiffness, (**b**) ultimate load and (**c**) ultimate displacement of the constructs obtained during quasi-static testing.

5.2.2. Strain distribution

The maximal and minimal principal strain distributions predicted with FEA and measured with DIC on the intact mandible are shown in Figure 5.12. Note that within the elastic region the logarithmic strain (LE) and true strains should yield essentially the same results. The two regions of interest are indicated by dashed and solid lines in the FEA (left) and DIC (right) images, respectively. In both cases the strain fields shown in Figure 5.12 are captured at a load of 800 N. Average maximum and minimum principal strains obtained from the regions of interest are plotted against the applied force in Figure 5.12-e and Figure 5.12-f, respectively.

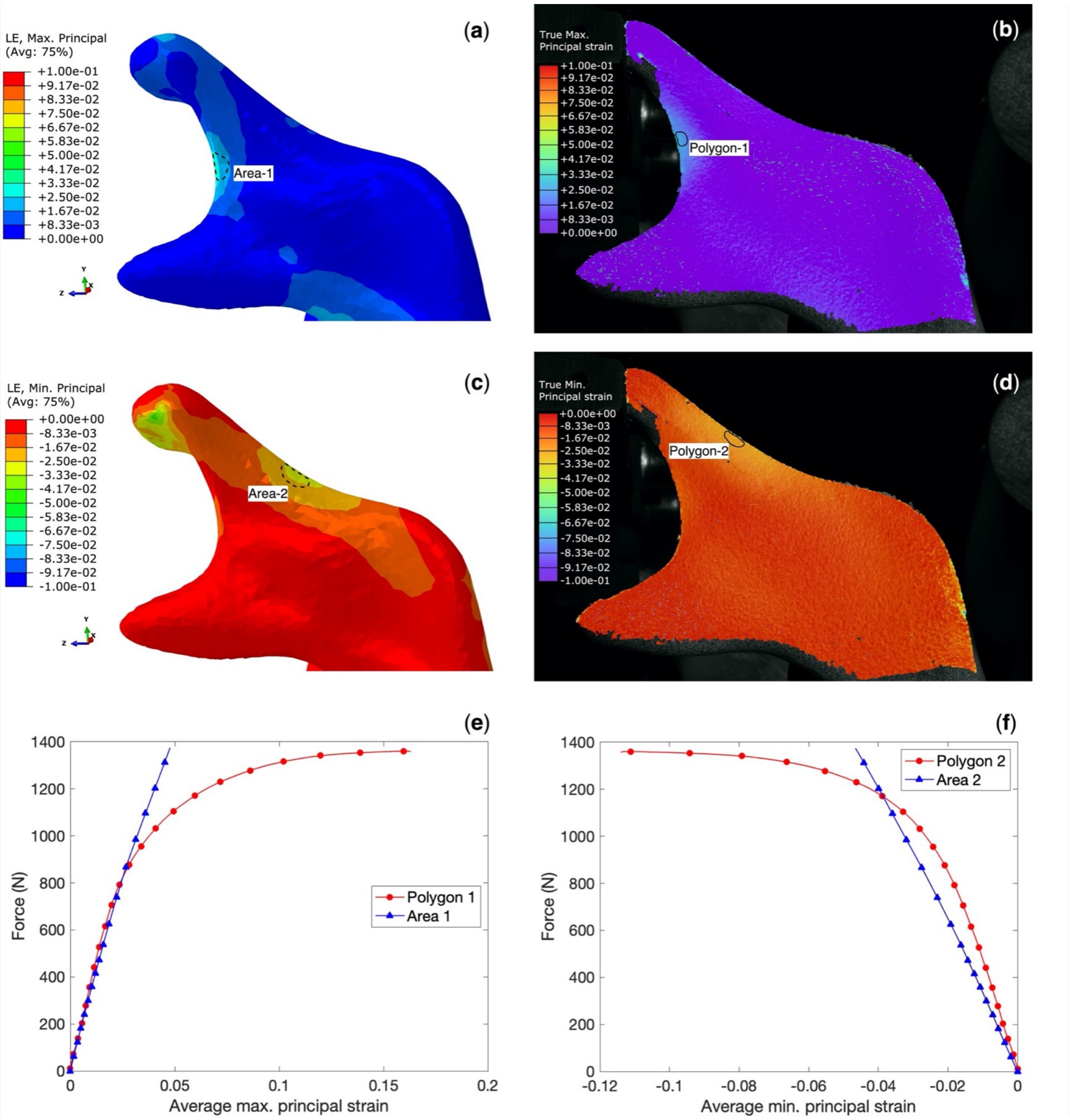

Figure 5.12. Comparison of DIC and FEA principal strains on the non-implanted mandible, with (**a**) FEA predicted maximum principal strain, (**b**) DIC measured maximum principal strain, (**c**) FEA predicted minimum principal strain, and (**d**) DIC measured minimum principal strain. Strain fields correspond to a load of 800 N. (**e**) Average maximum principal strain extracted from surfaces in Area-1 for FEA and Polygon-1 for DIC. (**f**) Average minimum principal strain extracted from surfaces in Area-2 for FEA and Polygon-2 for DIC.

Figure 5.12-e shows that the maximal principal strains obtained by DIC for Polygon-1 correspond well with the strains predicted by the FE model for Area-1 within the linear elastic limits (i.e., between 150 N and 850 N as determined from the force-displacement curve in Figure 5.1). Figure 5.12-f shows

that the minimal principal strains in both regions are proportional but slightly larger for Area-2 compared to Polygon-2, with a difference of 31% at a load of 850 N. This deviation might be related to a difference in camera angle, which becomes important when extracting data from the far edge of the sample surface.

True effective (von Mises) strain fields obtained with DIC at the time of failure of the specimen are shown in Figure 5.13-a, 5.13-b and 5.13-c for the non-implanted, lattice-implanted, and TO-implanted mandibles, respectively. Corresponding with the location of fracture, nearly all the strains were concentrated at the posterior (top) and anterior (bottom) surfaces of the condylar neck. In the case of the implanted mandibles, strains at the posterior side of the condyle increased due to the bending moment that was created by the edge of the implant. Strains on the anterior side of the condylar neck were comparable between the three samples.

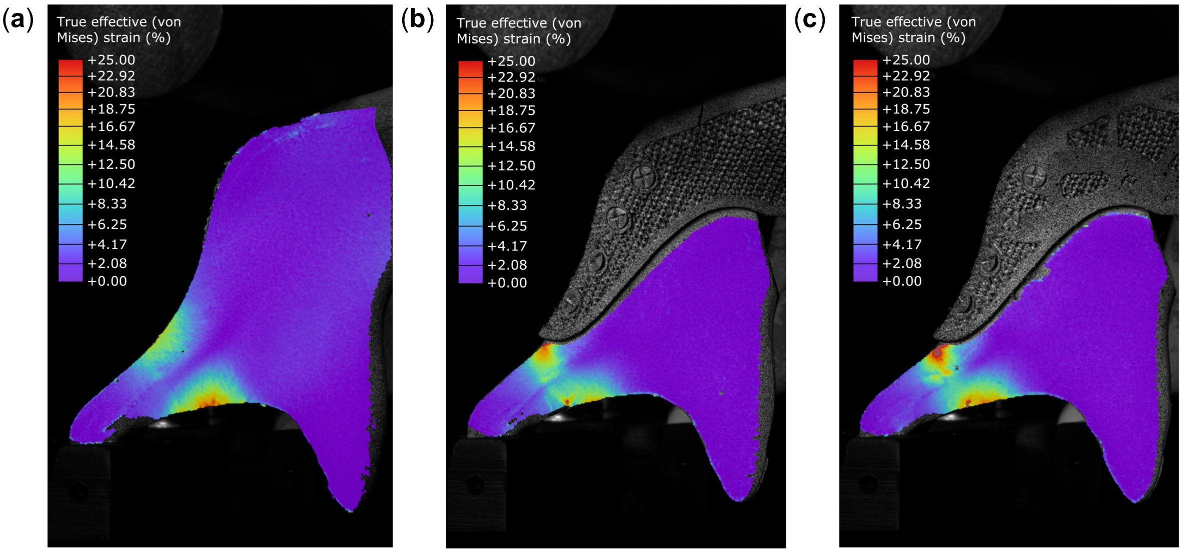

Figure 5.13. True effective strain (%) contours on the bone of the (**a**) non-implanted mandible, (**b**) lattice-implanted mandible, and (**c**) TO-implanted mandible at the time of failure of the specimen.

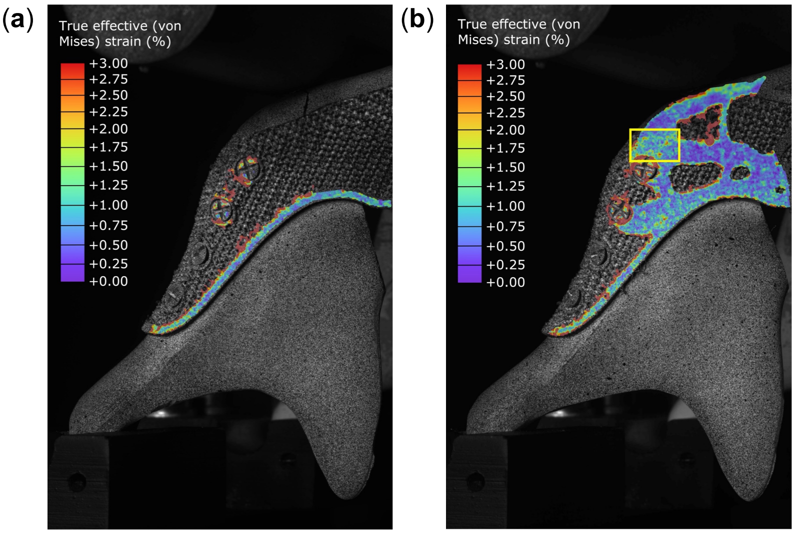

Figure 5.14. True effective strain (%) contours on the (**a**) lattice implant and (**b**) TO implant at the time of failure of the specimen.

It was not possible to obtain strain contours on the porous part of the implants as its highly irregular surface hampered the application of an appropriate speckle pattern. Therefore, strains could only be calculated for (some of) the flat surfaces on the edge of the LA implant (Figure 5.14-a) and across the solid volume of the TO implant (Figure 5.14-b). Also the ‘flat’ non-porous parts of the implants had a relatively high surface roughness as the implants were not polished after 3D printing. Because of this, a noisy strain pattern was obtained which was difficult to analyze. The high strain values that were locally distributed around the borders of the flat edges or in the porous regions could also be regarded as noise or calculation errors. Especially in the case of the LA implant, the information provided is too little and too noisy to draw meaningful conclusions based on strain distributions. In the case of the TO implant, however, higher levels of strain (>1%) seemed to be present right below to the first posterior screw near the resection margin, as indicated by the yellow box in Figure 5.14-b. This observation would agree with the FE predicted stresses as shown in Figure 5.9-b. Yet in this case too, strain contours were hard to read due to the noise, so accurate determination of strain remained practically impossible.

5.2.3. Dynamic mechanical behavior

Regarding constant-cyclic-method, all tested samples completed the maximum number of cycles without bone failure, implant failure, or visible changes in the screw-fixations to the bone. During removal of the implants no looseness of screws was observed. Also for increment-cyclic-method, no implant failure or failure at the screw-substrate interface was observed. The number of cycles to failure and the failure load for each sample are listed in Table 5.2.

Table 5.2. Testing results for increment-cyclic-method.

Sample	Cycles to failure	Failure load (N)
LA-1	501	1820
LA-2	594	2099
TO-1	579	2033
TO-2	448	1647

As with static testing, fracturing during increment-cyclic-method occurred in the condylar neck region of the mandible for 3 out of the 4 samples. One exception was identified (TO-2 in Table 5.2), where the mandible fractured in the region of the external oblique line and anterior mandibular angle (Figure 5.15). The most likely cause for fracturing in this area instead of in the condylar region was manufacturing defects, which were observed in several regions on the outer surface along the fracture line. According to the FEA predictions, the area of the oblique ridge is also associated with high stress concentrations, making it a susceptible region for fracturing, even more so in the case of bony defects.

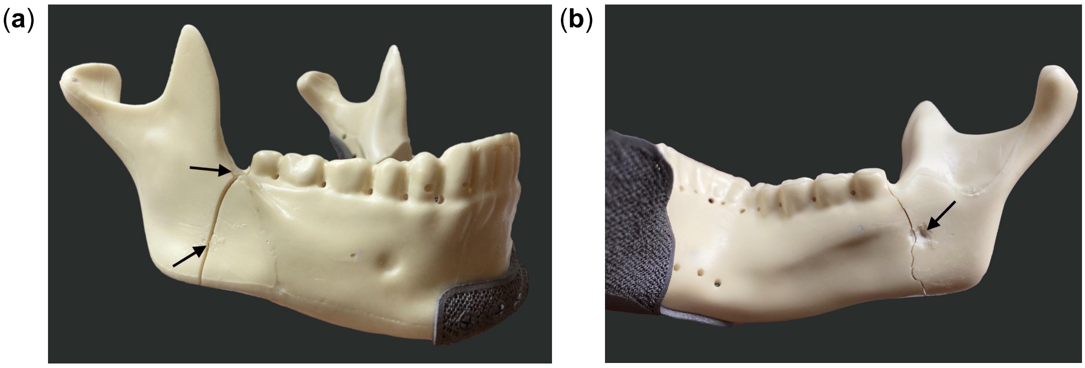

Figure 5.15. (**a**) Lateral and (**b**) medial view of the TO implanted sample that fractured from the external oblique line to the anterior mandibular angle during incremental cyclic loading. Black arrows indicate the location of manufacturing defects along the fracture line.

6

Discussion

6.1. Image processing and implant design methods

For this study, a synthetic (PU) mandible was used for the FE simulations and experimental tests. Image segmentation of the CT-scanned mandible was relatively simple due to the absence of tissues around the mandibular bone that would normally be present (i.e., in clinical situation). To make the workflow suitable for clinical application, a *region growing* step was integrated into the segmentation process, which attempted to simplify the separation of the mandibular bone from its surrounding tissues. As this workflow step was skipped for this non-clinical case, its functionality has not yet been tested. To ensure that this step, as well as all other steps in the workflow function properly for the majority of mandibular reconstruction patients, it should first be tested on multiple patient cases.

Segmental mirroring of the mandible in combination with a sweeping operation was chosen as the most suitable method to estimate the missing shape of the mandible after partial resection. Khalifa et al. (2016) have shown that segmental mirroring of the mandible produced more accurate 3D models and required less intraoperative readjustment of virtually planned pre-bent plates than mirroring the entire unaffected side. Additive manufacturing provides the possibility to design implant shapes that fit the patient-specific anatomy accurately. Designing the implant on the entire mirrored mandible half inevitably leads to a misfit between the connective parts of the implant and the remaining parts of the affected side of the mandible. Therefore, only the segment corresponding to the resected area should be estimated and connected with the remaining mandibular segments. Moiduddin et al. (2016) compared the mirroring reconstruction technique with the 3-Matic build-in anatomical reconstruction function, with which the plane of one segmental end was extruded towards the end of the other segment following a centerline between both segmental planes. The extrusion method resulted in less surface deviation from the reference mandible. However, the segmental resection investigated in their study was small, so the extrusion-based method might produce less precise shapes in the case of larger segmental resections. Besides, a slight misfit of the outer profiles was found between the flat ends of the remaining segments and those of the estimated segment in this study, and therefore modification through additional post-processing steps would be required.

Estimation using SSM did not give accurate results, at least not without the additional need of extensive post-processing procedures. It must be mentioned that the SSM script is developed for edentulous cases, and updates on this method to include dentulous cases would be a great addition to the workflow. The reason for this is that the mirroring technique is only suitable when there is still a healthy side left. Therefore, central defects, lesions that cross the midline, and highly asymmetric mandibles are not suited for shape estimation with the mirroring technique. SSM on the other hand would (ideally) work, independent of the location of resection or the presence of sagittal asymmetries in the mandible.

The implants used in this study were designed in the shape of a cage. Several case reports have produced successful clinical outcomes with a reconstruction implant in the shape of a cage or tray (Kondo et al., 2015; Malekpour et al., 2014; Rachmiel et al., 2017; Yamashita et al., 2008). Three major advantages of using a cage design can be inferred from these studies. First, the natural configuration of the mandible can be reproduced, leading to better aesthetics and patient satisfaction. Second, the procedure will require no special surgical experience, thereby saving operative time and reducing risks for complications. Third, autogenous bone grafts can be loaded into the cage, which will promote bone formation and assist the healing process. PCBM grafts are typically harvested from the patient's iliac crest. This harvesting procedure can be performed with lower risks for postoperative complications and without leaving substantial bone (continuity) defects. However, some potential disadvantages of a construction with a cage and PBCM exist. Risks for bone resorption, wound dehiscence, extraoral implant exposure, and post-operative infection, leading to partial or total loss of the construction, remain significant (Tideman et al., 1998; Kumar et al., 2016). This applies mainly to the patients that require resection of malignant tumours and substantial amounts of soft tissue. Nevertheless, this approach can still be used for the patients that have benign defects, have not been radiated or will be radiated, and where soft tissues are compromised to a limited extent. To minimize risks of infection and prevent contamination through the oral cavity, a two-stage intervention might be desirable, in which first the resection is performed in combination with plate fixation, and after healing reconstruction can take place through the neck. Important to mention is that the application of the current workflow is not limited to the design of cages but can be used to create patient-specific reconstruction *plates* (or basically any desired geometry) as well. A final note on the implant design in the case of clinical application would be that the edges on the bridging part of the implant should not have an inward overhang, which is the case with this design (even though very slightly). This would namely make it impossible to remove the implant if infection would occur at a later stage, and when the bone graft has secured itself across the full width of the implant by that time.

Whether a load-bearing implant will be successful depends to a large extent on its ability to reproduce the mechanical behavior of bone and to promote osseointegration. In order to achieve implant fixation through bone ingrowth and hence allow for full integration between the mesh and the bone, a porous structure was implemented in the implant designs. There are a number of reasons why it is beneficial to implement porosity in the implant design. First of all, for a given volume a titanium implant is heavier than bone. Inclusion of porosity in the implant design reduces the weight of the implant and thereby increases the comfort of the patient.

Secondly, bone density is continuously changing throughout life due to the process of bone remodeling. This means that, according to Wolff's law, bone resorption and formation occurs in response to the amount of mechanical stress that bone is receiving (Burke and Goodman, 2008). In general, bone that is subjected by to higher levels of stress will be triggered to generate more bone, whereas bone that experiences low levels of stress will atrophy. Completely solid titanium implants are usually much stiffer than the bone that lies adjacent to the implant. For instance, the elastic modulus of dense Ti-6Al-4V lies around 110 GPa, whereas the average elastic modulus of bone ranges between 0.5 GPa and 20 GPa (Yan et al., 2015). Because of this large difference in stiffness, the implant prevents the transfer of the applied stress to the adjacent bone. Since the loading on the bone decreases, the density and therefore strength of the bone will decrease. This phenomenon is known as "stress shielding" (Burke and Goodman, 2008). The resorption of bone around the implant weakens the implant support and may eventually result in bone fracture and implant loosening. The inclusion of porosity, possibly in combination with topology optimization, decreases the stiffness of the implant to a value that is similar to that of bone usually without compromising on its function and performance, thereby positively affecting the longevity of the implant.

Finally, the presence of pores in an implant design is extremely important for facilitating bone ingrowth, promoting angiogenesis, and disrupting fibrosis (Koschwanez and Reichert, 2013). The pore size determines whether there is enough void space for oxygen and nutrients to migrate to the inner regions of the porous biomaterial. A minimum pore size of around 400 μm has been shown to be optimal for bone tissue regeneration, a pore size below 200 and 300 μm may hinder cell proliferation and cell migration, and pore sizes lower than 100 μm should generally be avoided (Bobbert and Zadpoor, 2017; Zadpoor, 2015). Generally, a porosity (V_{void}/V_{total}) of at least 50% is required for sufficient tissue ingrowth. However, a high porosity that approaches the porosity of bone (70% - 90%) has been proven to provide the best bone ingrowth and highest cell viability, and is therefore most desirable (Z. Wang et al., 2017). On the other hand, a too large pore size could compromise the structural integrity of the porous scaffold, meaning that it may not be capable of providing enough mechanical support particularly when used in load-bearing applications. Besides, a larger pore diameter reduces the surface area for cell adhesion.

The choice of the dode structure as the unit cell type was based on previous studies, in which dode structures were analyzed and 3D printed for this application. Porosity, pore size and strut size were based on visual inspection, as well as ideal conditions for osseointegration according to the literature. Moiduddin et al. (2020) have developed a mandibular reconstruction implant with a graft carrier that consists of a porous mesh structure (Moiduddin et al., 2019; Moiduddin et al., 2020). The unit cell used for this graft carrier was also a dode unit cell structure, created with the Materialise Magics® software. They have investigated the three different dode structures shown in Figure 4.9 for their EBM manufactured implant. Visual inspection of the three different dode structures at various unit cell sizes (1, 2 and 3 mm) led to the conclusion that the 2 mm dode thick unit cell structure was most suitable for their implant. In their experience, the thick structure was interconnected through a good network of channels without any voids and gaps, in contrast to the thin and medium structures. The 1 mm unit cell contained trapped powder particles and the 3 mm unit cell contained gaps and discontinuities between the junctions. The 1.5 mm dode medium unit cell was found to produce the most optimal result in this study, resulting in an in-plane pore size of 460 µm and a porosity of 87.5%.

Definition of implant thickness, solid edge widths and screw positioning was also done based on the examples and requirements found in the literature, as well as according to the advice from maxillofacial surgeons. Bone screws that are suitable for actual reconstruction surgery were used for the experiments to imitate the clinical situation as accurately as possible. The distance between screw hole was set at 8 mm based on the literature on steel constructions. In comparison, the minimum screw hole spacing is also 8 mm for standard plates such as the DePuy Synthes® MatrixMANDIBLE™ Recon plate (Wilde et al., 2014). 2.4 mm bicortical titanium cortex screws (non-locking) were used for fixation of the implant to the mandible. Screws with a diameter of 2.4 mm have an established history of mandibular reconstruction plate and implant testing (Doty et al., 2004, C.-H. Li et al., 2020, Schupp et al., 2007, Gateno et al., 2013, Peng et al., 2021; Wu et al., 2017). In some cases, the use of locking screws might be preferred over non-locking screws. The reason behind the use of non-locking screws instead of locking screws is that specifications for the screw dimensions were not publicly available and therefore the threading inside screw holes could not be designed accurately. Besides, the 3D printing accuracy would probably be too low to print smooth screw thread. This study has shown that non-locking screws provided sufficient mechanical stability for the implants developed in this study. This is of course only true under the assumption that screw pull-out strength for real bone is similar to that of the PU mandible, which has been shown to be the case (Bredbenner and Haug, 2000).

The two cage designs had identical shapes, and both designs were derived from a fully solid model of the implant. The lattice implant was made fully porous, whereas the TO implant was obtained by merging the design of the lattice implant with the results from topology optimization of the solid implant model. A similar approach of integrating a topology optimized structure into a porous mandibular reconstruction implant design is described by Peng et al. (2021).

The main focus of this thesis was to develop a workflow for the designing of implants and to predict their performance both computationally and experimentally. Refinement of the implant design itself, for example with respect to unit cell type and dimensions, as well as the number of screws, screw position, screw diameter and inter-screw distance, was thus not prioritized, and remains mostly patient-dependent. Even though the implant used for this research was developed to be as suitable for clinical application as possible, its design still remains a proof of concept. Design improvements can be made in collaboration with the maxillofacial surgeon based on the needs and clinical situation of the patient.

6.2. FEA methods

Due to the complex geometry, structure, and function of the mandible, it is of great importance that FE models of the mandible are extensively validated. The current work adopted a double validation strategy: first, an ‘experimental FE model’ was developed to reproduce the simplified experimental conditions as closely as possible. This simplified model was then, under the same boundary conditions and coordinate system, extended to include the multidirectional muscle forces and heterogeneous distribution of bone material. Stresses and displacements in this ‘physiological FE model’ were compared with the data from the literature as a secondary validation.

Several material simplifications were made in the FE models, which generally had the purpose to reduce computational efforts. Firstly, bone was modeled as an isotropic material (i.e., identical mechanical properties in all directions), whereas bone is in fact anisotropic. Secondly, all materials were modeled as linear elastic, which assumes a constant stiffness of the material, also when deformation occurs. Finally, stress relaxation/hardening effects and load redistributions that typically occur during dynamic loading of materials were not considered in a static FE analysis. As a result of these simplifications, some discrepancies may be evident between the absolute stresses obtained with FEA and the experimentally derived strength, especially in the case of large deformations. The PU material used in the experiments is isotropic and is therefore correctly modeled in the experimental FE model. To stay away from the effects of plasticity, the experimental FE model was compared with the experimental data only at forces that lay within the linear elastic range of the force-displacement curve. Deformations and strains in the physiological FE model are much smaller. Estimating the bone to behave as an isotropic linear elastic material will be legitimate in that case, according to the infinitesimal strain theory.

Material properties of the PU mandible cortex were defined based on conformity with experimental results. The elastic modulus (0.41 GPa) was close to the one used by Koper et al. (2021), who used the same mandible analog and estimated its elastic modulus with the value of standard PU (0.5 GPa). The material properties of actual bone in the physiological FE model were based on the grey scale values obtained from the CT images. The HU values were converted to the ranges for density and elastic modulus found in the literature. The numbers of materials chosen to describe cancellous and cortical bone, 5 and 10, respectively, were estimated and do not necessarily reflect the variation in materials of real mandibular bone. In fact, the number of materials could theoretically be reduced to two, considering the way the mandibles are manufactured with two distinct regions of cancellous and cortical bone. Nevertheless, a more diverse spread of HU values was obtained from the CT images (Figure 4.15), indicating that there might be some transition regions between the cancellous and cortical bone, as well as some higher-density areas in the cortical region. These differences were captured within the 15 different material assignments and assumed to approximate the anatomical situation more accurately than when only 1 material value would be used for the cortical and cancellous bone regions. Average cortical bone material (E = 30.1 GPa) found for models of the dentulous mandible was assigned separately to the outer surface of the whole mandible to bypass PVE issues.

Normally, a layer of periodontal ligament (PDL) is located between the tooth roots and the alveolar sockets. This is very thin tissue that usually cannot be captured with the resolution of regular CT scans. The PDL is important for transferring the force to the alveolar bone. Even though some FEA studies have included this soft layer between the teeth and the bone, it is often excluded from the model as it involves time-consuming manual segmentation and increases processing time as a result of the higher model complexity (Gröning et al., 2012). However, several studies have found that FE models show a much higher stiffness, and hence lower strains, when teeth and bone were modeled as continuous, compared to when the PDL was included (Gröning et al., 2012; Marinescu et al., 2005). It would be recommended for future studies to perform sensitivity analyses on the influence of PDL on the current FE model.

The use of an identical mandible model in all FE models is a major advantage in the analysis of the results as it allows for direct quantitative comparison of stresses and strains observed in the different implanted and non-implanted models. The same advantages of consistency in model geometry apply to the individual mechanical experiments, as well as in the ability to directly compare FE results with experimental data.

The literature on loading and boundary condition methodologies to predict the performance of mandibular reconstruction systems has been investigated. Two different methods to define loads and boundary conditions can typically be identified (Table 6.1). In the first method, node sets on both condyles are fixed in all directions, and a specific region on the dental arch is constrained to prevent vertical translation. The masticatory-induced stresses are simulated with force vectors of the different muscle components at anatomically correct positions on the mandible. The second method also includes fixation of node sets on both condyles. However, in this case a specific region on the dental arch is vertically loaded while the muscular insertion areas are now fixed. Most of the studies investigating lateral defects applied molar loading at the unaffected side, while some included incisal/central loading or loading at the affected side. The latter requires the presence of molars or dental implants at the affected side. Loads and boundary conditions in this study were applied according to the first method with molar loading at the unaffected side, as well as incisal loading.

Table 6.1. Summary of literature study on loading and boundary condition methodologies.

Loading area	Fixation area	References
Muscle forces	Condyles and dental arch	*Al ahmari et al. (2015); Cheng et al. (2019a); Cheng et al. (2020); Gao et al. (2019); Jadahakbar et al. (2016); Moiduddin et al. (2019); Narra et al. (2014); Pinheiro et al. (2015); Wong et al. (2012b)*
Dental arch	Condyles and muscle insertion areas	*Huo et al. (2015); Kimura et al. (2006); Nagasao et al. (2002); Nagasao et al. (2003);*

The regions associated with high von Mises stress values observed in Figure 5.2-a correspond well with the primary locations of failure observed during experimental testing, namely the area of the condylar neck. Also, the deformations shown in Figure 5.2-b correspond well with the deformation of the samples during experimental testing (Figure 5.3). This would indicate correct implementation of boundary conditions and application of force. Direct qualitative assessment of the stresses is not possible since yielding properties of the PU material used for the mandibles are not available. Besides, it would not be relevant either since we are not interested in the material mechanics of PU, but primarily the reliability of applied loads and boundary conditions. As an indication, compressive strength for PU foam with densities between 0.240 – 0.641 g/cm^3 ranges between 4.7 and 24.7 MPa, according to Calvert et al. (2010). Assuming that the PU used in the cortical region is of high density, the maximal stress of 16 MPa observed in the FE model in the condylar neck region at a loading of 804 N fits well within this range of compressive strength.

Asymmetry in the stress and displacement fields of the healthy-model with the INC conditions can be seen in both the experimental FE model (Figure 5.2) and physiological FE model (Figure 5.4 and Figure 5.5), indicating some sagittal asymmetry in the mandible model. However, the degree of asymmetry is so low that its contribution to asymmetrical implant loading can be neglected.

The agreement in deformation patterns observed in Figure 5.4 indicates correct implementation of muscle forces vector directions and relative muscle force magnitudes. Good agreement between the stress patterns observed in Figure 5.5 and those reported in Pinheiro and Alves (2015) indicates correct scaling of muscle forces.

Maximum stress levels are higher for RMB than INC in all three implanted models. The maximum von Mises stresses in the mandible bone, i.e. 20 MPa, 55 MPa, and 36 MPa for the solid-implant-model, LA-implant-model, and TO-implant model under RMB conditions, respectively, are well below the yield strength of cortical bone. The difference in stress values between the left and right in the case of INC is expected because of the unequal distribution of forces between the two sides (the masseter and medial pterygoid muscles are not active on the implanted side). In all three implanted cases, the condylar neck on the contralateral side is stressed the most during INC, whereas the condylar neck on the lateral side is stressed the most during RMB. This observation agrees well with the quasi-static testing results shown in Figure 5.10, where fracturing under the INC-70/30% condition occurred in the contralateral condyle in all cases, while under the RMB-70/30% condition fracturing occurred in the lateral condyle in all cases. Where stress levels on the contralateral side of the mandible are comparable for the three implanted models, the stress levels on the lateral side of the mandible seem to increase with decreasing stiffness of the implant: in the LA-implant-model, maximum stress value on the anterior surface of the condylar neck is 55 MPa. For the TO-implant-model and solid-implant-model, however, these values are reduced to 24.8 MPa and 15 MPa, respectively. The resistance of the implanted mandible to deformation is depended on the stiffness of the implant. For a lower implant stiffness, the resistance to deformation is small, and as a result the equivalent stresses will be higher in the bone surrounding the implant. The opposite is true for implants with a higher stiffness. In that case more load is transferred trough the implant, which thereby shields the surrounding bone from higher levels of stress.

Maximum stresses on the implants can be found just below the first screw hole near the posterior resection margin. The average stress magnitudes observed in this region are considerably lower than the yield strength of the titanium alloy used. However, high stress values, which even exceed the yield strength in some critical areas, are located in the sharp corners of the unit cell struts. The fact that none of the implants showed any damage in these critical regions after mechanical testing at loads much higher than those used in the physiological FE models confirms that these high stresses are unreliable, and much likely caused by numerical singularity errors. In order to be able to quantify the results of the FEA based on peak stresses, the singularity points should first be eliminated. However, manually removing all the sharp corners would be too time-consuming, and the large number of elements required to model the fillet geometries would tremendously increase the computational demand.

DIC measurements

The grey value pattern in each facet should be random and unique for DIC to be successful. For that, several speckle pattern requirements must be met. Besides having a non-repetitive, high contrast and isotropic pattern, surface roughness should be minimized to reduce alterations in the geometry of the surface, and speckle dots should ideally correspond to 3-5 pixels with the surface being 50% white and 50% black. All these conditions can be mostly satisfied on the surface of the bone as these are all locally flat and smooth surfaces. However, the porous regions inside the implant cause some surface points to be hidden inside a groove of the surface. Hence, one camera will view a different surface pattern from the other because of this local curvature, thereby impeding the correlation between the views of both cameras. In addition, shadows created by the struts adversely affect the contrast in the images. The inability to correlate the camera views hampers the DIC image registration and therefore strains could not be measured in the porous implant regions. The strain pattern is also relatively noisy in the ‘flat’ non-porous areas due to the high roughness of the implant surface that has not been polished or sanded. In the case of the lattice implant, the measurable surface is very small and extremely noisy. Therefore, no useful information can be extracted from this measurement. In case of the TO implant, the average strain seems to be somewhat higher in the ‘critical’ regions of the implant, which is just below the first posterior screw closest to the resection margin, as well as near the edge of the implant above this screw. This would be in agreement with the predictions of the FE models. However, due to the low quality of the measurement, it is not possible to say with certainty that the higher stress values in this area are not affected by noise, so firm conclusions should not be drawn based on the strain distributions on the implants themselves. Polishing or sanding the implant surface, in combination with more closely positioned cameras may improve measurement sensitivity.

In the FE model that replicates the experimental conditions the highest stresses and strains are concentrated on the anterior and posterior sides of the condylar neck. This corresponds very well with the region of fracture obtained with biomechanical experiments, as well as the strain fields obtained with DIC. According to Figure 5.13, higher levels of strain can be observed in the posterior side of the condylar neck in the case of the implanted mandibles compared to the non-implanted mandible. However, this is for very high loads that are physiologically not achievable, especially not by the patients that have had reconstruction surgery. In the FE model, high stresses are also observed along the oblique line. Unfortunately, this anatomical feature is not present in the DIC field-of-view. However, fracturing of one of this samples in this area confirms the vulnerability of this area by experiment.

The full-field strain distributions obtained with DIC were very similar to the strains predicted by the FE model (Figure 5.12). Maximum and minimum principal strain values are extracted from two regions on the outer surface edges of the bone. Especially when the surface on the outer edges is curved, the subtended angle of the camera viewing direction with respect to the sample will play an important role. As the curvature on the anterior surface of the condylar neck (region of Polygon-1) is relatively sharp, the DIC will always capture approximately the same region when the images are taken from a sideperspective at slightly different angles. However, the curvature on the posterior surface of the condylar neck (region of Polygon-2) is relatively blunt. Therefore, the higher the cameras are positioned, the more the back of the condylar neck will be exposed to the cameras, which is where the strain values are expected to be the largest (Figure 6.1). Since this area is not fully captured by the cameras, it is likely that the Polygon-2 area covers a region with lower maximum strain values than those covered by Area-2 in the FE model, leading to lower average minimum principal strain values for DIC compared to FEA. Especially at the curved boundaries, peak strains could also be underestimated due to averaging errors, as the resolution depends on the pixel subset size used for strain calculations (Chanda et al., 2015). Placing the cameras closer to the normal of the surfaces at strain peak regions would be an option to improve accuracy. Finally, a limitation regarding the comparison of DIC measurements with FEA results in this study is that only one specimen was tested with DIC. Comparing FEA with averaged DIC data from multiple specimens may reduce the margin of error.

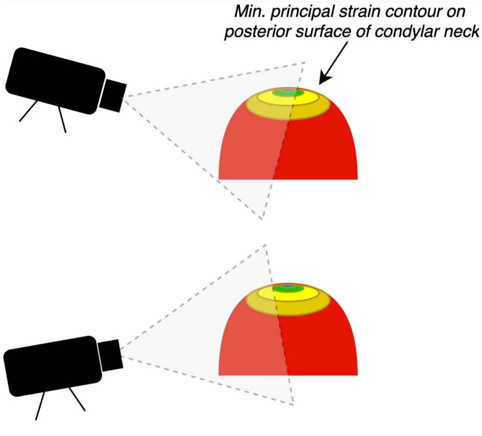

Figure 6.1. Illustration showing the effect of camera angles on the observed strain fields in regions with high curvature.

6.3. Experimental methods

As with setting up a biomechanical FE model, one aims to mimic the physiological situation as much as possible when designing an experimental testing setup. Most studies found in the literature used an approach similar to that used in this study to assess the performance of their reconstruction system by experiment (Fontana et al., 2016; Gateno et al., 2013; Rendenbach et al., 2017; Schupp et al., 2007; Koper et al., 2021). An example of this experimental setup used by Schupp et al. (2007) is shown in Figure 6.2.

A variation on the experimental setup described above involves fixation of the mandible by placing a rod through the coronoid regions, thereby allowing the condyles to function normally. Then, vertical linear loads are applied on the incisal or molar region using a servohydraulic mechanical testing unit. This experimental setup is well represented in the literature and has been used for many years to evaluate osteosynthesis products in the treatment of mandibular fractures (Dichard and Klotch, 1994; Haug et al., 1998; Haug et al., 2001; Kalfarentzos et al., 2009; Madsen et al., 2008).

It is very challenging to mimic the *in-vivo* three-dimensional loading configuration of the mandible, and therefore requires simplification. Seebach et al. (2017) showed that the biting forces could be described by a resultant vector that originated from the mandibular angles. This approach was translated into the current setup by uniaxial forces acting on both mandibular angles. Simplification of the complex biomechanics of the mandible in the experiments facilitates reproducible measurements, leading to more consistent outcomes. Muscular forces on the reconstructed side have been compromised to a certain extent, leading to an unequal distribution of biting forces between the two sides (Marunick et al., 1992; Curtis et al., 1999). The muscles that cannot retain function after reconstruction have been removed from the FE model, whereas in the experimental setup this loading imbalance has been accounted for by distributing 70% and 30% of the total forces on the healthy and affected side, respec-

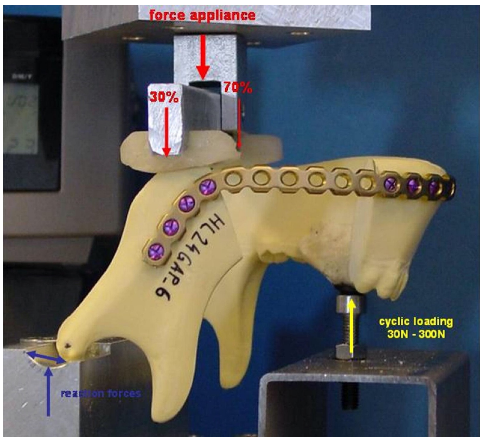

Figure 6.2. Example of the “three-point” fixation method used by Schupp et al. (2007). The condyles and a specifically chosen area on the dental arch are constrained, while a see-saw device applies a distributed load on the mandibular angles.

tively. Important to mention is that the respective force distribution of 30% and 70% on the mandibular angles of the affected and healthy side is estimated due to the absence of reliable data in the literature. In an attempt to induce implant failure, loads on the implant were increased by transmitting the load equally between the two sides. A similar approach to attempt failure at the implant instead of the mandible failure was taken by Gutwald et al. (2017).

Small cavities were visible primarily in the cancellous portion of most of the mandibles in the CT images and after cutting of the specimens. For each mandible, these cavities differed in number, size, and location, and are therefore assumed to be manufacturing defects. Even though the cancellous bone region has little effect on the mechanical stiffness of the construct, these cavities might have affected the strength of the mandibles during mechanical testing to a limited extent.

Torsional movements of the samples in the RMB 50/50% loading configuration impeded proper acquisition of mechanical properties from the load-displacement curves. An example of this torsional movement is shown in Figure 6.3. This torsion results from a sagittal misalignment between the location of tooth support and the location of the resultant loading. The degree of torsion is unpredictable and depends on several factors, including the small differences in sample preparation (i.e., cutting of the mandible and position of screws) and the differences in starting positions between measurements. This led to increased instability of the sample position throughout the test and therefore inconsistent results between samples within the same group. The inability to test under this loading configuration is not something to worry about since equal distribution of loads on both sides of the mandible during RMB is also physiologically unrealistic. This loading configuration was then tested only to put the implants under the heaviest loading conditions to induce fracture. Similar torsional movements were observed in the RMB 70/30% group, however to a much lesser extent as the resultant load is much more aligned with the location of tooth support in the sagittal plane. These small torsional deformations are normal and were also observed in the FE model of the healthy-model under RMB loading conditions, as shown in Figure 5.4.

Markwardt et al. (2007) have shown that for clinical cases plate fracture and screw loosening are predominantly caused by the transfer of muscle forces to the opposing teeth in the maxilla or mandible, as well as by material fatigue from bending of the reconstruction plate during the surgical procedure. Two different methods were used to test for fatigue in the system, denoted as constant-cyclic-method and increment-cyclic-method. In the former method, the load cycled between a constant minimum and maximum compressive stress amplitude at a physiological force range. A similar method was used by Schupp et al. (2007) and Wu et al. (2017). The second method of increasing the load with each cycle until specimen failure was applied similarly by Gateno et al. (2013) and Rendenbach et al. (2017). The fact that none of the implants failed during quasi-static testing, either through fracture or screw/implant loosening, at loads far above maximal physiological biting forces indicates that the reconstruction is

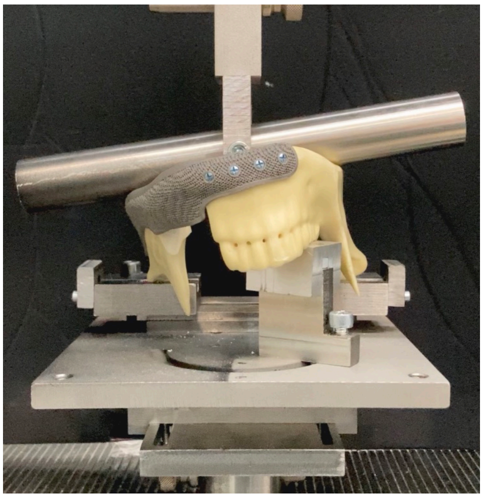

Figure 6.3. Example of the torsional movement observed during deformation of the mandible in a RMB 50/50% loading condition.

stable. Fatigue tests performed according to constant-cyclic-method have indicated that the high stability of the reconstruction systems remains for at least 250.000 cycles of biting at relatively high forces. Also, no fatigue failure in the osteosynthesis was observed during increment-cyclic-method. Since the implants are additively manufactured to the specific anatomy of the patient, intra-operative bending of the implants is not required.

No significant differences ($P < 0.01$) in stiffness, ultimate load and ultimate displacement were found between the healthy control mandible, lattice implanted mandible, and TO implanted mandible. The fact that no clear differences were observed between implanted and non-implanted mandibles would indicate that both implants perform well in taking over the function of the resected segment. However, the low sample size per loading condition can be seen as a limitation of this study as it reduces power of the statistical analyses. Still, the variation between samples was minimized by using identical mandible models, using a surgical guide to create nearly identical resections, and ensuring identical positioning of the samples during testing. Consequently, low dispersion of the data points within each group is obtained, making it safer to draw conclusions on the significance of the relative differences between groups despite the low sample size.

The low von Mises stresses observed in the solid implant in Figure 5.9 indicate that the solid implant would perform well in the sense that no implant fracturing is expected to occur under the applied loads. Besides, the low stress levels observed in the solid implant support the assumption that the exceedingly high stresses observed in the lattice and TO implants are most likely the result of stress singularities rather than improper design. Yet, no experimental tests were performed on the solid implant model, as it was not considered suitable for clinical application. Its high stiffness and complete absence of implant permeability would almost certainly lead to atrophy of the bone graft, and thereby reduces the chance for implant survival significantly. Therefore, the main comparison in implant performance was made between the lattice implant and TO implant. Table 6.2 lists the most important findings for the two implant designs, distinguishing between design outcomes and mechanical performance. Values for the mean construct stiffness, mean ultimate load and mean ultimate displacement are shown for INC 70/30%, which is considered as the most critical, yet physiologically relevant loading condition.

Since the mechanical performance of the lattice samples and TO samples were not found to be significantly different, the lattice implant would likely be preferred over the TO implant in case of clinical application for four main reasons. First, the lattice implant weight is lower than that of the TO implant, even though very minor, which will increase wearing comfort and reduces material costs. Second, the lattice implant has a higher porosity, which will likely result in a higher degree of osseointegration and bone tissue regeneration. Third, this increased porosity presumably yields a lower implant stiffness, which is beneficial for reducing stress shielding. And fourth, the relatively time-consuming process of

Table 6.2. Comparison of design outcomes and mechanical performance between the lattice implant and the TO implant.

	Lattice implant	**TO implant***
Design outcomes		
Implant weight (g)	15.8	18.4 (+ 16.5%)
Implant porosity (%)	63.4	52.4 (- 17.4 %)
Estimated workflow time (h)	3	22 (+ 633.3 %)
Mechanical performance**		
Implant failure (static or fatigue)	No	No
Screw loosening (static or fatigue)	No	No
Mean construct stiffness (N/mm)	311.5 ± 8.3	323.3 ± 21.9 (+ 3.8 %)
Mean ultimate load (N)	1200.9 ± 54.0	1271.5 ± 112.0 (+ 5.9 %)
Mean ultimate displacement (mm)	5.3 ± 0.3	4.9 ± 0.4 (- 7.5 %)

* Values within brackets indicate the percentage change with respect to the lattice implant.

** Values for the mean construct stiffness, mean ultimate load and mean ultimate displacement are shown for the INC 70/30% condition.

TO (18 hours for the implant in this study excluding additional post-processing time) can be omitted, thereby shortening the development workflow time considerably for these types of implants.

In an ideal situation, the implant stiffness would match the stiffness of bone to minimize the effects of stress shielding. Additionally, Schouman et al. (2016) evaluated bone ingrowth of load-bearing implants placed in critical-size mandibular bone defects of sheep and found that a reduced overall stiffness of porous implants promotes bone ingrowth. Especially in the case of metallic tray or cage containing a graft transplant, functional stresses are required for favorable growth and healing of the transplanted bone. The bone graft and the remaining mandible segments will then grow together, which in the case of cancellous cellular marrow grafts can take up to 6 months after reconstruction surgery (Marx, 2007). Zhou et al. (2010) investigated six patients treated with customized titanium reconstruction trays. The outcomes were successful, with good aesthetic results and no post-operative complications for five of the six patients. However, radiographic images and implant revision for one of the patients revealed excessive resorption of the inserted bone graft after initial healing. The authors indicated that this atrophy was most likely the result of stress shielding by the trays, which were thick and rigid and had low porosity and therefore a limited blood supply to the packed bone marrow (Figure 6.4). They speculated that this might be improved using a thinner titanium mesh with higher flexibility and high porosity that would permit proper permeation of the blood supply. Besides, the authors believed that the effects of stress shielding were enhanced by designing the dental fixture implants on top of the tray instead of having the dental supports implanted on top of the bony bridge after initial healing of the graft. All these findings support the potential clinical success of the implant designs developed in this study.

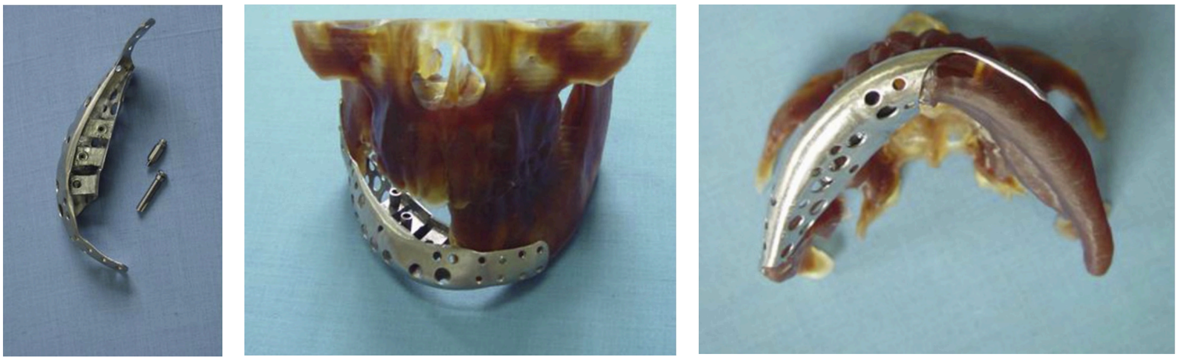

Figure 6.4. Customized titanium tray design in Zhou et al. (2010) that induced autogenous bone graft resorption as a result of stress shielding and limited blood supply.

7

Concluding remarks

7.1. Conclusion

Continuity defects of the mandible typically result from oncologic ablative surgery, infectious diseases, or trauma, and can have a significant impact on a patient's quality of life. Reconstruction of the defect using free tissue transfer with an autologous bone flap is currently the standard procedure. However, this procedure may not by applicable to patients suffering from multiple comorbidities, and it is associated with critical drawbacks, including severe donor side morbidity, long hospital stay and recovery process, need for high surgical expertise, and insufficient bone graft height. Consequently, reconstruction using PSIs is becoming a popular alternative to the procedure with microvascular bone flaps. Yet, a systematic approach for the designing and testing of PSIs used to restore reconstruction defects appears to be still lacking.

A workflow for designing patient-specific implants to restore lateral mandibular defects was developed in this study. The workflow comprised several steps, starting with CT image acquisition and segmentation, followed by the planning of mandibular resection, estimation of the missing segment, and finally designing of the implant. All the image processing and 3D modeling steps were combined in a semi-automatic workflow through Python scripting in the Materialise software environment.

Using the proposed workflow, two proof-of-concept cage-shaped implants, one fully porous and the other topology optimized, were tailored to the anatomy of a synthetic mandible analog subjected to lateral resection. The outer contour of the implants was designed to reproduce the natural shape of the mandible as closely as possible and maximize aesthetics. High porosity was implemented in both implant designs to decrease implant weight, stimulate osseointegration and allow favorable healing of the inserted bone transplant. Both implant designs were manufactured from Ti-6Al-4V using SLM. The use of a surgical guide for cutting and predrilling of the mandibles ensured an optimum implant fit and consistent sample preparation so as to minimize the variation between samples during experimental testing. The excellent fit between the screws and implant, and between the implant and mandibular segments indicates the capability of the workflow in combination with AM to develop customized implants with accurate dimensions.

The mechanical performance of the reconstructed mandibles was predicted with computational FEA and evaluated through quasi-static and cyclic experimental testing. As additional FEA validation, DIC measurements were performed in combination with quasi-static testing and compared with the FEA results at two regions. First, a FE model of the intact mandible was developed to match the simplified experimental conditions as closely as possible. Good agreement between the FE predictions, DIC, and experimental data was found, thereby ensuring the reliability of the computational analysis. The FE properties were extended to match physiological conditions, and a secondary validation on model reliability was established by comparing stress and deformation patterns with FE data reported in the literature.

Normal physiological stress levels on the mandibular bone were observed in the FE models of both implant designs, and overall implant stresses stayed well below the material yielding limit in both cases. Predictions on the performance of the two implants based on maximum stress values was not feasible due to the presence of stress singularities in the porous structure.

With regard to biomechanical evaluation, no significant differences were found in stiffness, ultimate load or ultimate displacement between the intact mandible, mandible reconstructed with lattice implant, and mandible reconstructed with TO implant. In all cases, the mandible itself fractured mostly at the condylar neck region at loads greater than the average biting force of *healthy* individuals. Neither the implants, nor screw-substrate fixations failed during quasi-static or fatigue testing, meaning that the strength of both implants was sufficient to withstand forces considerably higher than average maximum bite forces observed after mandibular resection. This would also indicate that there is still a margin to increase the porosity inside the implants even further. Head-to-head comparison between the lattice and TO implant indicated that the lattice implant would likely be preferred over the TO implant in the case of clinical application due to its lower weight, higher porosity, and shorter workflow time.

The experimental results not only show that the FE simulations are reliable to predict the performance of the implant designs, but also prove that the cage designs developed in this study are highly resistant to mechanically-induced complications, including implant fracture, implant loosening and screw loosening. Besides, the high degree of implant porosity reduces the stiffness of the implant substantially, which will likely result in a decrease of stress shielding without compromise of function. The various translational and rotational degrees of freedom integrated in the stage and tooth support of the experimental setup allow for testing on intact and reconstructed mandibles with arbitrary sizes and shapes, and under almost any desired loading condition. This will be particularly useful when biomechanical tests will be performed on cadaveric mandibles with varying morphologies in future studies.

Creating a plug-in that covers the FEA steps and implementing that into the design workflow was beyond the scope of this thesis project. However, the software platforms used for each process (i.e., image processing, implant designing and FE modeling) allow for GUI customization through Python programming. Therefore, the design workflow is developed such that the end product can be directly transferred to the FEA software. An associated FEA plug-in created at a later stage can then simply be added to the current workflow. The workflow proposed in this study may, after future incorporation of the FEA plug-in, offer surgeons and medical engineers the tools to systematically design and evaluate patient-specific reconstruction implants. This would result in more cost-effective and time-effective presurgical planning, and result in implant designs that can minimize morbidity and maximize aesthetic and functional outcomes.

7.2. Future recommendations

The current Mimics image processing script assumes good quality CT scan data. However, in clinical situations this might not always be self-evident. Therefore, an assessment step in which the quality of the CT data based on region of interest (ROI), number and thickness of slices, and the presence of imaging artifacts (e.g., scatter or movement artifacts) is being examined would be recommendable before entering the design workflow.

In the future, the following features could be implemented in the current implant design script:

- Besides the mirroring technique, provide the user with the option to use SSM for shape estimation. Depending on the region and size of the defect(s), one method might be preferable over the other.
- Allow the user to choose a different length for each individual screw.
- Implementation of lattice structuring in 3-Matic (requires 3-Matic full version).
- The surgical guide developed for this study is not designed to be suitable for clinical application, as there was no need to adapt its design to the clinical situation of a patient. Nevertheless, the clinical engineer should take the patient-specific anatomy into consideration when designing the

guide for clinical application, and therefore it would be recommended to enable the possibility to design the surgical guide along with the implant in a single workflow.

- Define the three-dimensional orientation of the mandible in 3-Matic such that its coordinate system already corresponds with cephalometric standards when loads and boundary conditions will be applied in the Abaqus FEA environment.

It would be recommended to fine-tune the workflow steps based on the feedback from clinical engineers that have more experience in the designing of mandibular reconstruction implants to maximize the workflow efficiency and user-friendliness.

The workflow application presented in this study was tested only on the ‘ideal’ Synbone mandible analog. Therefore, a future plan would be to test the workflow on an actual patient case. Besides, the current design workflow is developed for lateral defect types but could be extended to defects of other types, including central and hemimandibular defects.

Several implant design features, including the implant edge width, implant thickness and strut thickness were estimated based on commercially available implants, as well as examples from the literature. Ideally, parameter variations within each of these features should be examined through sensitivity studies in order to pursue optimal implant performance. Since this was beyond the scope of this thesis project, it would be highly recommended to do so in future studies.

Triply periodic minimal surface (TPMS) unit cell structures, such as gyroid, Schwarz diamond, and Neovius could be investigated in future studies as alternatives to the dode unit cell structure that was used to create implant porosity in this study. Studies have shown that their geometrical resemblance to trabecular bone and especially their curved surfaces might play a critical role in promoting bone ingrowth and osseointegration (Maconachie et al., 2019). Besides, stress-singularities observed in the strut-based lattice structures in this study would not be present in these curved structures.

With regard to the 3D printing process and the implant material, several important aspects should be investigated prior to clinical application. As mentioned in the discussion, no surface treatment steps were included, following the additive manufacturing process of the implants. The effect of heat-treatment and hot isostatic pressure (HIP) treatment on the biological and mechanical properties of the material could be investigated in future studies. To find out whether the lattice structure used in this study induces sufficient bone ingrowth, samples could be examined with tissue-engineered scaffolds and/or by performing animal studies. Additionally, the effects of ceramic or polymer coating to improve biological and mechanical properties of the implant could be investigated (Hudák et al., 2021). Finally, before printing implants for clinical application it is important to fine-tune the 3D printing parameters (e.g., laser power, laser scanning speed, and layer thickness), and to perform quality control of the SLM printed powder material.

Bibliography

Abel, R., Prime, M., Jin, A., Cobb, J., & Bhattacharya, R. (2013). 3d imaging bone quality: Bench to bedside.

Aitchison, G., Hukins, D., Parry, J., Shepherd, D., & Trotman, S. (2009). A review of the design process for implantable orthopedic medical devices. *The open biomedical engineering journal*, *3*, 21.

Al-Ahmari, A., Nasr, E. A., Moiduddin, K., Anwar, S., Kindi, M. A., & Kamrani, A. (2015). A comparative study on the customized design of mandibular reconstruction plates using finite element method. *Advances in Mechanical Engineering*, *7*(7), 1687814015593890.

Almansoori, A. A., Choung, H.-W., Kim, B., Park, J.-Y., Kim, S.-M., & Lee, J.-H. (2020). Fracture of standard titanium mandibular reconstruction plates and preliminary study of three-dimensional printed reconstruction plates. *Journal of Oral and Maxillofacial Surgery*, *78*(1), 153–166.

American Institute of Steel Construction. (2016). *Specification for structural steel buildings*. https://www.aisc.org/globalassets/aisc/publications/standards/a360-16-spec-and-commentary.pdf

Anderson, A. E., Ellis, B. J., & Weiss, J. A. (2007). Verification, validation and sensitivity studies in computational biomechanics. *Computer methods in biomechanics and biomedical engineering*, *10*(3), 171–184.

Ashby, M. F. (2006). The properties of foams and lattices. *Philosophical Transactions of the Royal Society A: Mathematical, Physical and Engineering Sciences*, *364*(1838), 15–30.

Ashby, M. F., & Gibson, L. J. (1997). Cellular solids: Structure and properties. *Press Syndicate of the University of Cambridge, Cambridge, UK*, 175–231.

Attar, H., Prashanth, K., Chaubey, A., Calin, M., Zhang, L. C., Scudino, S., & Eckert, J. (2015). Comparison of wear properties of commercially pure titanium prepared by selective laser melting and casting processes. *Materials Letters*, *142*, 38–41.

Ay, M., Kubat, T., Delilbasi, C., Ekici, B., Yuzbasioglu, H. E., & Hartomacioglu, S. (2013). 3d bio-cad modeling of human mandible and fabrication by rapid-prototyping technology. *Usak University Journal of Material Sciences*, 135.

Bailey, B. J. (2001). *Atlas of head & neck surgery–otolaryngology*. Lippincott Williams & Wilkins.

Bak, M., Jacobson, A. S., Buchbinder, D., & Urken, M. L. (2010). Contemporary reconstruction of the mandible. *Oral oncology*, *46*(2), 71–76.

Bendsøe, M. P. (1989). Optimal shape design as a material distribution problem. *Structural optimization*, *1*(4), 193–202.

Bobbert, F., & Zadpoor, A. (2017). Effects of bone substitute architecture and surface properties on cell response, angiogenesis, and structure of new bone. *Journal of Materials Chemistry B*, *5*(31), 6175–6192.

Boyd, J. B., Gullane, P. J., Rotstein, L. E., Brown, D. H., & Irish, J. C. (1993). Classification of mandibular defects. *Plastic and reconstructive surgery*, *92*(7), 1266–1275.

Brand, R. W., & Isselhard, D. E. (2014). *Anatomy of orofacial structures-enhanced 7th edition-e-book: A comprehensive approach*. Elsevier Health Sciences.

Bredbenner, T. L., & Haug, R. H. (2000). Substitutes for human cadaveric bone in maxillofacial rigid fixation research. *Oral Surgery, Oral Medicine, Oral Pathology, Oral Radiology, and Endodontology*, *90*(5), 574–580.

Burke, M., & Goodman, S. (2008). Failure mechanisms in joint replacement. *Joint replacement technology* (pp. 264–285). Elsevier.

Calvert, K. L., Trumble, K. P., Webster, T. J., & Kirkpatrick, L. A. (2010). Characterization of commercial rigid polyurethane foams used as bone analogs for implant testing. *Journal of Materials Science: Materials in Medicine*, *21*(5), 1453–1461.

Chanda, S., Dickinson, A., Gupta, S., & Browne, M. (2015). Full-field in vitro measurements and in silico predictions of strain shielding in the implanted femur after total hip arthroplasty. *Proceedings of the Institution of Mechanical Engineers, Part H: Journal of Engineering in Medicine*, *229*(8), 549–559.

Cheng, K., Liu, Y., Yao, C., Zhao, W., & Xu, X. (2019). A personalized mandibular implant with supporting and porous structures designed with topology optimization–a case study of canine. *Rapid Prototyping Journal*.

Coletti, D., Ord, R., & Liu, X. (2009). Mandibular reconstruction and second generation locking reconstruction plates: Outcome of 110 patients. *International journal of oral and maxillofacial surgery*, *38*(9), 960–963.

Curtis, D., Plesh, O., Hannam, A., Sharma, A., & Curtis, T. (1999). Modeling of jaw biomechanics in the reconstructed mandibulectomy patient. *The Journal of prosthetic dentistry*, *81*(2), 167–173.

Dichard, A., & Klotch, D. W. (1994). Testing biomechanical strength of repairs for the mandibular angle fracture. *The Laryngoscope*, *104*(2), 201–208.

Dolgolev, A., Reshetov, I., Svyatoslavov, D., Sinelnikov, M., Kudrin, K., Dub, V., Put, V., & Anikin, V. (2020). Experimental biointegration of a titanium implant in delayed mandibular reconstruction. *Journal of personalized medicine*, *10*(1), 6.

Doty, J. M., Pienkowski, D., Goltz, M., Haug, R. H., Valentino, J., & Arosarena, O. A. (2004). Biomechanical evaluation of fixation techniques for bridging segmental mandibular defects. *Archives of Otolaryngology–Head & Neck Surgery*, *130*(12), 1388–1392.

Du, R., Su, Y.-X., Yan, Y., Choi, W. S., Yang, W.-F., Zhang, C., Chen, X., Curtin, J. P., Ouyang, J., & Zhang, B. (2020). A systematic approach for making 3d-printed patient-specific implants for craniomaxillofacial reconstruction. *Engineering*, *6*(11), 1291–1301.

Elaiwy, O., El Ansari, W., AlKhalil, M., & Ammar, A. (2020). Epidemiology and pathology of oral squamous cell carcinoma in a multi-ethnic population: Retrospective study of 154 cases over 7 years in qatar. *Annals of Medicine and Surgery*, *60*, 195–200.

Elias, C., Lima, J., Valiev, R., & Meyers, M. (2008). Biomedical applications of titanium and its alloys. *Jom*, *60*(3), 46–49.

Ettl, T., Driemel, O., Dresp, B. V., Reichert, T. E., Reuther, J., & Pistner, H. (2010). Feasibility of alloplastic mandibular reconstruction in patients following removal of oral squamous cell carcinoma. *Journal of Cranio-Maxillofacial Surgery*, *38*(5), 350–354.

Fontana, S. C., Smith, R. B., Nazir, N., & Andrews, B. T. (2016). Biomechanical assessment of fixation methods for segmental mandible reconstruction with fibula in the polyurethane model. *Microsurgery*, *36*(4), 330–333.

Gateno, J., Cookston, C., Hsu, S. S.-P., Stal, D. N., Durrani, S. K., Gold, J., Ismaily, S., Alexander, J. W., Noble, P. C., & Xia, J. J. (2013). Biomechanical evaluation of a new matrixmandible plating system on cadaver mandibles. *Journal of Oral and Maxillofacial Surgery*, *71*(11), 1900–1914.

Goh, B. T., Lee, S., Tideman, H., & Stoelinga, P. J. (2008). Mandibular reconstruction in adults: A review. *International journal of oral and maxillofacial surgery*, *37*(7), 597–605.

Goodyear, S. R., & Aspden, R. M. (2012). Mechanical properties of bone ex vivo. *Bone research protocols* (pp. 555–571). Springer.

Gröning, F., Fagan, M., & O'higgins, P. (2012). Modeling the human mandible under masticatory loads: Which input variables are important? *The Anatomical Record: Advances in Integrative Anatomy and Evolutionary Biology*, *295*(5), 853–863.

Gupta, D. K., van Keulen, F., & Langelaar, M. (2020). Design and analysis adaptivity in multiresolution topology optimization. *International Journal for Numerical Methods in Engineering*, *121*(3), 450–476.

Gutwald, R., Jaeger, R., & Lambers, F. M. (2017). Customized mandibular reconstruction plates improve mechanical performance in a mandibular reconstruction model. *Computer methods in BiomeChaniCs and BiomediCal engineering*, *20*(4), 426–435.

Haug, R. H., Barber, J. E., & Reifeis, R. (1996). A comparison of mandibular angle fracture plating techniques. *Oral Surgery, Oral Medicine, Oral Pathology, Oral Radiology, and Endodontology*, *82*(3), 257–263.

Haug, R. H., Fattahi, T. T., & Goltz, M. (2001). A biomechanical evaluation of mandibular angle fracture plating techniques. *Journal of oral and maxillofacial surgery*, *59*(10), 1199–1210.

Haug, R. H., Nuveen, E. J., Barber, J. E., & Storoe, W. (1998). An in vitro evaluation of distractors used for osteogenesis. *Oral Surgery, Oral Medicine, Oral Pathology, Oral Radiology, and Endodontology*, *86*(6), 648–659.

Henninger, H. B., Reese, S. P., Anderson, A. E., & Weiss, J. A. (2010). Validation of computational models in biomechanics. *Proceedings of the Institution of Mechanical Engineers, Part H: Journal of Engineering in Medicine*, *224*(7), 801–812.

Hölzle, F., Kesting, M., Hölzle, G., Watola, A., Loeffelbein, D., Ervens, J., & Wolff, K.-D. (2007). Clinical outcome and patient satisfaction after mandibular reconstruction with free fibula flaps. *International journal of oral and maxillofacial surgery*, *36*(9), 802–806.

Hudák, R., Schnitzer, M., Králová, Z. O., Gorejová, R., Mitrík, L., Rajťúková, V., Tóth, T., Kovačević, M., Rizničˇ, M., Oriňaková, R., et al. (2021). Additive manufacturing of porous ti6al4v alloy: Geometry analysis and mechanical properties testing. *Applied Sciences*, *11*(6), 2611.

Ilavarasi, P., & Anburajan, M. (2011). Design and finite element analysis of mandibular prosthesis. *2011 3rd International Conference on Electronics Computer Technology*, *3*, 325–329.

J&J. (n.d.). *Titanium 3d printed devices*. https://www.jnjmedicaldevices.com/en-EMEA/service-details/titanium-3d-printed-devices

Kakarala, K., Shnayder, Y., Tsue, T. T., & Girod, D. A. (2018). Mandibular reconstruction. *Oral oncology*, *77*, 111–117.

Kalfarentzos, E. F., Deligianni, D., Mitros, G., & Tyllianakis, M. (2009). Biomechanical evaluation of plating techniques for fixing mandibular angle fractures: The introduction of a new 3d plate approach. *Oral and maxillofacial surgery*, *13*(3), 139–144.

Khalifa, G. A., Abd El Moniem, N. A., Elsayed, S. A.-E., & Qadry, Y. (2016). Segmental mirroring: Does it eliminate the need for intraoperative readjustment of the virtually pre-bent reconstruction plates and is it economically valuable? *Journal of Oral and Maxillofacial Surgery*, *74*(3), 621–630.

Kinoshita, Y., Kobayashi, M., Hidaka, T., & Ikada, Y. (1997). Reconstruction of mandibular continuity defects in dogs using poly (l-lactide) mesh and autogenic particulate cancellous bone and marrow: Preliminary report. *Journal of oral and maxillofacial surgery*, *55*(7), 718–723.

Klotch, D. (1995). Application of reconstruction plates to the mandible. *Operative Techniques in Otolaryngology-Head and Neck Surgery*, *6*(2), 89–96.

Ko, C.-C., Rocha, E. P., & Larson, M. (2012). Past, present and future of finite element analysis in dentistry. *Biomedical Applications to Industrial Developments*, 1–25.

Kondo, S., Katsuta, H., Akizuki, A., Kurihara, Y., Kamatani, T., Yaso, A., Nagasaki, M., Shimane, T., Shirota, T., et al. (2015). Computer-assisted surgery for mandibular reconstruction using a patient-specific titanium mesh tray and particulate cancellous bone and marrow. *Case Reports in Clinical Medicine*, *4*(03), 85.

Koper, D. C., Leung, C. A., Smeets, L. C., Laeven, P. F., Tuijthof, G. J., & Kessler, P. A. (2021). Topology optimization of a mandibular reconstruction plate and biomechanical validation. *journal of the mechanical behavior of biomedical materials*, *113*, 104157.

Korioth, T., & Hannam, A. (1994). Deformation of the human mandible during simulated tooth clenching. *Journal of Dental Research*, *73*(1), 56–66.

Koschwanez, H., & Reichert, W. (2013). Textured and porous materials. *Biomaterials science* (pp. 321–331). Academic Press.

Kumar, B. P., Venkatesh, V., Kumar, K. J., Yadav, B. Y., & Mohan, S. R. (2016). Mandibular reconstruction: Overview. *Journal of maxillofacial and oral surgery*, *15*(4), 425–441.

Lee, S., Goh, B., Tideman, H., & Stoelinga, P. (2008). Modular endoprosthesis for mandibular reconstruction: A preliminary animal study. *International journal of oral and maxillofacial surgery*, *37*(10), 935–942.

Lee, W.-b., Choi, W.-h., Lee, H.-g., Choi, N.-r., Hwang, D.-s., & Kim, U.-k. (2018). Mandibular reconstruction with a ready-made type and a custom-made type titanium mesh after mandibular resection in patients with oral cancer. *Maxillofacial plastic and reconstructive surgery*, *40*(1), 1–7.

Lee, Y., & Welsch, G. (1990). Young's modulus and damping of ti□ 6al□ 4v alloy as a function of heat treatment and oxygen concentration. *Materials Science and Engineering: A*, *128*(1), 77–89.

Lee, Y.-W., You, H.-J., Jung, J.-A., & Kim, D.-W. (2018). Mandibular reconstruction using customized three-dimensional titanium implant. *Archives of craniofacial surgery*, *19*(2), 152.

Leitz, K.-H., Singer, P., Plankensteiner, A., Tabernig, B., Kestler, H., & Sigl, L. (2017). Multi-physical simulation of selective laser melting. *Metal Powder Report*, *72*(5), 331–338.

León, D. N., Flórez, G. M., & Gualdrón, C. L. (2020). Low-cost mandibular reconstruction workflow. *Oral and Maxillofacial Surgery Cases*, *6*(2), 100146.

Li, C.-H., Wu, C.-H., & Lin, C.-L. (2020). Design of a patient-specific mandible reconstruction implant with dental prosthesis for metal 3d printing using integrated weighted topology optimization and finite element analysis. *Journal of the mechanical behavior of biomedical materials*, *105*, 103700.

Li, P., Shen, L., Li, J., Liang, R., Tian, W., & Tang, W. (2014). Optimal design of an individual endoprosthesis for the reconstruction of extensive mandibular defects with finite element analysis. *Journal of Cranio-Maxillofacial Surgery*, *42*(1), 73–78.

Liu, S.-P., Cai, Z.-G., Zhang, J., Zhang, J.-G., & Zhang, Y. (2016). Stability and complications of miniplates for mandibular reconstruction with a fibular graft: Outcomes for 544 patients. *British Journal of Oral and Maxillofacial Surgery*, *54*(5), 496–500.

Liu, S., & Shin, Y. C. (2019). Additive manufacturing of ti6al4v alloy: A review. *Materials & Design*, *164*, 107552.

Liu, Y.-f., Fan, Y.-y., Jiang, X.-f., & Baur, D. A. (2017). A customized fixation plate with novel structure designed by topological optimization for mandibular angle fracture based on finite element analysis. *Biomedical engineering online*, *16*(1), 1–17.

Liu, Y.-f., Zhu, F.-d., Dong, X.-t., & Peng, W. (2011). Digital design of scaffold for mandibular defect repair based on tissue engineering. *Journal of Zhejiang University Science B*, *12*(9), 769–779.

Louis, P., Holmes, J., & Fernandes, R. (2004). Resorbable mesh as a containment system in reconstruction of the atrophic mandible fracture. *Journal of oral and maxillofacial surgery*, *62*(6), 719–723.

Maconachie, T., Leary, M., Lozanovski, B., Zhang, X., Qian, M., Faruque, O., & Brandt, M. (2019). Slm lattice structures: Properties, performance, applications and challenges. *Materials & Design*, *183*, 108137.

Madsen, M. J., McDaniel, C. A., & Haug, R. H. (2008). A biomechanical evaluation of plating techniques used for reconstructing mandibular symphysis/parasymphysis fractures. *Journal of oral and maxillofacial surgery*, *66*(10), 2012–2019.

Malekpour, Z., Sarkarat, F., & Hooshangi, H. (2014). Mandibular reconstruction using custom-made titanium mesh tray and autogenous bone graft: A case report. *Thrita*, *3*(4).

Marchetti, C., Bianchi, A., Mazzoni, S., Cipriani, R., & Campobassi, A. (2006). Oromandibular reconstruction using a fibula osteocutaneous free flap: Four different “preplating” techniques. *Plastic and reconstructive surgery*, *118*(3), 643–651.

Marinescu, R., Daegling, D. J., & Rapoff, A. J. (2005). Finite-element modeling of the anthropoid mandible: The effects of altered boundary conditions. *The Anatomical Record Part A: Discoveries in Molecular, Cellular, and Evolutionary Biology: An Official Publication of the American Association of Anatomists*, *283*(2), 300–309.

Markwardt, J., Pfeifer, G., Eckelt, U., & Reitemeier, B. (2007). Analysis of complications after reconstruction of bone defects involving complete mandibular resection using finite element modelling. *Oncology Research and Treatment*, *30*(3), 121–126.

Martola, M., Lindqvist, C., Hänninen, H., & Al-Sukhun, J. (2007). Fracture of titanium plates used for mandibular reconstruction following ablative tumor surgery. *Journal of Biomedical Materials Research Part B: Applied Biomaterials: An Official Journal of The Society for Biomaterials, The Japanese Society for Biomaterials, and The Australian Society for Biomaterials and the Korean Society for Biomaterials*, *80*(2), 345–352.

Marunick, M., Mathes, B., & Klein, B. (1992). Masticatory function in hemimandibulectomy patients. *Journal of oral rehabilitation*, *19*(3), 289–295.

Marx, R. E. (2007). Bone and bone graft healing. *Oral and maxillofacial surgery clinics of North America*, *19*(4), 455–466.

Mehta, S., & Kuriakose, M. A. (2021). Principles of surgical management of oral cancer. *Oral and maxillofacial surgery for the clinician* (pp. 1869–1891). Springer.

Meng, L., Zhang, W., Quan, D., Shi, G., Tang, L., Hou, Y., Breitkopf, P., Zhu, J., & Gao, T. (2020). From topology optimization design to additive manufacturing: Today’s success and tomorrow’s roadmap. *Archives of Computational Methods in Engineering*, *27*(3), 805–830.

Merema, B. B. J., Kraeima, J., Glas, H. H., Spijkervet, F. K., & Witjes, M. J. (2021). Patient-specific finite element models of the human mandible: Lack of consensus on current set-ups. *Oral diseases*, *27*(1), 42–51.

Moghaddam, N. S., Jahadakbar, A., Amerinatanzi, A., Elahinia, M., Miller, M., & Dean, D. (2016). Metallic fixation of mandibular segmental defects: Graft immobilization and orofacial functional maintenance. *Plastic and Reconstructive Surgery Global Open*, *4*(9).

Moiduddin, K., Anwar, S., Ahmed, N., Ashfaq, M., & Al-Ahmari, A. (2017). Computer assisted design and analysis of customized porous plate for mandibular reconstruction. *Irbm*, *38*(2), 78–89.

Moiduddin, K., Al-Ahmari, A., Nasr, E. S. A., Al Kindi, M., Ramalingam, S., & Kamrani, A. (2016). Comparing 3-dimensional virtual reconstruction methods in customized implants. *International Journal of Advanced Biotechnology and Research*, *7*(1), 323–331.

Moiduddin, K., Mian, S. H., Ahmed, N., Ameen, W., Al-Khalefah, H., khan Mohammed, M., & Umer, U. (2020). Integrative and multi-disciplinary framework for the 3d rehabilitation of large mandibular defects. *The International Journal of Advanced Manufacturing Technology*, *106*(9), 3831–3847.

Moiduddin, K., Mian, S. H., Alkhalefah, H., & Umer, U. (2019). Digital design, analysis and 3d printing of prosthesis scaffolds for mandibular reconstruction. *Metals*, *9*(5), 569.

Momoh, A. O., Yu, P., Skoracki, R. J., Liu, S., Feng, L., & Hanasono, M. M. (2011). A prospective cohort study of fibula free flap donor-site morbidity in 157 consecutive patients. *Plastic and reconstructive surgery*, *128*(3), 714–720.

Mounir, M., Abou-ElFetouh, A., ElBeialy, W., & Mounir, R. (2020). Patient-specific alloplastic endoprosthesis for reconstruction of the mandible following segmental resection: A case series. *Journal of Cranio-Maxillofacial Surgery*, *48*(8), 719–723.

Munir, K. S., Li, Y., & Wen, C. (2017). Metallic scaffolds manufactured by selective laser melting for biomedical applications. *Metallic foam bone* (pp. 1–23). Elsevier.

Naros, A., Weise, H., Tilsen, F., Hoefert, S., Naros, G., Krimmel, M., Reinert, S., & Polligkeit, J. (2018). Three-dimensional accuracy of mandibular reconstruction by patient-specific pre-bent reconstruction plates using an “in-house” 3d-printer. *Journal of Cranio-Maxillofacial Surgery*, *46*(9), 1645–1651.

Nasr, E. A., Al-Ahmari, A. M., Moiduddin, K., Al Kindi, M., & Kamrani, A. K. (2017). A digital design methodology for surgical planning and fabrication of customized mandible implants. *Rapid Prototyping Journal*.

Nelms, L., & Palmer, W. J. (2019). Tissue engineering in mandibular reconstruction: Osteogenesis-inducing scaffolds. *Plastic and Aesthetic Research*, *6*.

Palanca, M., Tozzi, G., & Cristofolini, L. (2016). The use of digital image correlation in the biomechanical area: A review. *International biomechanics*, *3*(1), 1–21.

Paré, A., Bossard, A., Laure, B., Weiss, P., Gauthier, O., & Corre, P. (2019). Reconstruction of segmental mandibular defects: Current procedures and perspectives. *Laryngoscope investigative otolaryngology*, *4*(6), 587–596.

Park, J.-H., Odkhuu, M., Cho, S., Li, J., Park, B.-Y., & Kim, J.-W. (2020). 3d-printed titanium implant with pre-mounted dental implants for mandible reconstruction: A case report. *Maxillofacial Plastic and Reconstructive Surgery*, *42*(1), 1–4.

Patton, K., & Thibodeau, G. (2012). *Anatomy & physiology*. Mosby.

Pelleg, J. (2020). *Additive and traditionally manufactured components: A comparative analysis of mechanical properties*. Additive Manufacturing Materia.

Peng, W.-m., Cheng, K.-j., Liu, Y.-f., Nizza, M., Baur, D. A., Jiang, X.-f., & Dong, X.-t. (2021). Biomechanical and mechanostat analysis of a titanium layered porous implant for mandibular reconstruction: The effect of the topology optimization design. *Materials Science and Engineering: C*, *124*, 112056.

Petrovic, I. D., Migliacci, J., Ganly, I., Patel, S., Xu, B., Ghossein, R., Huryn, J., & Shah, J. (2018). Ameloblastomas of the mandible and maxilla. *Ear, nose, & throat journal*, *97*(7), E26.

Pinheiro, M., & Alves, J. (2015). The feasibility of a custom-made endoprosthesis in mandibular reconstruction: Implant design and finite element analysis. *Journal of Cranio-Maxillofacial Surgery*, *43*(10), 2116–2128.

Poelert, S., Valstar, E., Weinans, H., & Zadpoor, A. A. (2013). Patient-specific finite element modeling of bones. *Proceedings of the Institution of Mechanical Engineers, Part H: Journal of Engineering in Medicine*, *227*(4), 464–478.

Pradhan, R., Rahman, S., Qureshi, A., & Ullah, A. (2021). Biopolymers: Opportunities and challenges for 3d printing. *Biopolymers and their Industrial Applications*, 281–303.

Qassemyar, Q., Assouly, N., Temam, S., & Kolb, F. (2017). Use of a three-dimensional custom-made porous titanium prosthesis for mandibular body reconstruction. *International journal of oral and maxillofacial surgery*, *46*(10), 1248–1251.

Rachmiel, A., Shilo, D., Blanc, O., & Emodi, O. (2017). Reconstruction of complex mandibular defects using integrated dental custom-made titanium implants. *British Journal of Oral and Maxillofacial Surgery*, *55*(4), 425–427.

Radwan, D., & Mobarak, F. (2018). Plate-related complications after mandibular reconstruction: Observational study osteotomy. *Egyptian Journal of Oral and Maxillofacial Surgery*, *9*(1), 22–27.

Rankin, K., Browne, M., & Dickinson, A. (2017). Digital image correlation for strain analysis of whole bones and implants. *Experimental methods in orthopaedic biomechanics* (pp. 65–83). Elsevier.

Rendenbach, C., Sellenschloh, K., Gerbig, L., Morlock, M. M., Beck-Broichsitter, B., Smeets, R., Heiland, M., Huber, G., & Hanken, H. (2017). Cad–cam plates versus conventional fixation plates for primary mandibular reconstruction: A biomechanical in vitro analysis. *Journal of Cranio-Maxillofacial Surgery*, *45*(11), 1878–1883.

Safi, Y., Hohenberger, S., Robbenmenke, C., Banki, F., Lethaus, B., Kessler, P., Schmitz-Rode, T., & Steinseifer, U. (2010). Investigation of the failure behavior of a cranial implant-skull model under different load conditions using fem. *SIMULIA Customer Conference*, 1–16.

Schouman, T., Schmitt, M., Adam, C., Dubois, G., & Rouch, P. (2016). Influence of the overall stiffness of a load-bearing porous titanium implant on bone ingrowth in critical-size mandibular bone defects in sheep. *Journal of the mechanical behavior of biomedical materials*, *59*, 484–496.

Schupp, W., Arzdorf, M., Linke, B., & Gutwald, R. (2007). Biomechanical testing of different osteosynthesis systems for segmental resection of the mandible. *Journal of oral and maxillofacial surgery*, *65*(5), 924–930.

Seebach, M., Theurer, F., Foehr, P., von Deimling, C., Burgkart, R., & Zaeh, M. F. (2017). Design of bone plates for mandibular reconstruction using topology and shape optimization. *World Congress of Structural and Multidisciplinary Optimisation*, 2086–2096.

Seol, G.-J., Jeon, E.-G., Lee, J.-S., Choi, S.-Y., Kim, J.-W., Kwon, T.-G., & Paeng, J.-Y. (2014). Reconstruction plates used in the surgery for mandibular discontinuity defect. *Journal of the Korean Association of Oral and Maxillofacial Surgeons*, *40*(6), 266–271.

Sercombe, T., Zhang, L.-C., Li, S., & Hao, Y. (2018). Additive manufacturing of cp-ti, ti-6al-4v and ti2448. *Titanium in medical and dental applications* (pp. 303–324). Elsevier.

Shibahara, T., Noma, H., Furuya, Y., & Takaki, R. (2002). Fracture of mandibular reconstruction plates used after tumor resection. *Journal of oral and maxillofacial surgery*, *60*(2), 182–185.

Shim, V., Boheme, J., Josten, C., & Anderson, I. (2012). Use of polyurethane foam in orthopaedic biomechanical experimentation and simulation. *Polyurethane*, 171–200.

SLM Solutions®. (n.d.). *Material data sheet*. https://www.slm-solutions.com/fileadmin/Content/Powder/MDS/MDS_Ti-Alloy_Ti6Al4V__ELI_0719_EN.pdf

Smith, J. (2021). *Mandibular plating: Overview, preoperative evaluations and considerations, hardware and techniques*. https://emedicine.medscape.com/article/881542-overview

Sproll, C. K., Holtmann, H., Schorn, L. K., Jansen, T. M., Reifenberger, J., Boeck, I., Rana, M., Kübler, N. R., & Lommen, J. (2020). Mandible handling in the surgical treatment of oral squamous cell carcinoma: Lessons from clinical results after marginal and segmental mandibulectomy. *Oral surgery, oral medicine, oral pathology and oral radiology*, *129*(6), 556–564.

Szucs, A., Bujtár, P., Sándor, G., & Barabás, J. (2010). Finite element analysis of the human mandible to assess the effect of removing an impacted third molar. *Journal (Canadian Dental Association)*, *76*, a72–a72.

Taqi, M., & Raju, S. (2020). Fibula free flaps. *StatPearls [Internet]*.

Tideman, H., & Lee, S. (2006). The tl endoprosthesis for mandibular reconstruction-a metallic yet biological approach. *Asian J Oral Maxfac Surg*, *18*(5).

Tideman, H., Samman, N., & Cheung, L. (1998). Functional reconstruction of the mandible: A modified titanium mesh system. *International journal of oral and maxillofacial surgery*, *27*(5), 339–345.

Tohka, J. (2014). Partial volume effect modeling for segmentation and tissue classification of brain magnetic resonance images: A review. *World journal of radiology*, *6*(11), 855.

Trainotti, S., Raith, S., Kesting, M., Eichhorn, S., Bauer, F., Kolk, A., Lethaus, B., Hölzle, F., & Steiner, T. (2014). Locking versus nonlocking plates in mandibular reconstruction with fibular graft—a biomechanical ex vivo study. *Clinical oral investigations*, *18*(4), 1291–1298.

Tümer, N., Vuurberg, G., Blankevoort, L., Kerkhoffs, G. M. M., Tuijthof, G. J., & Zadpoor, A. A. (2019). Typical shape differences in the subtalar joint bones between subjects with chronic ankle instability and controls. *Journal of Orthopaedic Research®*, *37*(9), 1892–1902.

Urken, M. L., Weinberg, H., Vickery, C., Buchbinder, D., Lawson, W., & Biller, H. F. (1991). Oromandibular reconstruction using microvascular composite free flaps: Report of 71 cases and a new classification scheme for bony, soft-tissue, and neurologic defects. *Archives of Otolaryngology–Head & Neck Surgery*, *117*(7), 733–744.

Van Eijden, T. (2000). Biomechanics of the mandible. *Critical reviews in oral biology & medicine*, *11*(1), 123–136.

van Baar, G. J., Forouzanfar, T., Liberton, N. P., Winters, H. A., & Leusink, F. K. (2018). Accuracy of computer-assisted surgery in mandibular reconstruction: A systematic review. *Oral oncology*, *84*, 52–60.

Vignesh, U., Mehrotra, D., Howlader, D., Singh, P. K., Gupta, S., et al. (2019). Patient specific three-dimensional implant for reconstruction of complex mandibular defect. *Journal of Craniofacial Surgery*, *30*(4), e308–e311.

Vollmer, D., Meyer, U., Joos, U., Vegh, A., & Piffko, J. (2000). Experimental and finite element study of a human mandible. *Journal of Cranio-Maxillofacial Surgery*, *28*(2), 91–96.

Wang, Y., Zhang, H., Fan, S., Zhang, D., Huang, Z., Chen, W., Ye, J., & Li, J. (2016). Mandibular reconstruction with the vascularized fibula flap: Comparison of virtual planning surgery and conventional surgery. *International journal of oral and maxillofacial surgery*, *45*(11), 1400–1405.

Wang, Z., Wang, C., Li, C., Qin, Y., Zhong, L., Chen, B., Li, Z., Liu, H., Chang, F., & Wang, J. (2017). Analysis of factors influencing bone ingrowth into three-dimensional printed porous metal scaffolds: A review. *Journal of Alloys and Compounds*, *717*, 271–285.

Wilde, F., Cornelius, C.-P., & Schramm, A. (2014). Computer-assisted mandibular reconstruction using a patient-specific reconstruction plate fabricated with computer-aided design and manufacturing techniques. *Craniomaxillofacial trauma & reconstruction*, *7*(2), 158–166.

Wong, C., Loh, J. S., & Islam, I. (2016). The role of finite element analysis in studying potential failure of mandibular reconstruction methods. *Perusal Finite Elem. Method*, 189–210.

Wong, R. C., Tideman, H., Merkx, M., Jansen, J., Goh, S., & Liao, K. (2011). Review of biomechanical models used in studying the biomechanics of reconstructed mandibles. *International Journal of Oral and Maxillofacial Surgery*, *40*(4), 393–400.

Wong, R. C., Tideman, H., Merkx, M. A., Jansen, J., & Goh, S. M. (2012a). The modular endoprosthesis for mandibular body replacement. part 1: Mechanical testing of the reconstruction. *Journal of Cranio-Maxillofacial Surgery*, *40*(8), e479–e486.

Wong, R. C., Tideman, H., Merkx, M. A., Jansen, J., & Goh, S. M. (2012b). The modular endoprosthesis for mandibular body replacement. part 2: Finite element analysis of endoprosthesis reconstruction of the mandible. *Journal of Cranio-Maxillofacial Surgery*, *40*(8), e487–e497.

Wu, C.-H., Lin, Y.-S., Liu, Y.-S., & Lin, C.-L. (2017). Biomechanical evaluation of a novel hybrid reconstruction plate for mandible segmental defects: A finite element analysis and fatigue testing. *Journal of Cranio-Maxillofacial Surgery*, *45*(10), 1671–1680.

Yamashita, Y., Yamaguchi, Y., Tsuji, M., Shigematsu, M., & Goto, M. (2008). Mandibular reconstruction using autologous iliac bone and titanium mesh reinforced by laser welding for implant placement. *International Journal of Oral & Maxillofacial Implants*, *23*(6).

Yan, C., Hao, L., Hussein, A., & Young, P. (2015). Ti–6al–4v triply periodic minimal surface structures for bone implants fabricated via selective laser melting. *Journal of the mechanical behavior of biomedical materials*, *51*, 61–73.

Yi, Z., Jian-Guo, Z., Guang-Yan, Y., Ling, L., Fu-Yun, Z., & Guo-Cheng, Z. (1999). Reconstruction plates to bridge mandibular defects: A clinical and experimental investigation in bimomechanical aspects. *International Journal of Oral & Maxillofacial Surgery*, *28*(6), 445–450.

Zadpoor, A. A. (2015). Bone tissue regeneration: The role of scaffold geometry. *Biomaterials science*, *3*(2), 231–245.

Zhang, Y., Wu, L., Guo, X., Kane, S., Deng, Y., Jung, Y.-G., Lee, J.-H., & Zhang, J. (2018). Additive manufacturing of metallic materials: A review. *Journal of Materials Engineering and Performance*, *27*(1), 1–13.

Zhou, L.-b., Shang, H.-t., He, L.-s., Bo, B., Liu, G.-c., Liu, Y.-p., & Zhao, J.-l. (2010). Accurate reconstruction of discontinuous mandible using a reverse engineering/computer-aided design/rapid prototyping technique: A preliminary clinical study. *Journal of Oral and Maxillofacial Surgery*, *68*(9), 2115–2121.

Zienkiewicz, O. C., Taylor, R. L., & Zhu, J. Z. (2005). *The finite element method: Its basis and fundamentals*. Elsevier.

Appendices

A

Mimics image processing workflow

The first step will be to load the DICOM image dataset into Mimics. Then, thresholding will be applied to segment the mandible bone out of the images (Figure A.1-a). The user is provided with the option to adjust the threshold values as desired. Normally, that is in case of patient data, the predefined threshold set will be set at “Bone (CT)” which may already produce correct threshold boundaries. However, since this research uses a synthetic mandible model, different minimum and maximum values for the thresholding need to be applied (Figure A.1-b). After the thresholding process, the user is provided with the option to use the region grow tool to get rid of extraneous (noise) structures around the mandible (Figure A.1-c). The user is therefor asked to indicate a starting point on the mask (Figure A.1-d). Afterwards, the user is provided with the options to continue with the current mask, adjust the thresholds again, or to edit the mask using to cut away structures by hand using the Edit Masks tool (Figure A.1-e). After either of these options, a 3D part will be calculated from the final mask, which will be presented to the user for a final check (Figure A.1-f). The user can choose to edit the mask again by adjusting the thresholds, or to directly export the part to 3-Matic where the script will continue to run.

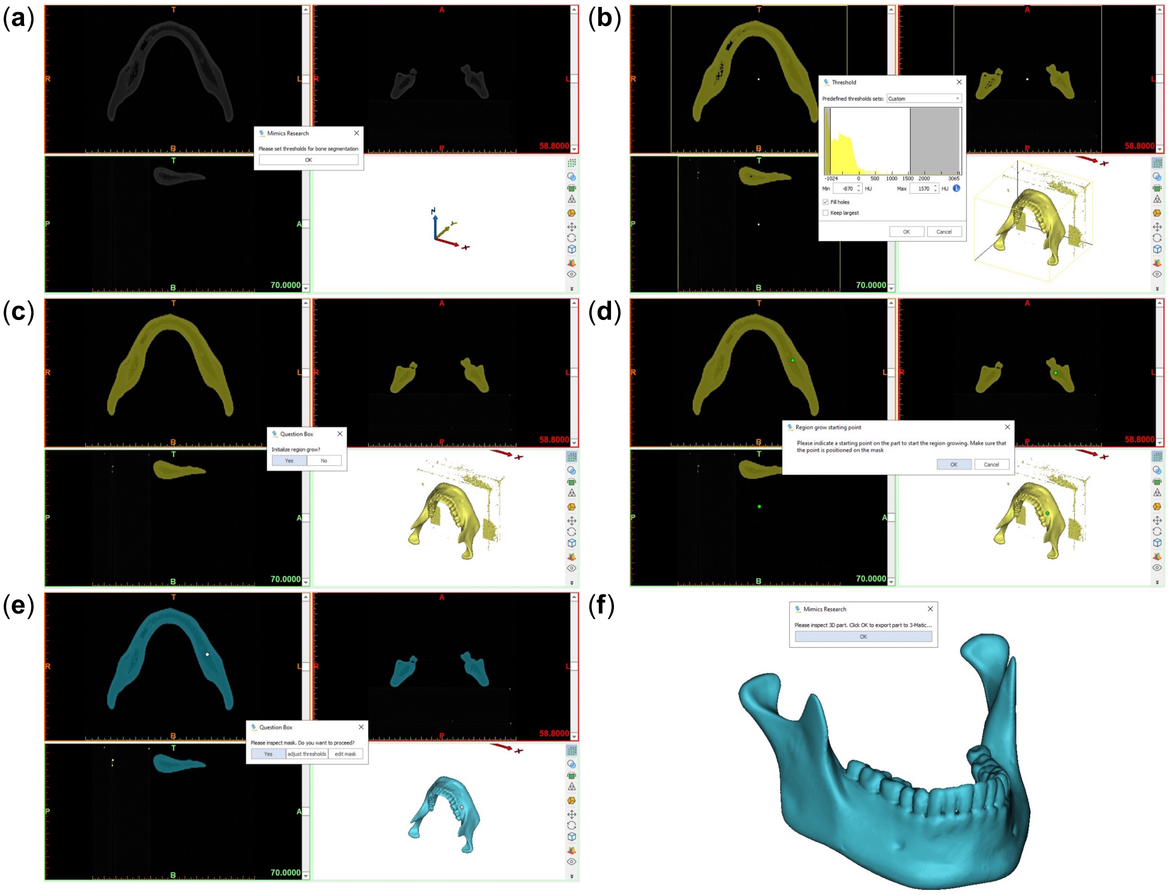

Mimics Research

Please set thresholds for bone segmentation

Predefined thresholds sets: Custom

Min -870 HU Max 1570 HU

☑ Fill holes

☐ Keep largest

Initialize region grow?

Please indicate a starting point on the part to start the region growing. Make sure that the point is positioned on the mask

Please inspect mask. Do you want to proceed?

Please inspect 3D part. Click OK to export part to 3-Matic...

Figure A.1. Image processing steps in Mimics.

B

3-Matic design workflow

After completion of the image processing steps, the virtual 3D mandible model is exported to 3-Matic where the script continues to run. The design workflow in 3-Matic comprises 7 steps, including (1) segmental resection, (2) segmental mirroring, (3) missing shape estimation, (4) implant surface definition, (5) screw type and positioning and (6) meshing. The dialogue screens providing instructions to the user are not included in the images of the design steps shown below. However, pop-up menus in which the user is required to choose from a list of options or type in a specific value are included.

Design Step 1 – segmental resection

Define the two cutting planes by creating two datum planes. The user will indicate three points on the mandible surface through which the datum planes will be generated (Figure B.1-a). After creating each datum planes, the user can finetune the orientation of the plane by translating or rotating it (Figure B.1-b). A cutting operation is used to perform the segmental resection along the created datum planes (Figure B.1-c).

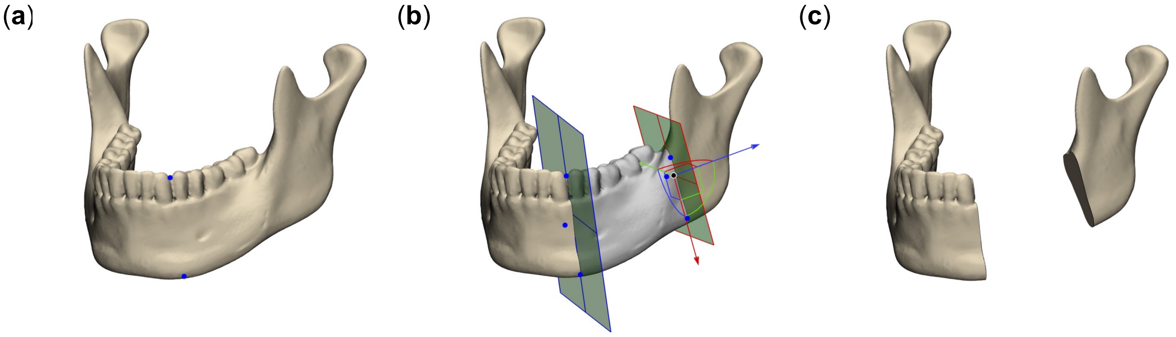

Figure B.1. Segmental resection steps in 3-Matic.

Design Step 2 – segmental mirroring

Ask user to select two points, one on each condylar or coronoid process, in between which the mid-sagittal (datum) cutting plane will be created (Figure B.2-a). The position and orientation of the plane can be finetuned after creating it (Figure B.2-b). Copy and mirror the healthy side of the mandible over the affected side across the mid-sagittal datum plane. Finetune the position of the mirrored segment (red colored) such that that it aligns best with the affected side of the mandible (Figure B.2-c). Cut the mirrored segment using the cutting planes created in Design step 1 and keep only the middle segment that fits the gap in the affected side of the mandible.

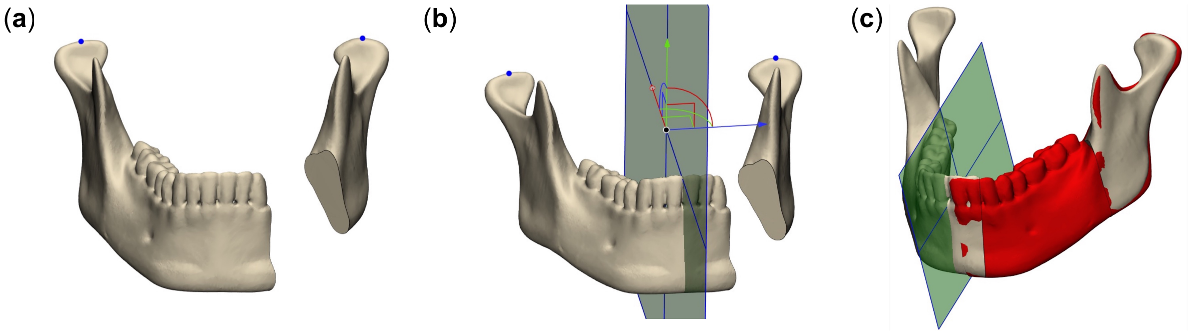

Figure B.2. Segmental mirroring steps in 3-Matic.

Design Step 3 – missing shape estimation

If teeth are present, remove them first by using the 'trim' function (Figure B.3-a), followed by 'fillet' of the remaining contour to get smooth borders (Figure B.3-b). Ask user to select 6 points lying in one plane around the bridging part. This operation will be performed on the bridging part 3 times; first about 1 cm away from one end, one in the middle and finally about 1 cm away from the other end (Figure B.3-c). Curves will be created between the points that will serve as intermediate contour profiles for the sweeping operation. Ask user to select two points, one in approximately the middle of the flat surface on each bony end (Figure B.3-d and B.3-e). A curve will be created between these two points that will serve as a path for the sweeping operation. Perform a sweep-loft operation using the previously created curves as sweep path and intermediate profiles. Perform a Boolean union on the three separate parts and complete the shape estimation with the filter small surfaces, wrapping and smoothing operations to end up with a smooth reconstruction (Figure B.3-f).

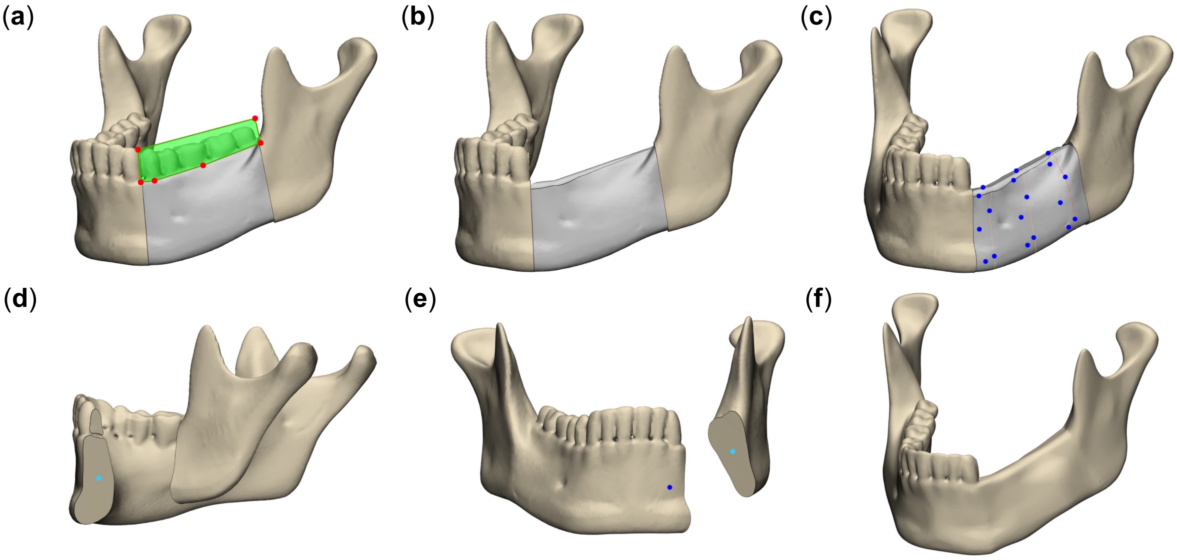

Figure B.3. Shape estimation steps in 3-Matic.

Design Step 4 – implant surface definition

Ask user to mark the surface of the mandible to define the desired implant region (Figure B.4-a). Smooth the marking borders to get a cleaner surface area (Figure B.4-b) and copy the implant surface to a new part. A pop-up window is being displayed asking the user to start the implant thickness processing (Figure B.4-c). The user is asked to enter the desired implant thickness (Figure B.4-d). The solid implant is shown (Figure B.4-e). The user is asked to check the implant and is given instructions to trim off any protrusions or unwanted areas.

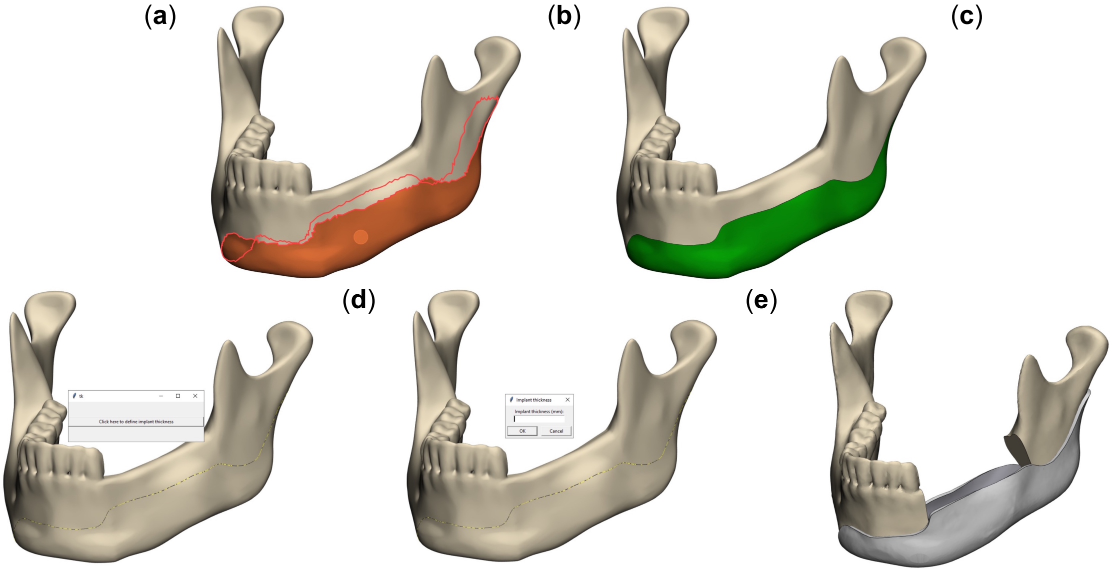

Figure B.4. Implant surface definition steps in 3-Matic.

Design Step 5 – screw type and positioning

First of all, the user is asked to select two points on the anterior mandibular segment, one on the lateral side and one on the medial side, to measure the distance between both points as an estimation for the screw length. This procedure will be repeated for the posterior mandibular segment. Next, a pop-up window is being displayed asking the user to start the MatrixMANDIBLE screw type process for the anterior side of the remaining mandible (Figure B.5-a). A second pop-up window is being displayed asking the user to enter the length of the screws (Figure B.5-b). A third pop-up window is being displayed asking the user to select the desired screw diameter (Figure B.5-c). A fourth pop-up window is being displayed asking the user to start the screw positioning process in the anterior region (Figure B.5-d). A sixth pop-up window is being displayed asking the user to select the desired number of screws (Figure B.5-e). Then, the user is asked to position the specified number of screws one by one by clicking on the implant. After clicking, a screw hole is automatically created corresponding to the screw size chosen earlier (Figure B.5-f). A countersink hole is automatically created at the end of the screw hole to make sure that the screw head lies flat with the surface of the mandible. Steps A through F are repeated for the posterior region (Figure B.5-g). Holes are also automatically created in the mandible with lengths corresponding to the screw lengths specified by the user (Figure B.5-h). The final design will be shown (Figure B.5-i).

Design Step 6 – meshing

A new surface and volume mesh will automatically be created for both mandibular segments, as well as the implant. For all three parts, a quality preserving reduce triangles meshing operation is first applied, followed by an adaptive remesh (Figure B.6-a). Maximum triangle edge lengths of the mesh applied to the mandibular bone and implant are 2.0 and 1.0, respectively. The screw hole surfaces will be remeshed with a higher element density, based on expected high levels of stress in these regions. 4-node tetrahedral volume meshes will be created with maximum edge lengths of 1.5 and 1.0 for the mandible and implant, respectively. (Figure B.6-b). After meshing, the user is asked to copy the three parts, close 3-Matic and paste the parts into Mimics for material assignment.

After finishing the design process of the implant, the implant and mandible parts will be imported back into Mimics for material assignment. First, the outer surface pixels of the mask will be removed using the Erode operation with 8-connectivity to prevent partial volume artefacts. Then, the meshes will be assigned with materials that are stored in a lookup file. Lastly, the meshes are exported in a single .inp file that is compatible with the Abaqus FEA software.

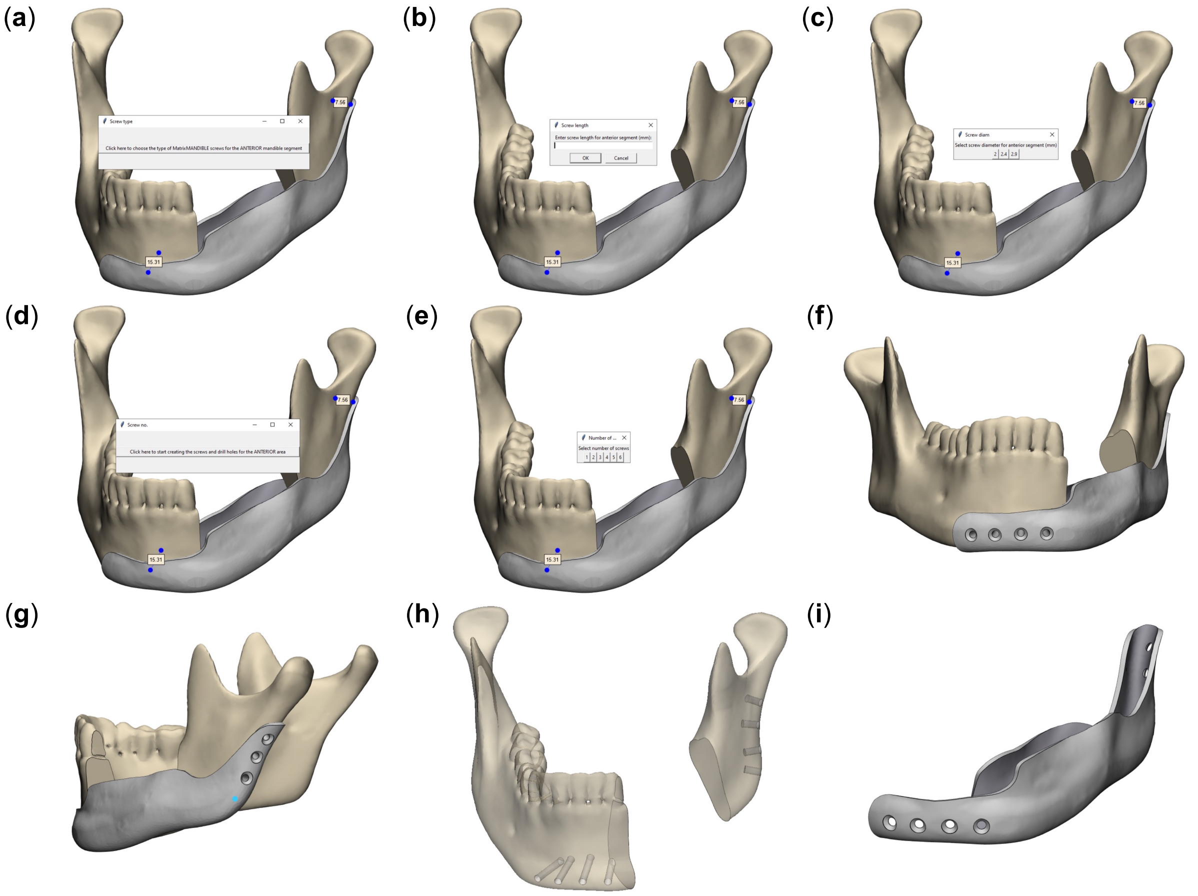

Click here to choose the type of MatrixMANDIBLE screws for the ANTERIOR mandible segment

Enter screw length for anterior segment (mm):

Select screw diameter for anterior segment (mm)

Click here to start creating the screws and drill holes for the ANTERIOR area

Select number of screws

Figure B.5. Screw type and positioning steps in 3-Matic.

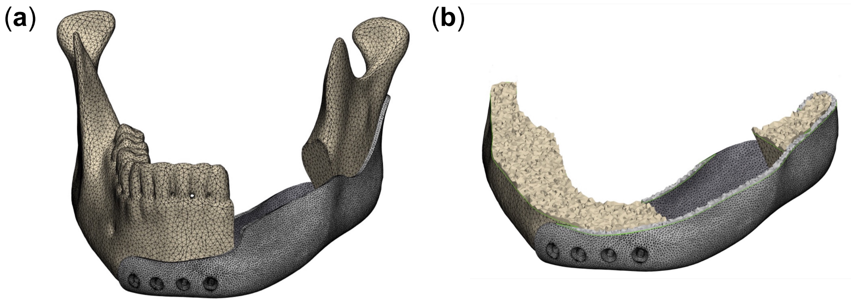

Figure B.6. Meshing steps in 3-Matic.

C

Cyclic testing results

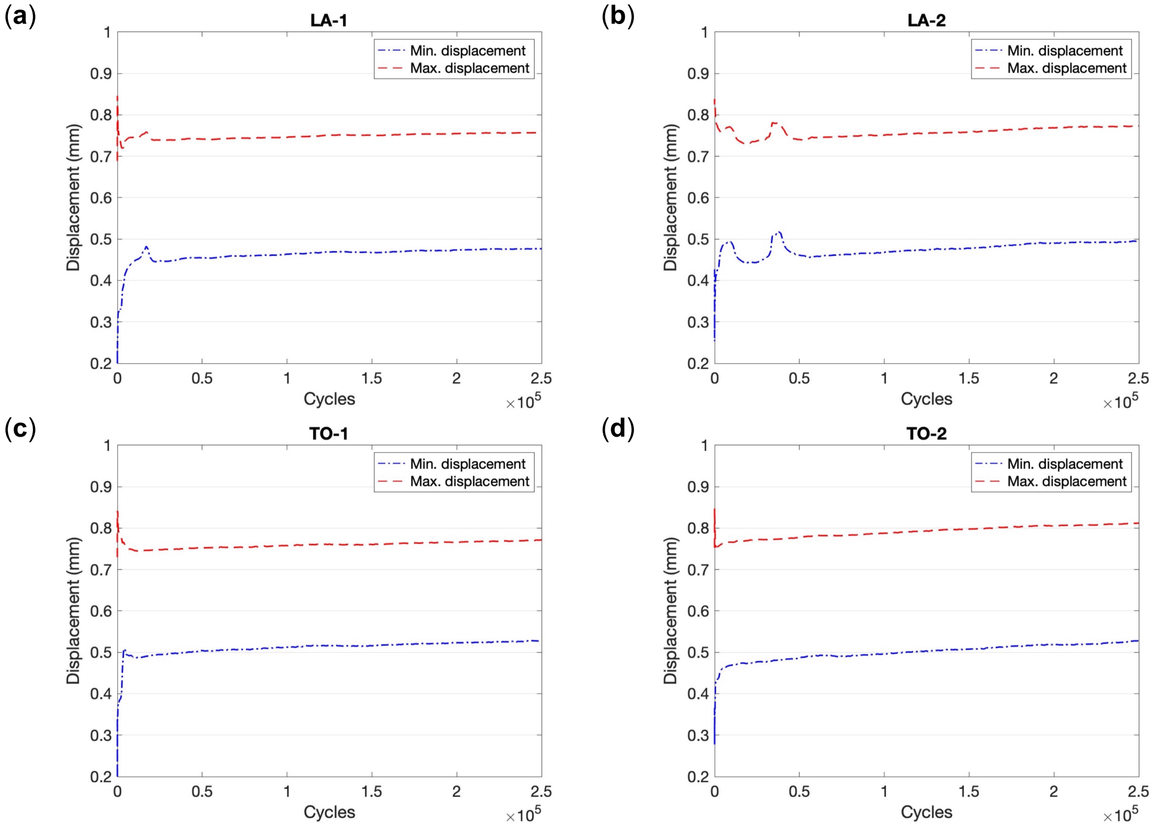

Figure C.1. Minimum and maximum displacement versus the number of cycles of each specimen with (**a**, **b**) lattice implants, and (**c**, **d**) TO implants during cyclic testing according to constant-cyclic-method.

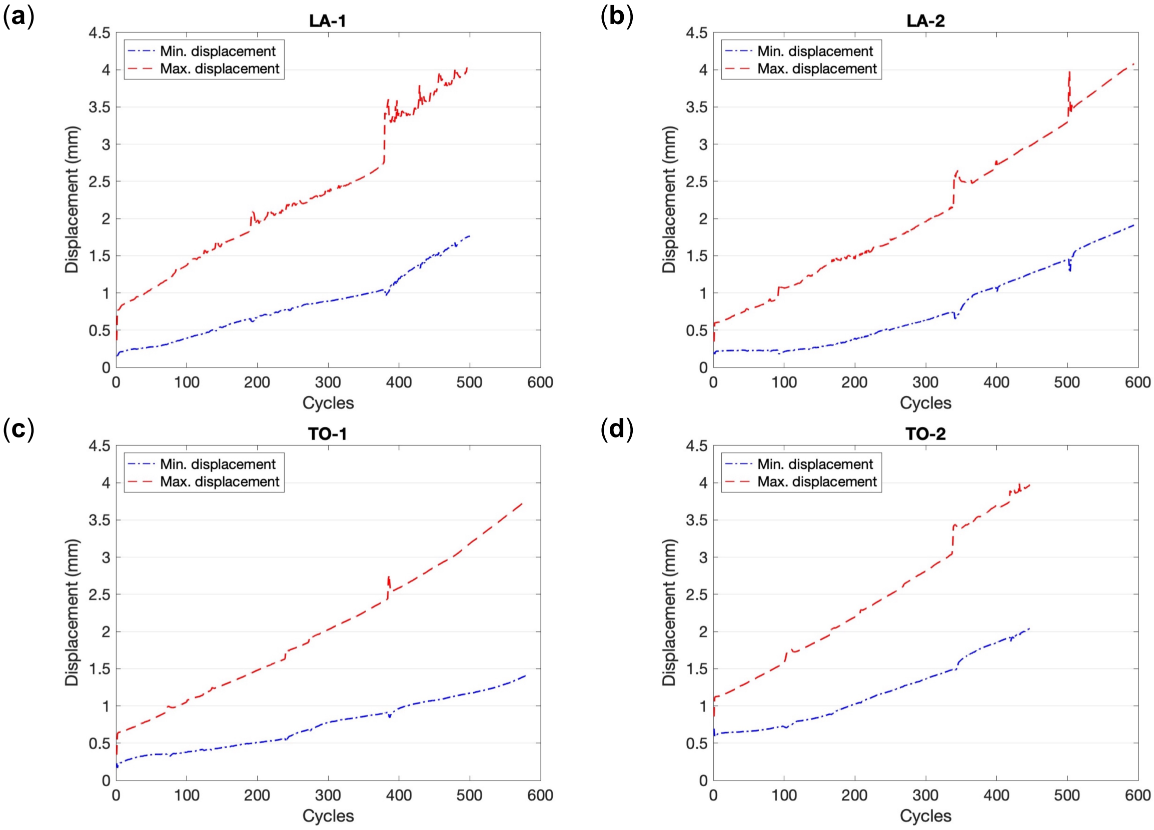

Figure C.2. Minimum and maximum displacement versus the number of cycles of each specimen with (**a**, **b**) lattice implants, and (**c**, **d**) TO implants during cyclic testing according to increment-cyclic-method.

D

Experimental setup technical drawings

See next pages

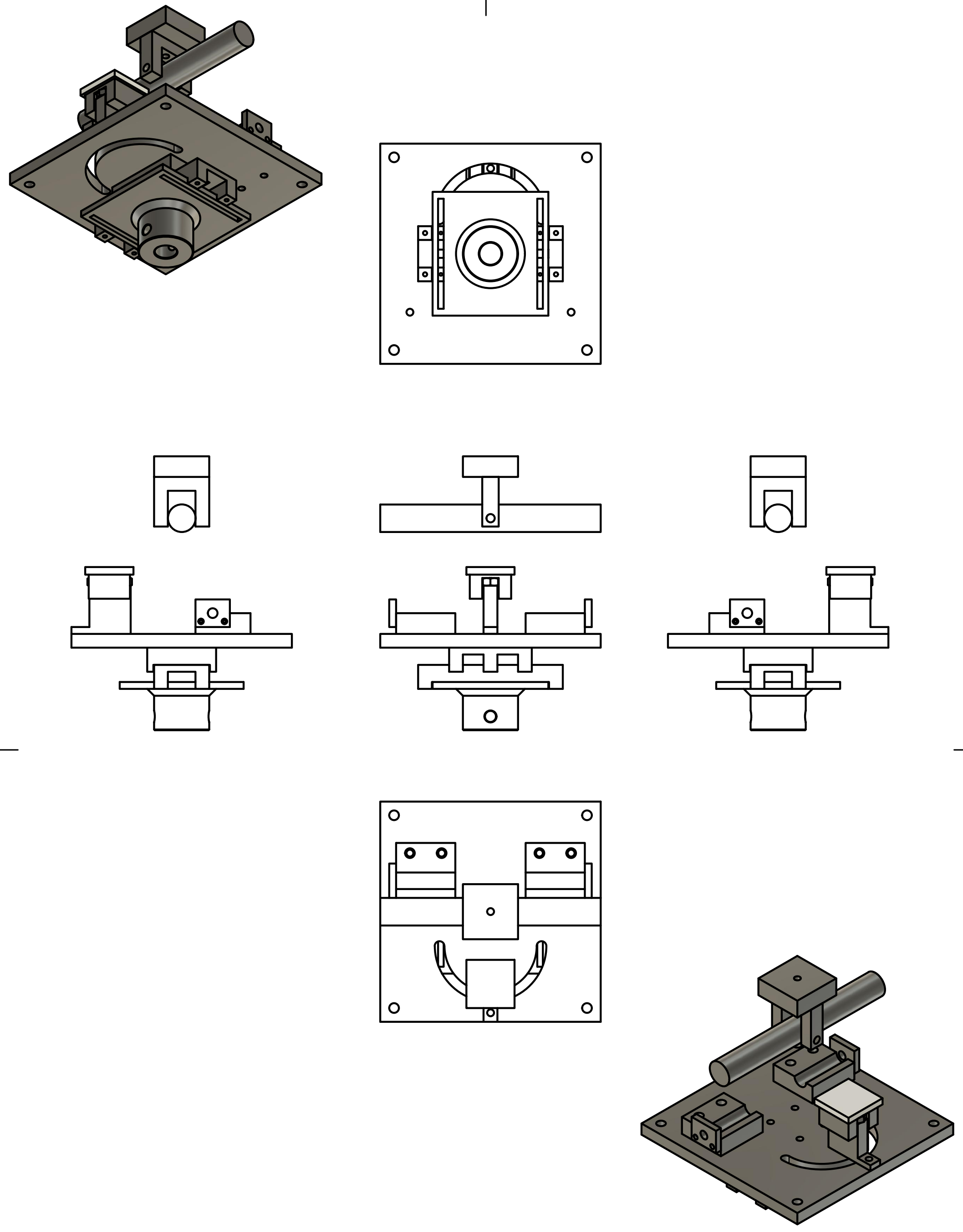

Dept.

Technical reference

Created by
Arthur van Kootwijk .

Approved by

Document type

Document status

Title
Experimental setup
Full overview

DWG No.

Rev.

Date of issue

Sheet
1/1

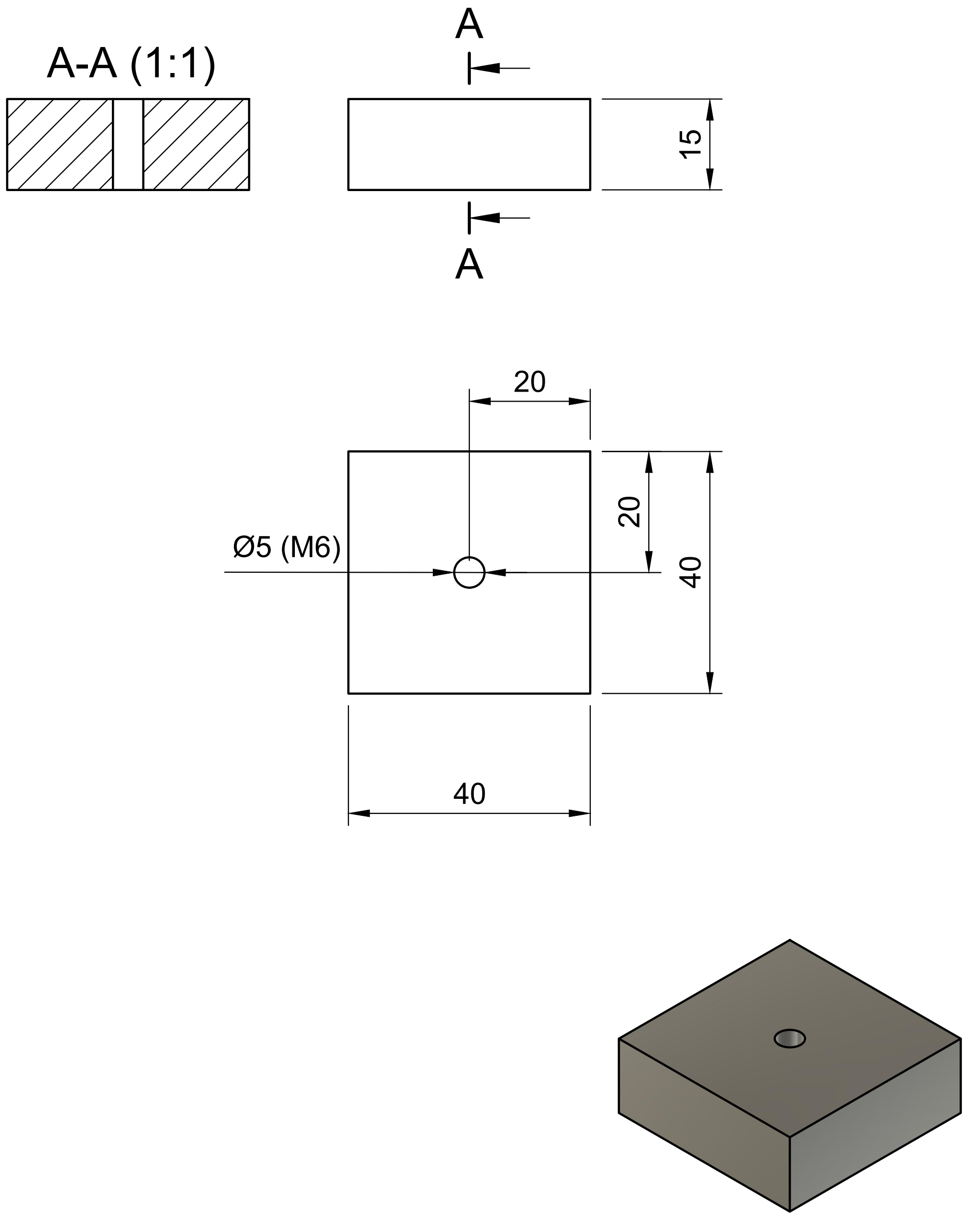

Dept.	Technical reference	Created by Arthur van Kootwijk	Approved by
		Document type	Document status
		Title Top block	DWG No.
			Rev. Date of issue Sheet 1/1

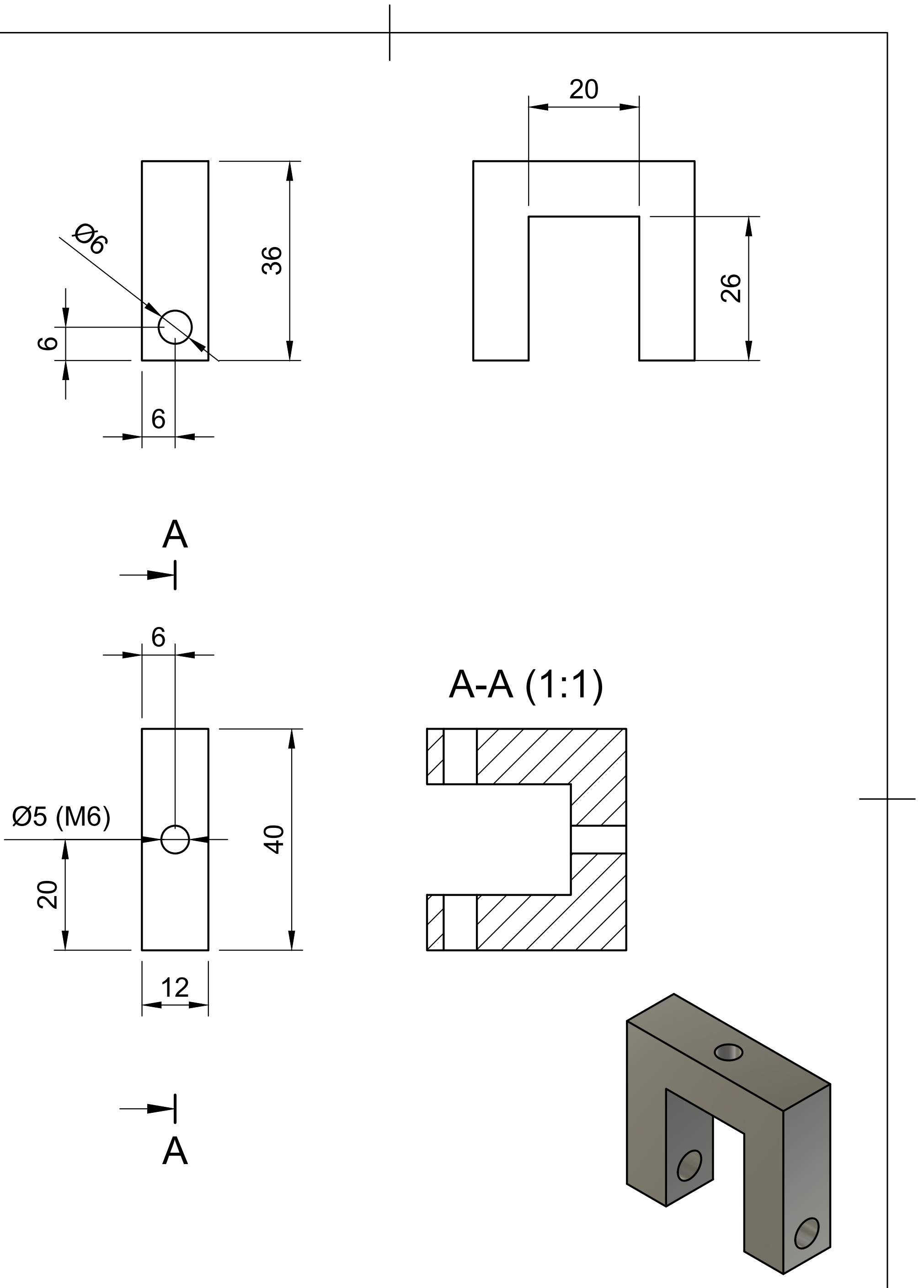

Dept.	Technical reference	Created by Arthur van Kootwijk	Approved by
		Document type	Document status
		Title Bar hold	DWG No.
			Rev. / Date of issue / Sheet 1/1

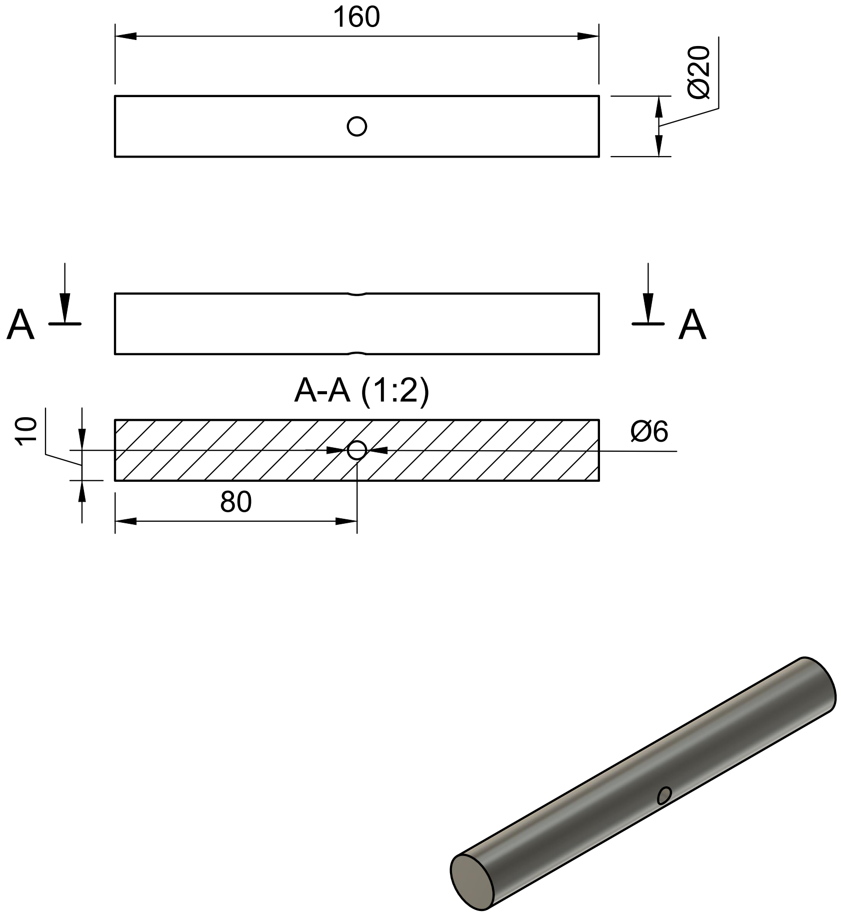

Dept.	Technical reference	Created by Arthur van Kootwijk	Approved by	
		Document type	Document status	
		Title Loading bar	DWG No.	
			Rev.	Date of issue	Sheet 1/1

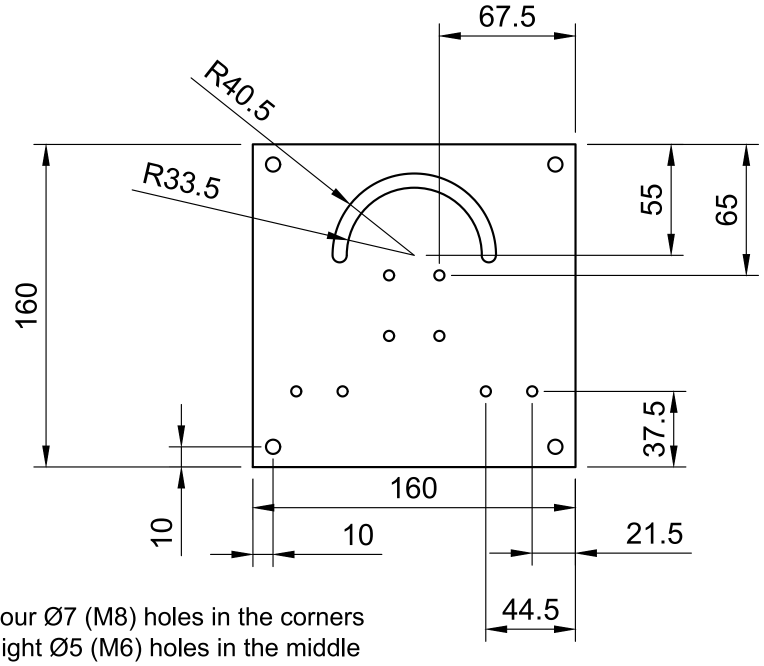

- Four Ø7 (M8) holes in the corners
- Eight Ø5 (M6) holes in the middle
- Symmetric distances from the centerpoint

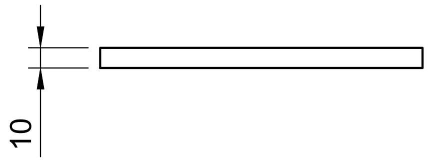

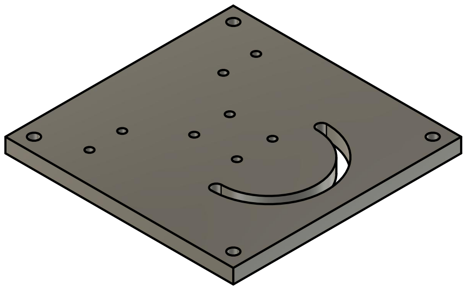

Dept.	Technical reference	Created by Arthur van Kootwijk .	Approved by
		Document type	Document status
		Title Bottom table	DWG No.
			Rev. Date of issue Sheet 1/1

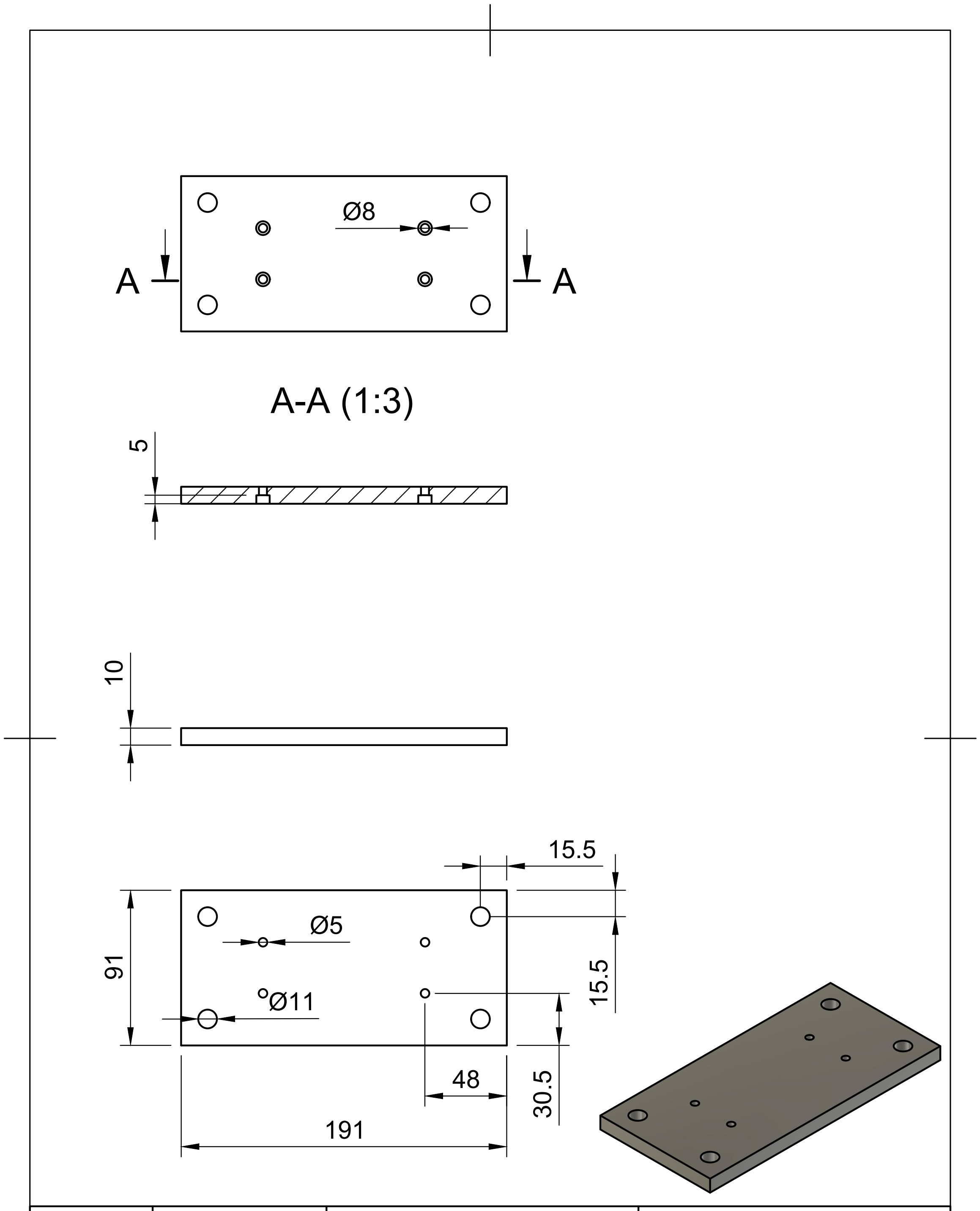

Dept.

Technical reference

Created by
Arthur van Kootwijk

Approved by

Document type

Document status

Title
Bottom plate INSTRON

DWG No.

Rev.

Date of issue

Sheet
1/1

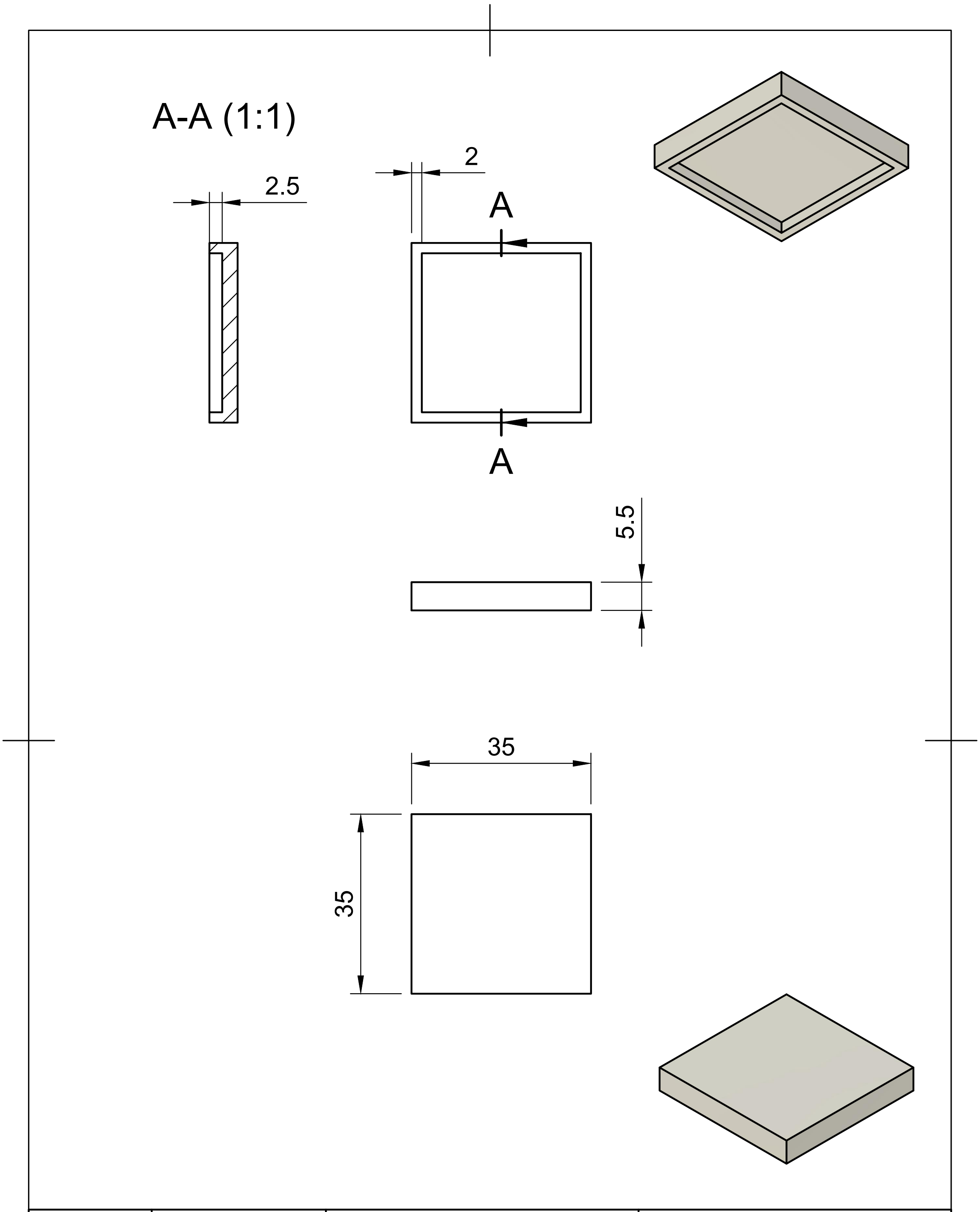

Dept.	Technical reference	Created by Arthur van Kootwijk .	Approved by
		Document type	Document status
		Title Tooth support top plate (PLA)	DWG No.
			Rev. Date of issue Sheet 1/1

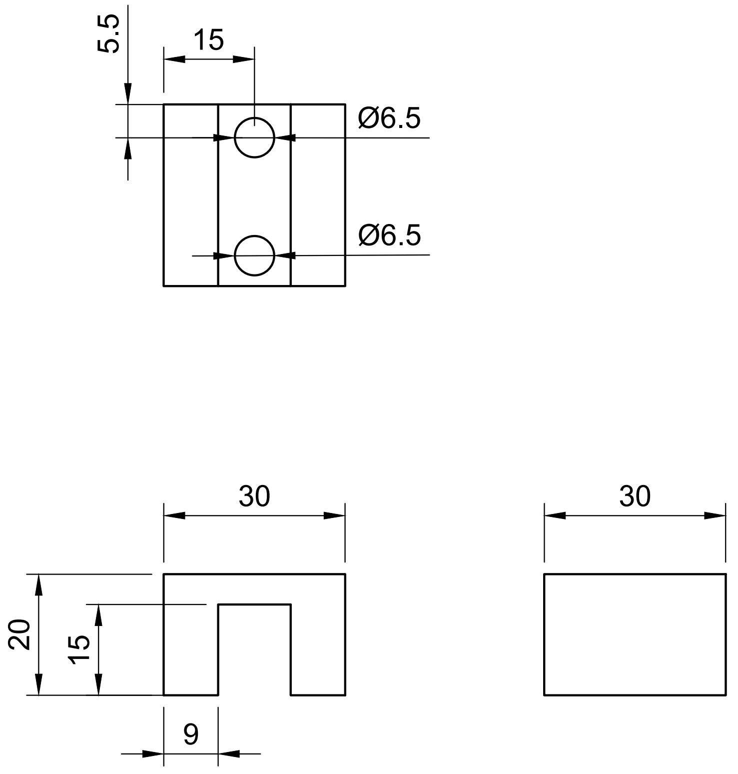

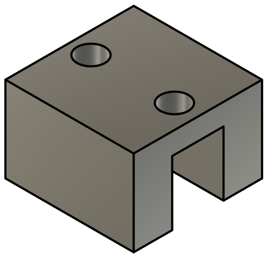

Dept.	Technical reference	Created by Arthur van Kootwijk .	Approved by
		Document type	Document status
		Title Tooth support middle part	DWG No.
			Rev. Date of issue Sheet 1/1

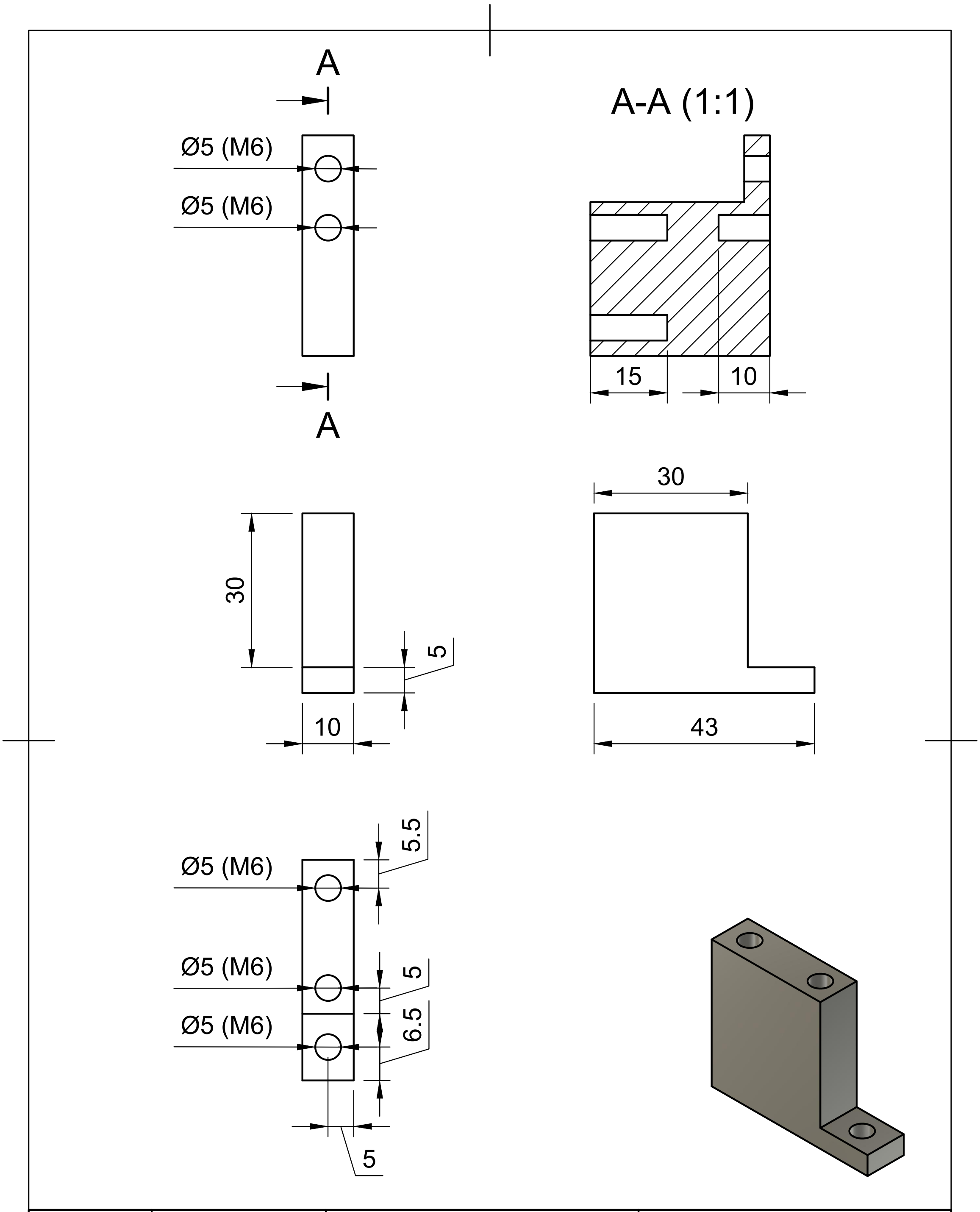

Dept.	Technical reference	Created by Arthur van Kootwijk	Approved by	
		Document type	Document status	
		Title Tooth support	DWG No.	
			Rev.	Date of issue	Sheet 1/1

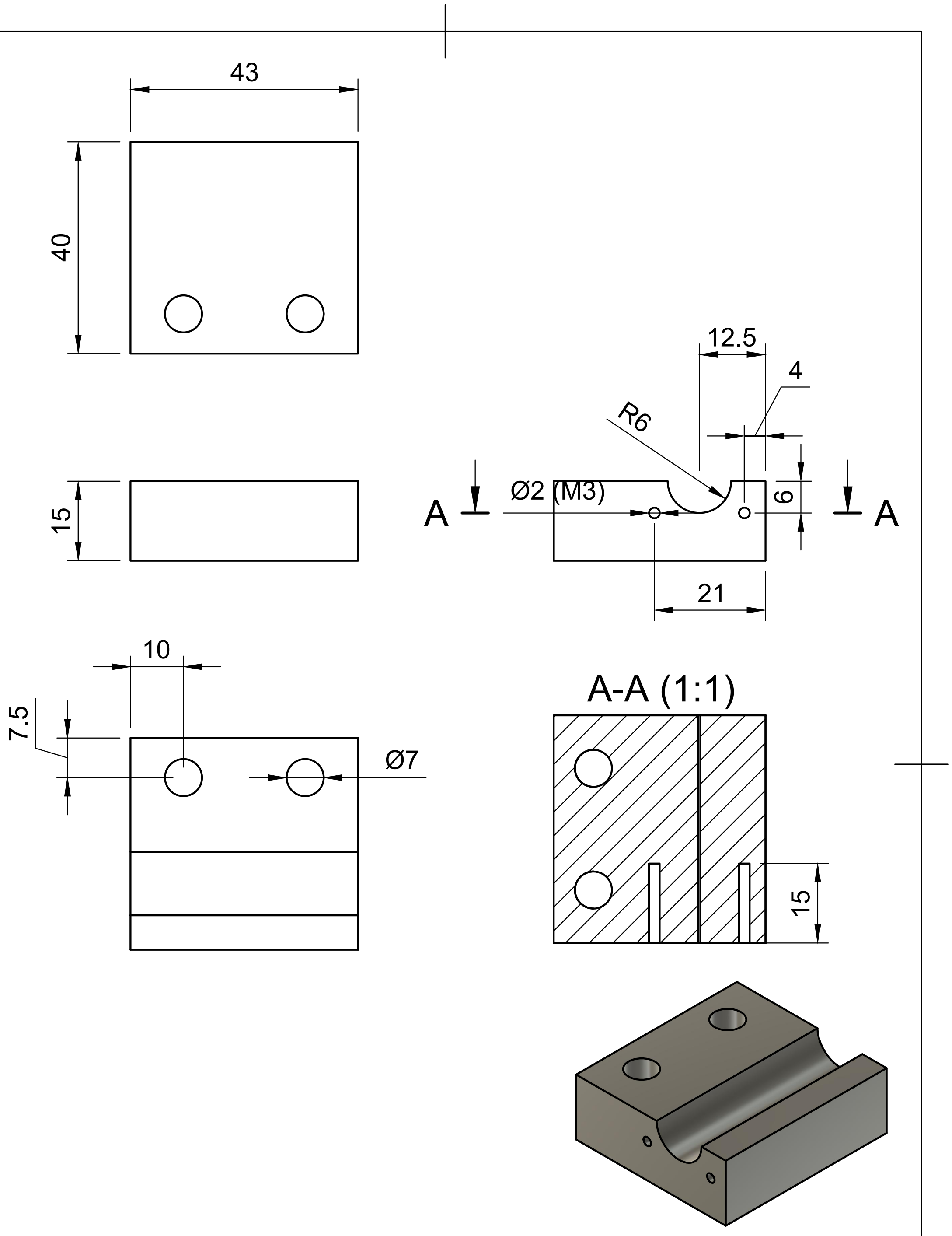

Dept.

Technical reference

Created by
Arthur van Kootwijk

Approved by

Document type

Document status

Title
Condyle support left

DWG No.

Rev.

Date of issue

Sheet
1/1

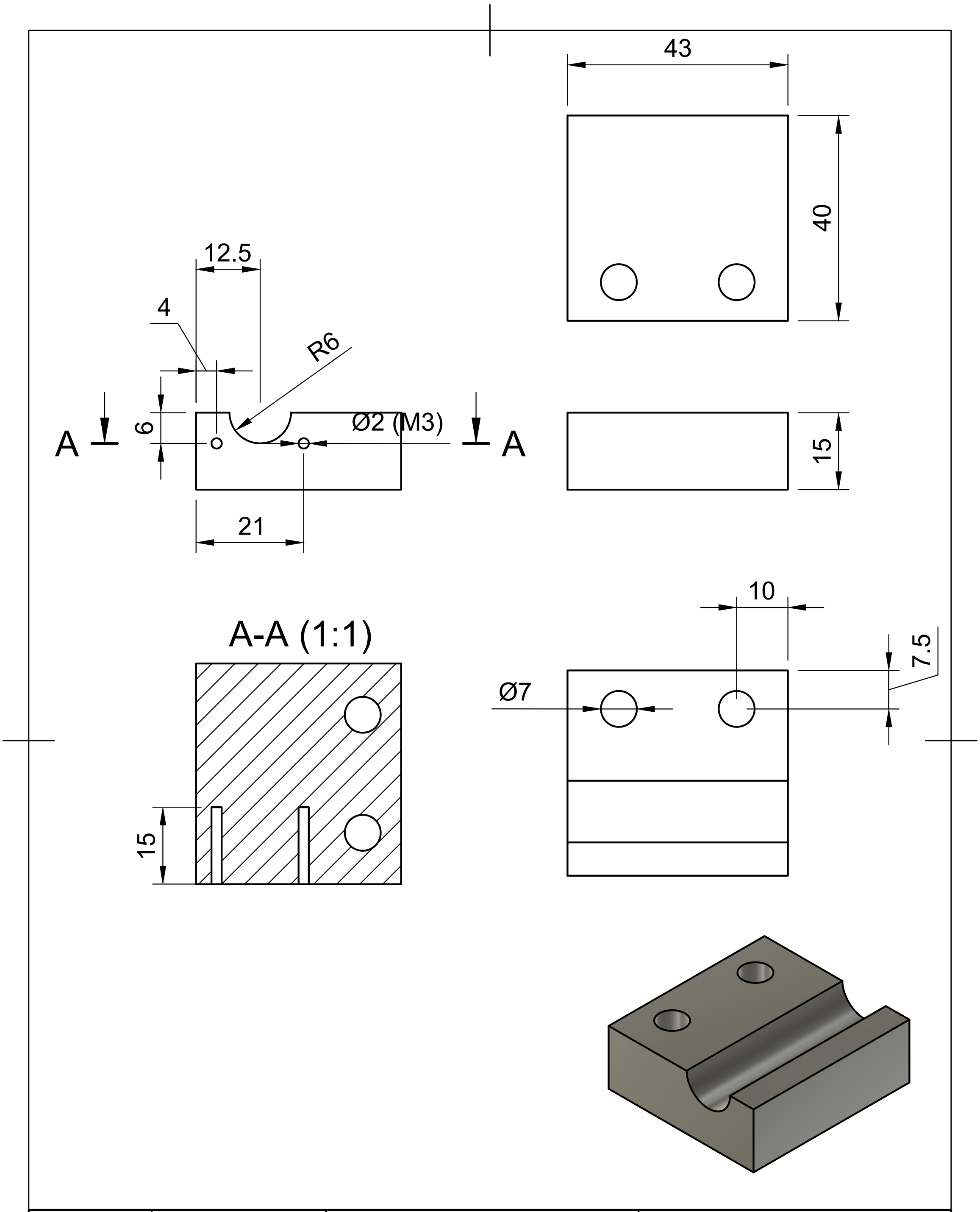

Dept.	Technical reference	Created by Arthur van Kootwijk	Approved by
		Document type	Document status
		Title Condyle support right	DWG No.
			Rev. | Date of issue | Sheet 1/1

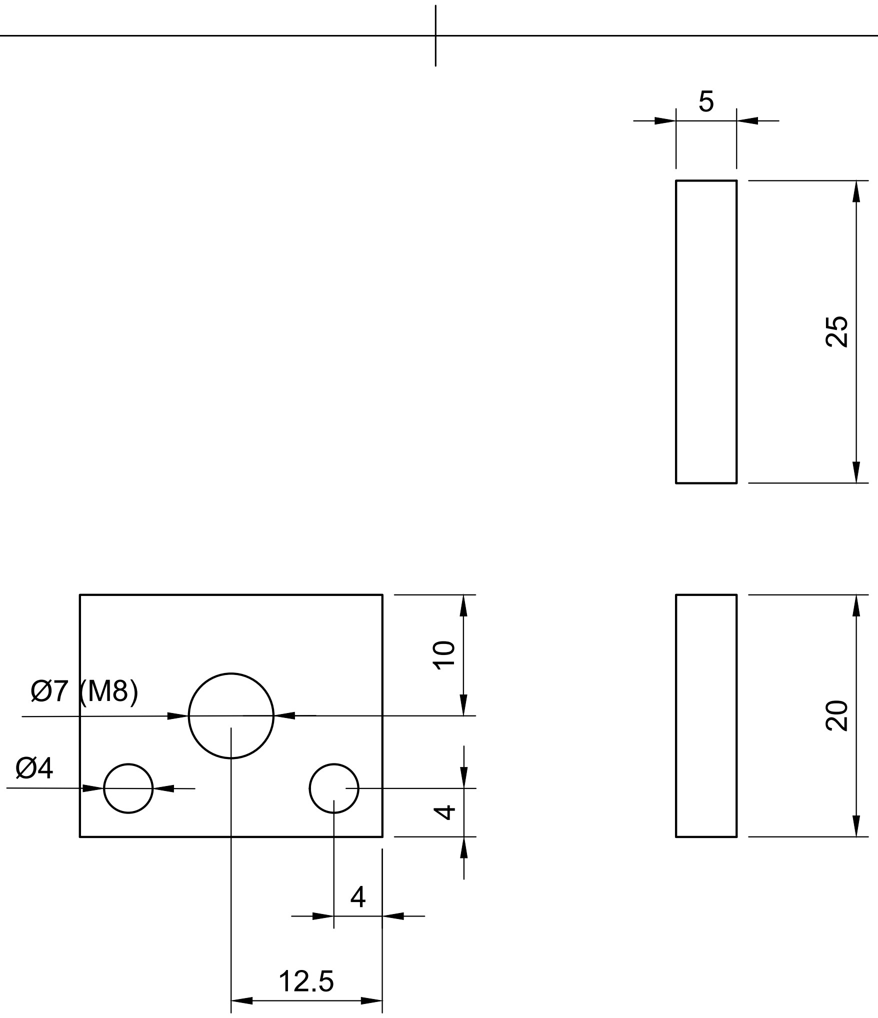

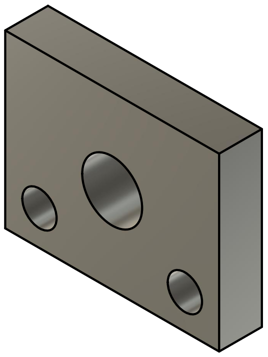

Dept.	Technical reference	Created by Arthur van Kootwijk	Approved by
		Document type	Document status
		Title Condyle side fixations (x2)	DWG No.
			Rev. Date of issue Sheet 1/1

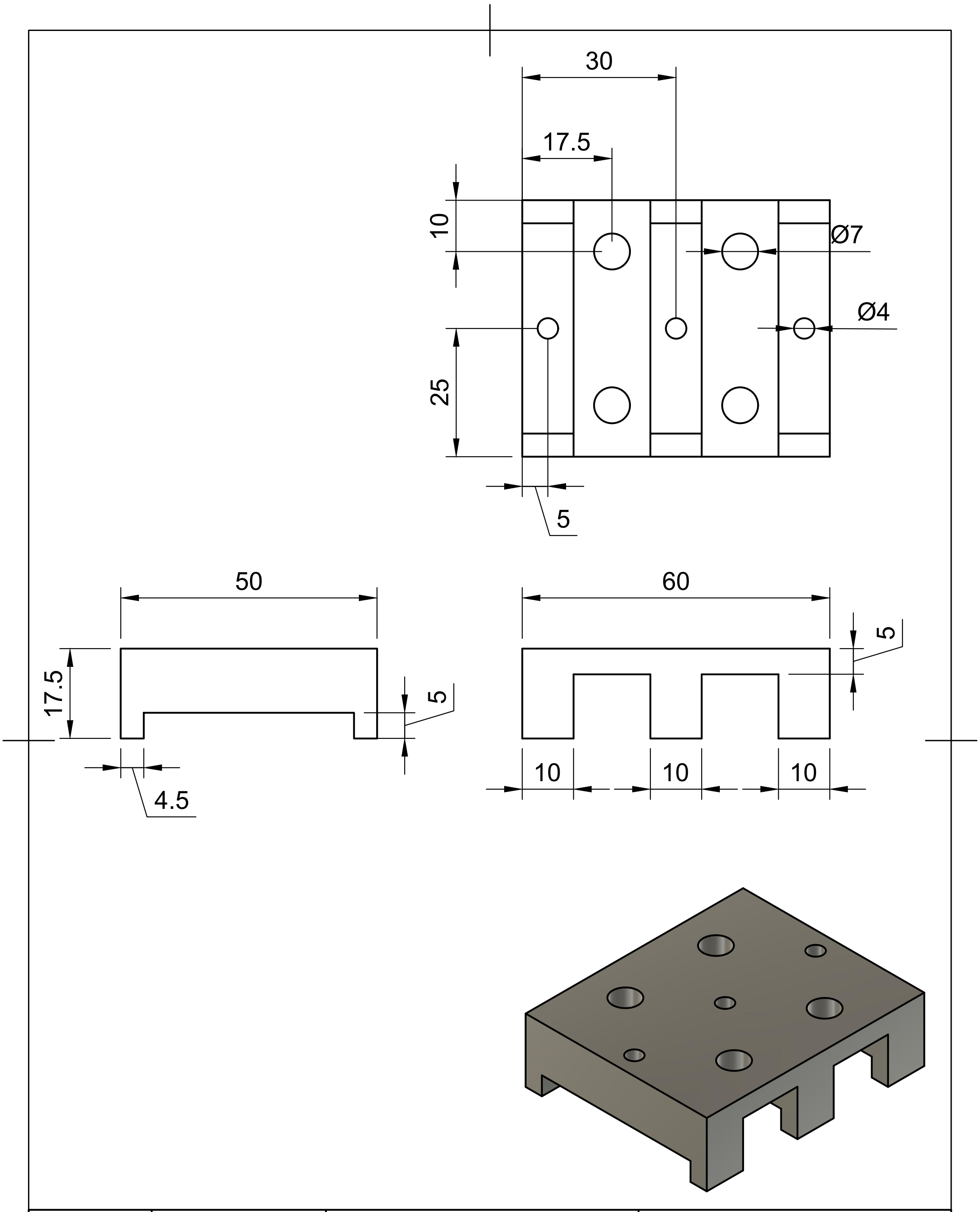

Dept.	Technical reference	Created by Arthur van Kootwijk	Approved by		
		Document type	Document status		
		Title XY-table top slide	DWG No.		
			Rev.	Date of issue	Sheet 1/1

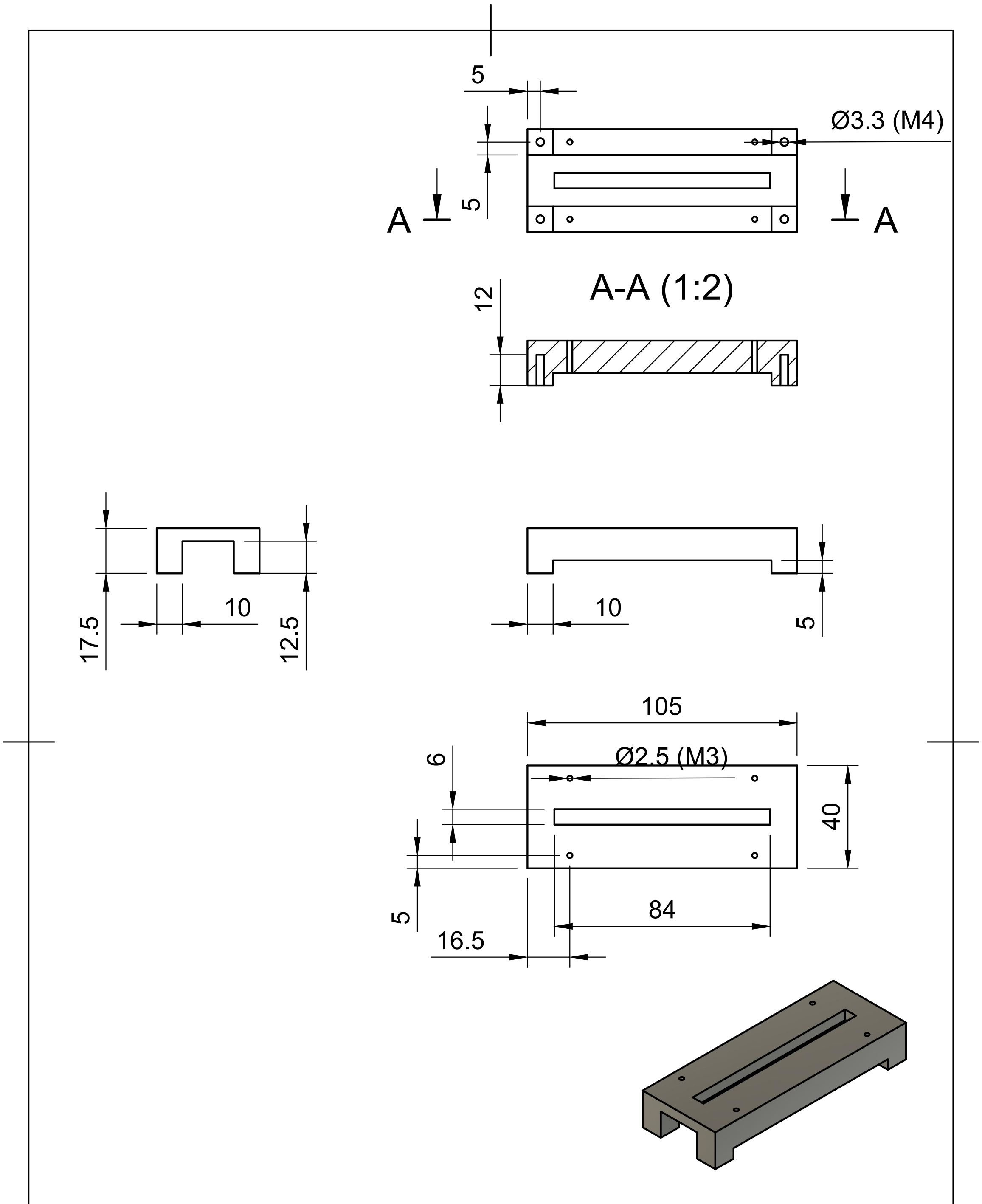

Dept.	Technical reference	Created by Arthur van Kootwijk	Approved by
		Document type	Document status
		Title XY-table bottom slide	DWG No.
			Rev. | Date of issue | Sheet 1/1

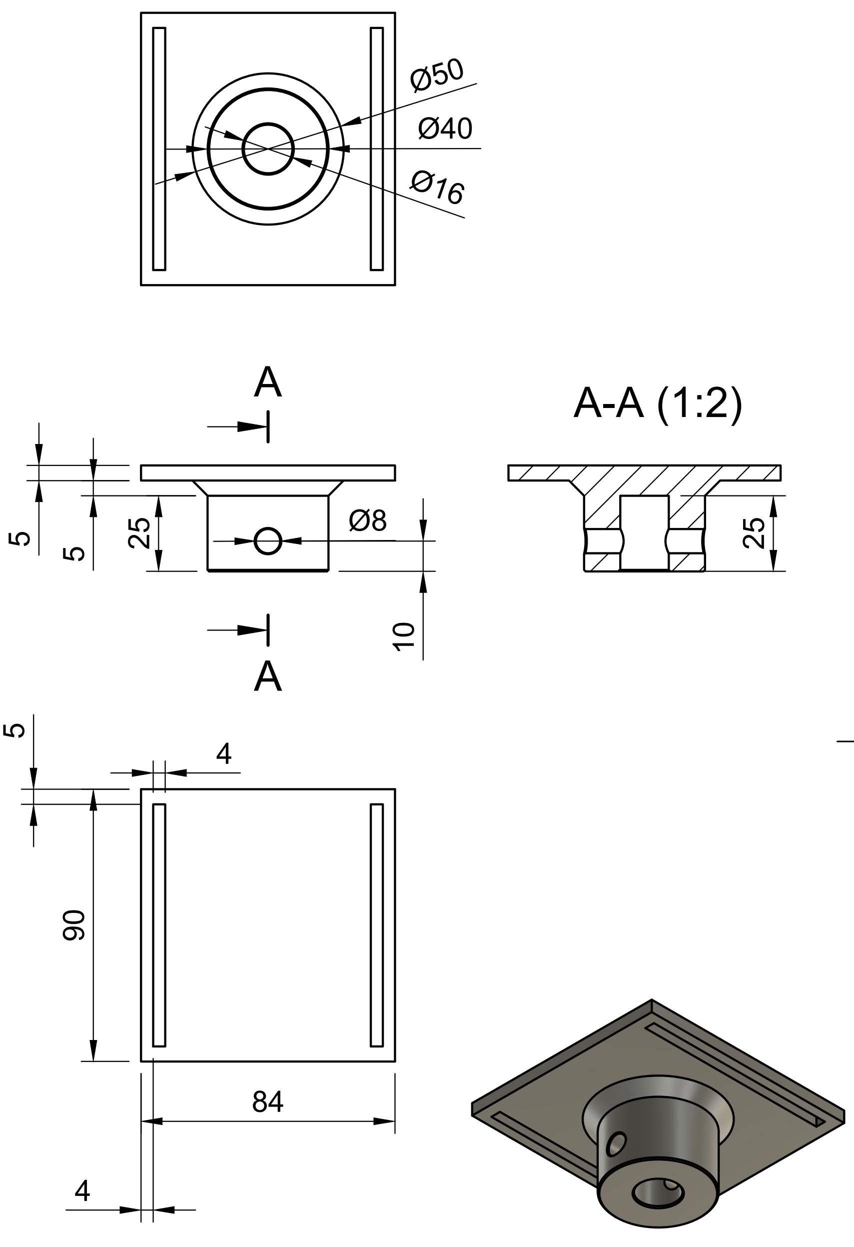

Dept.	Technical reference	Created by Arthur van Kootwijk	Approved by		
		Document type	Document status		
		Title Bottom block	DWG No.		
			Rev.	Date of issue	Sheet 1/1